RADIATIVE CAPTURE OF NEUTRONS AND DEUTERONS INTO ^{13}C: EVIDENCE FOR A SECONDARY DOORWAY STATE EFFECT.

by

Robert Andrew August, Jr.

Department of Physics
Duke University

Date: October 5, 1984

Approved:

Henry R. Weller

Henry R. Weller, Supervisor

Edward G. Bilpuch

Robert P. Behringer

Moon Hee

Michael Stearns

A dissertation submitted in partial fulfillment of the requirements for the degree of Doctor of Philosophy in the Department of Physics in the Graduate School of Duke University

1984

Abstract

RADIATIVE CAPTURE OF NEUTRONS AND DEUTERONS INTO ^{13}C: EVIDENCE FOR A SECONDARY DOORWAY STATE EFFECT.

by

Robert Andrew August, Jr.

Department of Physics
Duke University

Date: October 5, 1984

Approved:

Henry R. Weller, Supervisor

Edward G. Bilpuch

Robert P. Behringer

Monty Hall

Michael Shara

An abstract of a dissertation submitted in partial fulfillment of the requirements for the degree of Doctor of Philosophy in the Department of Physics in the Graduate School of Duke University

1984

RADIATIVE CAPTURE OF NEUTRONS AND DEUTERONS INTO ^{13}C:

EVIDENCE FOR A SECONDARY DOORWAY STATE EFFECT.

by

Robert Andrew August, Jr.

Differential cross sections were measured at a detector angle of 90^{o} in the lab for the $^{12}C(n,\gamma_0)^{13}C$ reaction at 19 incident neutron energies between 6.5 and 18.5 MeV. This energy region spans the pygmy and $T_<$ giant dipole resonances in ^{13}C. Angular distributions of cross section were measured for this reaction at 7 incident neutron energies between 12.0 and 18.5 MeV. Angular distributions of vector analyzing power were measured for the $^{12}C(\vec{n},\gamma_0)^{13}C$ reaction at 4 incident neutron energies between 12.0 and 18.2 MeV, analyzing powers were measured at 125^{o} for neutron energies of 15.4, 17.4, and 18.8 MeV.

The angular distributions show a rapid energy dependence just below the peak of the giant dipole resonance. This energy dependent structure in the angular distributions occurs at the same excitation energy as a resonance in the $^{11}B(d,\gamma_0)^{13}C$ reaction. A study of the deuteron capture reaction in this energy region was therefore undertaken. The 90^{o} differential cross sections were measured for the $^{11}B(d,\gamma_0)^{13}C$ reaction at 11 deuteron beam energies between 1.65 and 3.50 MeV. Angular distributions of cross section were measured at deuteron beam energies of 1.6, 1.8, 2.0, and 4.0 MeV. Angular distributions of vector and tensor ($T_{20}(\theta)$) analyzing power were measured at deuteron beam energies of 2.0 and 4.0 MeV, with 55^{o} and 125^{o} vector analyzing

powers being measured at 1.6 and 1.8 MeV.

Both data sets were fit simultaneously using a formalism which described the $^{11}B(d,\gamma_0)^{13}C$ resonance as a secondary doorway state, with the $T_<$ giant dipole resonance (seen through the neutron capture data) being a primary doorway state. The data were well described by this fit, most notably the rapid energy dependence in the neutron capture angular distributions. A shell model calculation of the expected strength of this interaction agreed well with the strength found by fitting the data. It was found to be possible to describe the deuteron capture angular distributions (the doorway state formalism leaves these independent of the rest of the analysis) fairly well using a simple "deuteron cluster" model of the ^{13}C ground state.

ACKNOWLEDGEMENTS

I would like to thank my thesis advisor, Dr. Henry R. Weller, for so many things that I will not even attempt to list them here. The work on this project by Drs. P. C. Colby, J. W. Jury, N. R. Roberson, D. R. Tilley, and especially J. G. Woodworth was most appreciated. I gratefully acknowledge the help received by the other students in the capture group, Doug Fields, Colleen Fitzpatrick, Steve King, James Langenbrunner, George Mitev, John Riley, Doug Wagenaar, Mark Whitton, and Mike Wright.

I would like to thank TUNL for the financial support of this work and of my graduate student career. The technical assistance of Mike Bailey, Paul Carter, Sidney Edwards, and Bob Rummel is gladly noted.

A special heartfelt thanks is extended for the long standing love and support of my parents and family (including Brian Allen).

Most of all, I thank my wife, Alison, for being the presence that makes everything worthwhile.

TABLE OF CONTENTS

List of Figures

List of Tables

1 INTRODUCTION

The photoabsorption strength in ^{13}C is concentrated in three main peaks located at excitation energies in ^{13}C of about 13, 21, and 25 MeV (Measday, 1965). The measure of this strength is the portion of the classical dipole sum rule exhausted by these peaks (Hayward, 1970). In ^{13}C the sum rule strength can be seen in the data of B.C. Cook (Cook, 1957) from which he extracts total photoabsorption cross sections. The region from 5 to 17 MeV excitation energy in ^{13}C contains the lowest energy resonance, the so called "pygmy" resonance, and exhausts no more than about 11 percent of the dipole sum rule. The region from 17 to 30 MeV excitation energy contains the upper two peaks, identified as the giant dipole resonance, and exhausts between 64 and 72 percent of the dipole sum rule. This should be considered in light of the fact that in the range from 0 to 30 MeV excitation energy in light nuclei ($Z < 20$) a survey of the amount of the dipole sum rule exhausted by these nuclei shows that it is never more than 80 percent (Measday, 1965; Hayward, 1970).

The fact that the giant dipole shows two distinct peaks is considered one of the best examples of isospin splitting of the giant dipole resonance (Hayward, 1970). The lower peak is $T = 1/2$ and the upper is $T = 3/2$. The pygmy resonance is also assigned $T = 1/2$ (Measday, 1965). One would then expect that reactions like $^{13}C(\gamma,n_0)^{12}C$ and $^{13}C(\gamma,d_0)^{11}B$ would not populate the $T_>$ resonance since the ^{12}C ground state is $T = 0$, the ^{11}B ground state is $T = 1/2$, and the neutron and deuteron have $T = 1/2$ and $T = 0$ respectively. (There can be some

deviation from this due to isospin mixing of the resonance caused by the isospin violating coulomb force.) This was indeed found to be the case in an earlier study of the $^{13}C(\gamma,n_0)^{12}C$ reaction (Woodworth, 1979), which found the pygmy and $T_<$ resonances, but not the $T_>$, to be populated by this reaction.

The current work has concentrated on the $T_<$ giant dipole region in ^{13}C using the time reversed radiative capture reactions $^{12}C(n,\gamma_0)^{13}C$ and $^{11}B(d,\gamma_0)^{13}C$. Differential cross section measurements at 90^o were made over the region of the pygmy and $T_<$ giant dipole resonances, corresponding to excitation energies in ^{13}C of 10.5 to 22.0 MeV, for the $^{12}C(n,\gamma_0)^{13}C$ reaction. These measurements show the pygmy and $T_<$ giant dipole peaks. More extensive studies of this reaction were made in the region of the giant dipole from 16.0 to 22.0 MeV excitation energy in ^{13}C using unpolarized and polarized angular distribution measurements. A strong energy dependence over a region of the order of a few MeV, just below the peak of the giant dipole resonance, was noticed in both the a_2 and b_2 Legendre polynomial coefficients derived from these angular distribution measurements. Typically the energy dependence of the angular distributions of nucleon capture gamma rays varies slowly over the region of the giant dipole resonance. These cases have been successfully described by a simple model known as the Direct Semidirect (DSD) Model, which cannot describe the strong energy dependence observed in our data.

A resonance in the region of ^{13}C corresponding to the energies at which the strong energy dependence is observed in the $^{12}C(n,\gamma_0)^{13}C$

reaction was previously observed in the $^{11}B(d,\gamma_0)^{13}C$ reaction (Weller, 1973). This suggests that a secondary doorway exists in the ^{13}C system. Such secondary doorway structures have been seen previously in the case of the ^{16}O nucleus (Calarco, 1977). In that case structure in the $^{15}N(p,\gamma_0)^{16}O$ reaction was correlated with a resonance in the $^{12}C(\alpha,\gamma_0)^{16}O$ cross section. The interaction was between states of different isospin and presumably proceeded via the isospin violating coulomb interaction. In our case the interference is between states of the same isospin and should therefore proceed via the strong force. The $^{11}B(d,\gamma_0)^{13}C$ resonance was studied in this work using 90^{o} differential cross section measurements in the range of excitation energy in ^{13}C from 20.0 to 22.0 MeV. Also, unpolarized, vector polarized, and tensor polarized angular distribution measurements were taken in this same range of excitation.

This study attempts to explain this intermediate structure in the giant dipole resonance of ^{13}C using a secondary doorway state formalism as derived from works by Feshbach, Kerman, and Lemmer (Feshbach, 1967) and Wang and Shakin (Wang, 1972). Our data are consistent with an electric dipole dominated description of this region, as will be shown in the chapter on angular distributions, and therefore a pure electric dipole analysis is used. A comparison is also made between the strength of the interaction between these doorway states as derived from fitting the data to a secondary doorway state formalism, and a calculation of the strength of the interaction using shell model configurations in which the interaction is the result of the strong force coupling the nucleons.

2 THEORY

2.1 Classification of Giant Multipole Resonances

Giant multipole resonances are classified according to the basic oscillations of the nucleus to which they correspond. Some examples are shown in Figure 2-1. The monopole modes are spherically symmetric vibrations, the dipole modes vibrate along a single axis, the quadrupole modes vibrate along two different axes, and so on for the higher multipoles. In the electric modes there is no differentiation according to spin, while in the magnetic modes particles with spin up vibrate against particles with spin down. In isoscalar modes there is no differentiation between protons and neutrons, while in the isovector modes protons vibrate against neutrons. The multipolarity of the vibration goes as 2^L, where, in radiative capture reactions, L is the angular momentum carried off by the photon emitted in the transition from the intermediate excited state to the final state of the transition. The notation used is EL or ML, such that E1 corresponds to electric dipole, M2 corresponds to magnetic quadrupole, and so on. The parity change of the nucleus during an electric transition is $(-1)^L$, while during a magnetic transition it is $(-1)^{L+1}$. In isoscalar modes the transition is between states of the same isospin, while in isovector modes $T \rightarrow T-1, T, T+1$ with $T=0 \rightarrow T=0$ excluded.

Figure 2-1.

Some examples of basic oscillations of the nucleus that correspond to the giant multipole resonances.

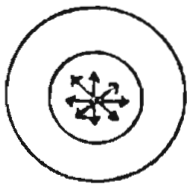

ISOSCALAR

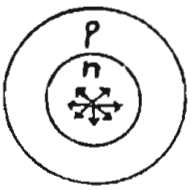

ISOVECTOR

Electric Monopole

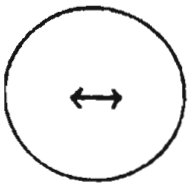

ISOSCALAR

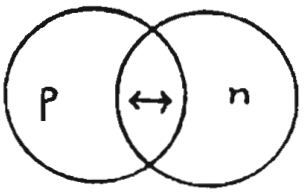

ISOVECTOR

Electric Dipole

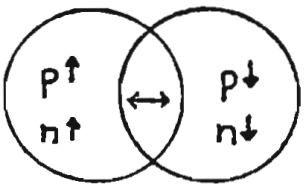

ISOSCALAR

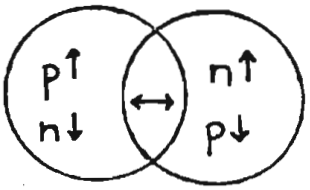

ISOVECTOR

Magnetic Dipole

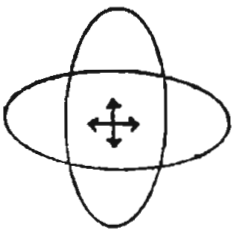

ISOSCALAR

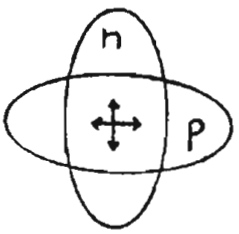

ISOVECTOR

Electric Quadrupole

2.2 The Giant Dipole Resonance

The giant dipole resonance has been identified as an isovector electric dipole vibration of the nucleus. It was first identified as such by Goldhaber and Teller in 1948 (Goldhaber, 1948). It is the main component of the giant resonance region of nuclei, a region which dominates the photoabsorption cross section in nuclei, and it can be considered a general property of nuclear matter. The peak of the giant dipole resonance is located near $80\,A^{-1/3}$ MeV in medium and heavy nuclei and at about 20 MeV in light nuclei. It is usually 3 to 10 MeV in width (Hayward, 1970). As mentioned in the introduction, the measure of the strength of a multipole transition is the amount of the appropriate sum rule it exhausts. The classical dipole sum rule is:

$$2\text{-}1 \qquad \int \sigma_{\gamma}(E1)\,dE_{\gamma} = 60\frac{NZ}{A}\ \text{mb}\cdot\text{MeV}.$$

For ^{13}C the classical dipole sum has the value 193.85 mb·MeV.

As mentioned in the introduction, a simple model known as the Direct Semidirect (DSD) Model has been used successfully to describe the radiative capture process (Brown, 1964; Clement, 1965). This model separates the capture process into two parts: a direct and a semidirect part. The direct part corresponds to the incoming nucleon being captured directly to the final state and emitting a gamma ray as it does so. The semidirect part corresponds to the incoming nucleon exciting the nucleus into a collective state which then decays to the final state

by emission of a gamma ray. Both of these processes predict angular distributions which vary slowly with energy over the region of the giant dipole resonance. The DSD model can be used successfully to predict the shape of the angular distribution of the reaction in the case of the $^{11}B(d,\gamma_0)^{13}C$ reaction. Calculations of the absolute cross section which arises from the direct term alone, however, predict a cross section vastly smaller than the experimental results, indicating that the reaction is a resonant one in this energy region. On the other hand, the DSD model can not predict the strong energy dependence of the angular distribution of the $^{12}C(n,\gamma_0)^{13}C$ reaction in this energy region. A secondary doorway state was introduced into the problem in order to describe both the $^{11}B(d,\gamma_0)^{13}C$ and $^{12}C(n,\gamma_0)^{13}C$ results successfully.

In the secondary doorway state approach, the giant dipole resonance in ^{13}C is taken to be the primary state, observed as the dominant feature in the $^{12}C(n,\gamma_0)^{13}C$ data, which could then interfere with a more complicated secondary state, observed as the dominant feature in the $^{11}B(d,\gamma_0)^{13}C$ data. The more complicated state was taken to have no intrinsic gamma decay width and could therefore decay only by coupling to the primary state which subsequently decayed. This lack of a second decay channel to interfere with this decay channel explains why the angular distribution data for the $^{11}B(d,\gamma_0)^{13}C$ reaction displays the slow energy dependence characteristic of the DSD model rather than the rapid energy dependence shown in the $^{12}C(n,\gamma_0)^{13}C$ data. The results of this secondary doorway analysis will be discussed later in this thesis.

2.3 Doorway States

The idea of "doorway states" was developed in order to explain resonances in nuclei with widths intermediate between those of the compound nuclear states and the larger widths of the optical model shape resonances. These states are relatively simple modes of excitation whose complexity falls between the single particle virtual states used to explain the optical model shape resonances and the complicated compound nuclear states.

The supposition is made that these states are the only states which strongly couple directly to the entrance channel. To realize the full complexity of a compound nuclear state, a system must first pass through these doorway states from the entrance channel. The hypothesis that such simple states exist and that they are the only states which couple strongly to the entrance channel is referred to as the "doorway state hypothesis" (Feshbach, 1967).

The doorway state is not an eigenvalue of the nuclear Hamiltonian; therefore, if a nuclear system were placed in a doorway state, its probability of remaining there would decrease with increasing time. The decay rate of the doorway state consists of a term for decay into the entrance channel and a term for decay into the more complicated compound nuclear states. The width Γ_d of the doorway state will thus consist of two parts: a width $\Gamma_d^{\uparrow}$ for decay into the entrance channel and a width $\Gamma_d^{\downarrow}$ for decay into the compound nucleus. The lifetime of the doorway state

is given by $\hbar/(\Gamma_d^{\uparrow} + \Gamma_d^{\downarrow})$. To give rise to an intermediate resonance this lifetime must lie between compound nuclear lifetimes and characteristic single particle lifetimes.

It is important to realize that the doorway state hypothesis does not depend on any model used to describe the nuclear states involved. The hypothesis itself is model-independent and should be considered a framework on which one can apply a model. The applied model would depend only on the characteristics of the particular case being studied.

2.4 Doorway State Formalism

To derive the formalism we follow Seyler (Seyler, 1983), Wang and Shakin (Wang, 1972). Let $|\Psi\rangle$ be the wave function of the nuclear system with the particle to be captured in a continuum state and H be the nuclear Hamiltonian. Then the Schrödinger equation is:

2-2 $$(E-H)|\Psi\rangle = 0.$$

We now define the projection operators P, d, Q such that

2-3 $$|\Psi\rangle = P|\Psi\rangle + d|\Psi\rangle + Q|\Psi\rangle,$$

where P projects onto the subspace containing the open entrance channels for the particle in the continuum, d projects onto the subspace of simple excited states coupled strongly to the entrance channels, and Q projects onto all possible configurations not included in P and d. These operators obey the following conditions:

2-4 Completeness $P + d + Q = 1$

Orthogonality $Pd = dP = 0$; $PQ = QP = 0$; $Qd = dQ = 0$.

In the following discussion the notation $H_{XX} = XHX$ and $|X\psi\rangle = X|\psi\rangle$ will be used.

The orthogonality conditions (2-4) and equations (2-2) and (2-3) lead directly to the coupled equations:

2-5
$$(E-H_{PP})|P\psi\rangle = H_{Pd}|d\psi\rangle + H_{PQ}|Q\psi\rangle$$
$$(E-H_{dd})|d\psi\rangle = H_{dP}|P\psi\rangle + H_{dQ}|Q\psi\rangle$$
$$(E-H_{QQ})|Q\psi\rangle = H_{QP}|P\psi\rangle + H_{Qd}|d\psi\rangle.$$

Solving for $|Q\psi\rangle$,

2-6
$$|Q\psi\rangle = (E-H_{QQ})^{-1}H_{QP}|P\psi\rangle + (E-H_{QQ})^{-1}H_{Qd}|d\psi\rangle,$$

and substituting into (2-5) along with the renormalized Hamiltonian

2-7
$$\tilde{H} = H + HQ(E-H_{QQ})^{-1}QH$$
$$= H + H\frac{Q}{(E-H_{QQ})}H$$

yields the coupled equations:

2-8
$$(E-\tilde{H}_{PP})|P\psi\rangle = \tilde{H}_{Pd}|d\psi\rangle$$
$$(E-\tilde{H}_{dd})|d\psi\rangle = \tilde{H}_{dP}|P\psi\rangle.$$

Solving for $|d\psi\rangle$,

2-9
$$|d\psi\rangle = (E-\tilde{H}_{dd})^{-1}\tilde{H}_{dP}|P\psi\rangle,$$

and substituting into (2-8) yields:

$$2\text{-}10 \qquad (E-\tilde{H}_{PP})|P\psi\rangle = \tilde{H}_{Pd}(E-\tilde{H}_{dd})^{-1}\tilde{H}_{dP}|P\psi\rangle.$$

We now obtain the solution,

$$2\text{-}11 \qquad |P\psi^{\pm}\rangle = |\psi_0^{\pm}\rangle + (E-\tilde{H}_{PP}\pm i\varepsilon)^{-1}\tilde{H}_{Pd}(E-\tilde{H}_{dd})^{-1}\tilde{H}_{dP}|P\psi^{\pm}\rangle,$$

where the homogeneous solution $|\psi_0^{\pm}\rangle$ satisfies

$$2\text{-}12 \qquad (E-\tilde{H}_{PP})|\psi_0^{\pm}\rangle = 0,$$

and we choose the (+) solutions for capture and the (-) solutions for photodisintegration. We now use the Greens function

$$2\text{-}13 \qquad g_P^{+} = (E-\tilde{H}_{PP}+i\varepsilon)^{-1}$$

and equations (2-8) to find that

$$2\text{-}14 \qquad |P\psi^{+}\rangle = |\psi_0^{+}\rangle + g_P^{+}\tilde{H}_{Pd}(E-\tilde{H}_{dd}-\tilde{H}_{dP}\, g_P^{+}\tilde{H}_{Pd})^{-1}\tilde{H}_{dP}|\psi_0^{+}\rangle,$$

$$|d\psi^{+}\rangle = (E-\tilde{H}_{dd}-\tilde{H}_{dP}\, g_P^{+}\tilde{H}_{Pd})^{-1}\tilde{H}_{dP}|\psi_0^{+}\rangle.$$

It then follows that

$$2\text{-}15 \qquad |\psi^{+}\rangle = (1+(E-H_{QQ})^{-1}QH)\,(|P\psi^{+}\rangle+|d\psi^{+}\rangle),$$

which results in our solution:

$$2\text{-}16 \qquad |\psi^{+}\rangle = (1+(E-H_{QQ})^{-1}QH)\,[1+g_P^{+}\tilde{H}_{Pd}(E-\tilde{H}_{dd}-\tilde{H}_{dP}\, g_P^{+}\tilde{H}_{Pd})^{-1}\tilde{H}_{dP}$$
$$+(E-\tilde{H}_{dd}-\tilde{H}_{dP}\, g_P^{+}\tilde{H}_{Pd})^{-1}\tilde{H}_{dP}]\,|\psi_0^{+}\rangle.$$

We now write the T-matrix for radiative capture as

2-17 $$T = \langle 0|H_\gamma|\psi^+\rangle,$$

where $|0\rangle$ is the final state, H_γ is the electromagnetic operator, and $|\psi^+\rangle$ is the continuum state solution just found.

Defining the effective electromagnetic operator $\tilde{H}_\gamma$ as

2-18 $$\tilde{H}_\gamma = H_\gamma + H_\gamma \frac{Q}{E-H_{QQ}} H,$$

we now have

2-19 $$T = \langle 0|\tilde{H}_\gamma|\psi_0^+\rangle + \sum_d \sum_{d'} \langle 0|\tilde{H}_\gamma + \tilde{H}_\gamma g_P^+ \tilde{H}_{Pd}|\mu_d\rangle \times \langle \mu_d|D^{-1}|\mu_{d'}\rangle \langle \mu_{d'}|\tilde{H}_{dP}|\psi_0^+\rangle,$$

where

2-20 $$\langle \mu_d|D^{-1}|\mu_{d'}\rangle = \langle \mu_d|(E-\tilde{H}_{dd}-\tilde{H}_{dP}\, g_P^+ \tilde{H}_{Pd})^{-1}|\mu_{d'}\rangle = \langle \mu_d|(E-H_{dd}-H_{dQ}(E-H_{QQ})^{-1}H_{Qd}-\tilde{H}_{dP}\, g_P^+ \tilde{H}_{Pd})^{-1}|\mu_{d'}\rangle.$$

Here we have introduced a complete set of eigenstates in d space, $\{\mu_d\}$, which is defined by

2-21 $$(E_d-H_{dd})|\mu_d\rangle = 0.$$

We now introduce the notation:

2-22 $$W_{dd'} \equiv W_{dd'}^{\uparrow} + W_{dd'}^{\downarrow}$$

$$\equiv \langle \mu_d|H_{dQ}(E-H_{QQ})^{-1}H_{Qd}-\tilde{H}_{dP}\, g_P^+ \tilde{H}_{Pd}|\mu_{d'}\rangle$$

$$W_{dd'}^{\uparrow} \equiv \langle \mu_d|\tilde{H}_{dP}\, g_P^+ \tilde{H}_{Pd}|\mu_{d'}\rangle$$

$$\equiv \Delta^{\uparrow}_{dd'} - \frac{i}{2}\Gamma^{\uparrow}_{dd'}$$

$$W^{\downarrow}_{dd'} \equiv \langle \mu_d | H_{dQ}(E-H_{QQ})^{-1} H_{Qd} | \mu_{d'} \rangle$$

$$\equiv \Delta^{\downarrow}_{dd'} - \frac{i}{2}\Gamma^{\downarrow}_{dd'}$$

$$\Delta_{dd'} \equiv \Delta^{\uparrow}_{dd'} + \Delta^{\downarrow}_{dd'}$$

$$\Gamma_{dd'} \equiv \Gamma^{\uparrow}_{dd'} + \Gamma^{\downarrow}_{dd'} \ ,$$

where $W^{\uparrow}_{dd'}$ represents the continuum coupling and $W^{\downarrow}_{dd'}$ represents the compound coupling. These couplings represent the interaction between the doorway state in question and other doorway states in the continuum and in the compound nucleus respectively.

The doorway state hypothesis now says that

2-23 $$H_{PQ} = H_{QP} = 0$$

$$QH_{\gamma} = H_{\gamma}Q = 0,$$

or in other words that the compound states can be reached only through the doorway states. This then lets us replace $\tilde{H}_{\gamma}$ by H_{γ} in our expression for T. We will also assume no significant contribution from single particle resonances in P space:

2-24 $$\langle 0|H_{\gamma}|\mu_d\rangle \ \gg \langle 0|H_{\gamma} g^{+}_{P} \tilde{H}_{Pd}|\mu_d\rangle.$$

In the case of nonoverlapping doorways, the off-diagonal $W_{dd'}$ are small compared to the on-diagonal. The expression for the T-matrix then becomes

2-25 $$T = \langle 0|H_{\gamma}|\psi^{+}_{0}\rangle + \sum_{d} \frac{\langle 0|H_{\gamma}|\mu_d\rangle\langle\mu_d|H_{dP}|\psi^{+}_{0}\rangle}{E-E_d-\Delta_d+\frac{i}{2}\Gamma_d}.$$

The first term in this expression represents direct capture and the second is the form of the noninterfering resonances. The case of interest to us, however, is that in which two of the doorways overlap. In this case the form of the T-matrix will be the same as (2-25) plus the term for the interfering states. Therefore, from now on we will drop the part of T including the direct term and nonoverlapping resonances and include only the part generated from the two overlapping states.

It is convenient at this point to introduce the notation:

2-26
$$E_{dr} \equiv E_d - \Delta_d$$
$$g_d^{\gamma} \equiv \langle 0 | H_{\gamma} | \mu_d \rangle$$
$$g_d^{\alpha \ell j} \exp(i\theta_d^{\alpha \ell}) \equiv \langle \mu_d | H_{dP} | \psi_0^+ \rangle,$$

where the j dependence has been dropped from the phase. The indices α, ℓ, and j refer to the particle type (α = p, n, or d corresponds to p = proton, n = neutron, or d = deuteron), orbital angular momentum, and total angular momentum, respectively, of the incoming partial wave. The g's are the square roots of the escape widths of the channels indicated. Also we can rewrite D^{-1} for two overlapping doorways such that

2-27
$$\sum_d \sum_{d'} \langle \mu_d | D^{-1} | \mu_{d'} \rangle = \left\langle \begin{bmatrix} E-E_1-W_{11} & -W_{12} \\ -W_{21} & E-E_2-W_{22} \end{bmatrix}^{-1} \right\rangle$$
$$= \frac{1}{\tilde{D}} \left\langle \begin{bmatrix} E-E_2-W_{22} & W_{12} \\ W_{21} & E-E_1-W_{11} \end{bmatrix} \right\rangle$$

$$\tilde{D} = (E-E_1-W_{11})(E-E_2-W_{22}) - W_{12}W_{21}.$$

Assuming W to be Hermitian (Calarco, 1977), we can write $W = W^{\dagger}$

$\Rightarrow W_{21} = W_{12}^{*}$ and $W_{12}^{*}W_{21} = |W_{12}|^2 \equiv |V|^2$. Therefore:

$$2\text{-}28 \qquad T_{\ell j}^{\alpha} = \frac{g_1^{\gamma} g_1^{\alpha \ell j} \exp(i\theta_1^{\alpha \ell})(E - E_{2r} + \frac{i}{2}\Gamma_2^{\gamma}) + g_2^{\gamma} g_2^{\alpha \ell j} \exp(i\theta_2^{\alpha \ell})(E - E_{1r} + \frac{i}{2}\Gamma_1^{\gamma})}{(E - E_{1r} + \frac{i}{2}\Gamma_1^{\gamma})(E - E_{2r} + \frac{i}{2}\Gamma_2^{\gamma}) - |V|^2}$$

$$+ \frac{(g_1^{\gamma} g_2^{\alpha \ell j} \exp(i\theta_2^{\alpha \ell}) + g_2^{\gamma} g_1^{\alpha \ell j} \exp(i\theta_1^{\alpha \ell}))|V|}{(E - E_{1r} + \frac{i}{2}\Gamma_1^{\gamma})(E - E_{2r} + \frac{i}{2}\Gamma_2^{\gamma}) - |V|^2}.$$

This is the form of the T-matrix of interest, which will be referred to as the "overlapping doorway" equation.

2.5 Secondary Doorway States

To introduce secondary doorway states we take the idea of doorway states one step further. We assume that in Q space there exists a limited set of states that couple strongly to the doorway states. To define these secondary doorway states we extract from Q a subspace s, such that Q = s + R, where R describes the remainder of the Q space. Following the definition of the doorways (2-21), we introduce a complete set of eigenstates in s space, $\{\mu_s\}$, which is defined by

$$2\text{-}29 \qquad (E - H_{ss})|\mu_s\rangle = 0.$$

If we assume that μ_s and $\mu_{s'}$ are not coupled through the R space, we can rewrite the compound mixing of the doorway state (Wang, 1972) as

$$2\text{-}30 \qquad W_d^{\downarrow} = \sum_s \frac{|\langle \mu_d | h_{ds} | \mu_s \rangle|^2}{E - E_s - \Delta_s + \frac{i}{2}\Gamma_s} + \Delta_R - \frac{i}{2}\Gamma_R.$$

It should be noted that the compound shifts (Δ_s , Δ_R) and the compound widths (Γ_s , Γ_R) are the energy averaged values that one would expect to

see in a T-matrix which represents structure that varies over an energy range of the order of the intermediate resonances being discussed.

Now the situation of interest for us will be two interfering states, the first being a primary doorway (d=1) and the second being a secondary doorway (s=2). The following definitions will be appropriate in the secondary doorway case:

2-31
$$E_{dr} \equiv E_d - \Delta_d^{\uparrow} - \Delta_R$$
$$\Gamma_d \equiv \Gamma_d^{\uparrow} + \Gamma_R$$
$$E_{sr} \equiv E_s - \Delta_s.$$

Therefore the T-matrix in the case of a primary doorway and a secondary doorway becomes

2-32
$$T_{\ell j}^{\alpha} = \frac{g_1^{\gamma} g_1^{\alpha \ell j} \exp(i\theta_1^{\alpha \ell}) (E - E_{2r} + \frac{i}{2}\Gamma_2)}{(E - E_{1r} + \frac{i}{2}\Gamma_1)(E - E_{2r} + \frac{i}{2}\Gamma_2) - |V|^2}.$$

2.6 Overlapping versus Secondary Doorways

If we compare the equation for overlapping doorways (2-28) to the equation for a doorway and a secondary doorway (2-32), we notice that by setting $g_2^{\gamma} = 0$ and $g_2^{\alpha \ell j} \exp(i\theta_2^{\alpha \ell}) = 0$ in the former (2-28) it reduces to the same form as the latter (2-32). In other words, an overlapping doorway state with no gamma or particle escape width is effectively a secondary doorway state. To set only the gamma escape width to zero will result in an additional term in the secondary doorway state equation, which describes the particle escape nature of the state:

$$2\text{-}33 \qquad T^{\alpha}_{\ell j} = \frac{g_1^{\gamma} g_1^{\alpha \ell j} \exp(i\theta_1^{\alpha \ell}) (E - E_{2r} + \frac{i}{2}\Gamma_2) + g_1^{\gamma} g_2^{\alpha \ell j} \exp(i\theta_2^{\alpha \ell}) |V|}{(E - E_{1r} + \frac{i}{2}\Gamma_1)(E - E_{2r} + \frac{i}{2}\Gamma_2) - |V|^2}.$$

This is the form of the T-matrix which will be used in this thesis. Although it does not describe the situation which corresponds to the presence of a pure secondary doorway state, it is closely related to it, and in fact has been referred to as a secondary doorway state in the literature (Calarco, 1977; Woodworth, 1984). Therefore, we will stay with this nomenclature in this thesis, and equation (2-33) will be referred to as the "secondary doorway state" equation.

2.7 The Coupling Interaction Matrix Element

In the case of ^{13}C, as stated in the introduction, the primary and secondary doorway states have the same isospin. Therefore, one would expect that the interaction between these two states would be dominated by the strong force. In order to test this idea we have calculated the magnitude of the coupling interaction matrix element $|V|$ of equation (2-33) in the context of the nuclear shell model. Using the particle-hole formalism, we used the ^{12}C nucleus as a core in which the $1s_{1/2}$ and $1p_{3/2}$ neutron and proton subshells are filled. The ^{13}C ground state is then a 1p state, the primary state a 2p-1h state, and the secondary state a 3p-2h state. An illustration of a possible configuration for each of these three states is shown in Figure 2-2. It should be noted that these are not the only possible configurations for these states. Shell model calculations by Marangoni, Ottaviani, and Saruis (Marangoni, 1974) say that the strongest transitions for electric

Figure 2-2

A possible shell model configuration in ^{13}C for each of the three states: ground, primary doorway, and secondary doorway.

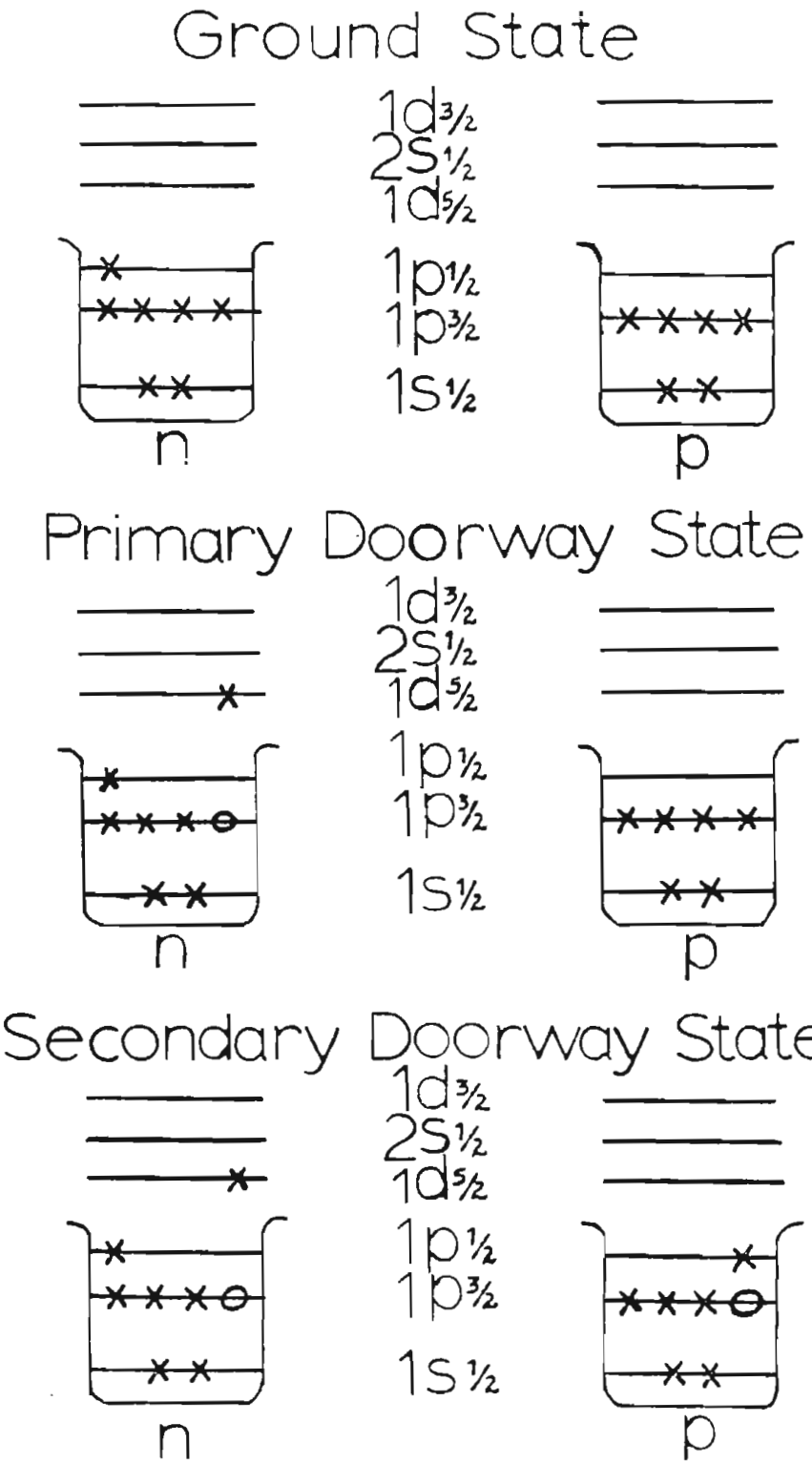
Ground State
1d3/2
2s1/2
1d5/2
1p1/2
1p3/2
1s1/2
n
p
Primary Doorway State
1d3/2
2s1/2
1d5/2
1p1/2
1p3/2
1s1/2
n
p
Secondary Doorway State
1d3/2
2s1/2
1d5/2
1p1/2
1p3/2
1s1/2
n
p

dipole absorption in this energy region in ^{13}C should be those promoting a particle from the p to the d shell. Of these, the main component of the giant dipole resonance is the $p_{3/2} \rightarrow d_{5/2}$ transition. We therefore restricted our primary state to these configurations. For our secondary state, the shell model calculations of Höhn (Höhn, 1979) indicate that, in the energy region from 10 to 26 MeV in ^{13}C, between 10 and 40 percent of the possible configurations should be 3p-2h. Of these, the important ones should be those that promote the particles up from the p subshells. We shall restrict ourselves to the simplest of these, where one goes from the 2p-1h to the 3p-2h configurations by promoting a particle from the $p_{3/2} \rightarrow p_{1/2}$ level.

One writes the various particle-hole states in terms of the two-body matrix elements between the various particles and holes by means of a straightforward recoupling algebra (Seyler, 1979; Rose, 1957; deShalit, 1963). The two-body shell model matrix elements (G-matrix elements) have been calculated by Dean Halderson (Halderson, 1979) using the two-body interaction of Bertsch, Borysowicz, McManus, and Love (Bertsch, 1977). The coupling order was chosen so that the particle-hole pair (in ^{13}C) could be coupled to a $J^{\pi} = 1^{-}$, T = 1 state, since this is physically consistent with the isovector electric dipole nature of the giant dipole resonance which is our primary doorway state. This form is:

$$2\text{-}34 \qquad \langle j_h^{-1} j_2(J_\gamma, T_\gamma) j_1(J,T) \,|V|\, [j_1^2(J_2, T_2) j_2]^{J_p, T_p} j_h^{-2}(J_h, T_h)(J,T) \rangle,$$

where, on the left, the particle-hole pair is coupled to a state having

total angular momentum J_γ and isospin T_γ, which is then coupled to the particle j_1 to produce a state (J,T). On the right, the three particles, coupled to total angular momentum and isospin J_p, T_p, combine with the two holes having total angular momentum and isospin J_h, T_h to form the state (J,T). The expansion of this coupling order in terms of the two-body matrix elements is shown in Table 2-1. The derivation of this expansion is shown in appendix A. Besides the one we have chosen, two other coupling orders were tried. First, the constraint of setting (J_γ, T_γ) to $(1^-, 1)$ was relaxed, and all possibilities were included. Second, the two particles were coupled first, then coupled to the hole on the left hand side. It was found that the average values were insignificantly different in all three cases.

We have calculated all non-vanishing matrix elements for J = 1/2 , 3/2 and T= 1/2, with the coupling order described above and with either a $d_{5/2}$ or $d_{3/2}$ particle in the s-d shell. The other particles and holes were restricted to the p shell. The average values of these matrix elements, along with the two-body matrix elements from which they were generated, are shown in Table 2-2. These results were also presented in an earlier publication (Woodworth, 1984). In light of the fact, as stated above, that the matrix elements with a $d_{5/2}$ particle in the s-d shell are expected to dominate the giant dipole resonance in ^{13}C, it is interesting to note that the average value of the matrix elements with this restriction and the proper statistical weights is 0.8 MeV. This value will be compared with our experimental results later in this thesis.

Table 2-1. Expansion of the coupling interaction matrix element in terms of the two-body G-matrix elements.

$$\langle j_h^{-1} j_2(J_\gamma,T_\gamma) j_1(J,T) \,|V|\, [j_1^2(J_2,T_2) j_2]^{J_p,T_p} j_h^{-2}(J_h,T_h)(J,T) \rangle$$

$$= \langle \text{ TERM 1 } \rangle + \langle \text{ TERM 2 } \rangle$$

$$\langle \text{ TERM 1 } \rangle = \sum_{J_1,T_1} \begin{Bmatrix} j_h & j_2 & J_\gamma \\ j_1 & J & J_1 \end{Bmatrix} \begin{Bmatrix} 1/2 & 1/2 & T_\gamma \\ 1/2 & T & T_1 \end{Bmatrix} \begin{Bmatrix} J_p & j_h & J_1 \\ j_h & J & J_h \end{Bmatrix}$$

$$\cdot \begin{Bmatrix} T_p & 1/2 & T_1 \\ 1/2 & T & T_h \end{Bmatrix} \bar{J}_p \bar{T}_p \bar{J}_h \bar{T}_h \bar{J}_\gamma \bar{T}_\gamma \left(\bar{J}_1 \bar{T}_1\right)^2 (-1)^{j_1+j_2+j_h+J+T+3/2}$$

$$\cdot \frac{(1-(-1)^{-T_h-J_h})}{\sqrt{2}} \delta^{J_1 \; T_1}_{J_2 \; T_2} \left(\langle \text{ TERM 1a } \rangle + \langle \text{ TERM 1b } \rangle \right)$$

$$\langle \text{ TERM 1a } \rangle = (-1)^{J_x+T_x+J_1+T_1} \begin{Bmatrix} j_1 & j_1 & J_a \\ j_2 & J_p & J_x \end{Bmatrix} \begin{Bmatrix} 1/2 & 1/2 & T_a \\ 1/2 & T_p & T_x \end{Bmatrix} \begin{Bmatrix} j_1 & J_x & J_p \\ j_h & J_1 & j_2 \end{Bmatrix}$$

$$\cdot \begin{Bmatrix} 1/2 & T_x & T_p \\ 1/2 & T_1 & 1/2 \end{Bmatrix} \bar{J}_a \bar{T}_a \left(\bar{J}_x \bar{T}_x\right)^2 \frac{(1-(-1)^{-T_a-J_a})}{\sqrt{2}} \delta^{j_2 \; 1/2}_{J_y \; T_y}$$

$$\cdot \langle j_h j_2(J_x,T_x) \,|V|\, j_1 j_2(J_x,T_x) \rangle$$

$$\langle \text{ TERM 1b } \rangle = (-1)^{\bar{J}_a \bar{T}_a} \begin{Bmatrix} j_2 & J_a & J_p \\ j_h & J_1 & j_1 \end{Bmatrix} \begin{Bmatrix} 1/2 & T_a & T_p \\ 1/2 & T_1 & 1/2 \end{Bmatrix} \delta^{J_z \; T_z}_{j_1 \; 1/2}$$

$$\cdot \langle j_h j_1(J_a,T_a) \,|V|\, (j_1^2)(J_a,T_a) \rangle$$

Table 2-1. Continued

$$\langle \text{ TERM 2 } \rangle = \begin{Bmatrix} J_1 & j_1 & J_p \\ J_h & J & j_h \end{Bmatrix} \begin{Bmatrix} T_1 & 1/2 & T_p \\ T_h & T & 1/2 \end{Bmatrix} \begin{Bmatrix} j_2 & j_1 & J_1 \\ j_1 & J_p & J_a \end{Bmatrix}$$

$$\cdot \begin{Bmatrix} 1/2 & 1/2 & T_1 \\ 1/2 & T_p & T_a \end{Bmatrix} \begin{Bmatrix} j_h & j_2 & J_\gamma \\ j_1 & J & J_1 \end{Bmatrix} \begin{Bmatrix} 1/2 & 1/2 & T_\gamma \\ 1/2 & T & T_1 \end{Bmatrix} \frac{(1-(-1)^{-T_a-J_a})}{\sqrt{2}} \bar{J}_\gamma \bar{T}_\gamma$$

$$\cdot \bar{J}_a \bar{T}_a \bar{J}_p \bar{T}_p \bar{J}_h \bar{T}_h \left(\bar{J}_1 \bar{T}_1 \right)^2 (-1)^{J+T+J_a+T_a+j_1+j_2-j_h+3/2} \delta^{J_c}_{J_1} \delta^{T_c}_{T_1}$$

$$\cdot \delta^{J_k}_{j_h} \delta^{T_k}_{1/2} \langle (j_h^2)(J_h,T_h) \, |V| \, j_1 j_h (J_h,T_h) \rangle$$

The following notation is used in this table:

$$\bar{J} = (2J+1)^{1/2}$$

$$\delta^{A}_{B} = 1 \quad \text{if } A=B, \quad = 0 \quad \text{if } A \neq B.$$

The Wigner 6-j coefficients are represented by the symbols:

$$\begin{Bmatrix} j1 & j2 & j3 \\ j4 & j5 & j6 \end{Bmatrix}$$

Table 2-2. Two-body G-matrix elements and average values of the coupling interaction matrix element.

Two-body G-matrix elements

$\langle p_{3/2}p_{1/2}(J,T) \|V\| p^2_{1/2}(J,T) \rangle$	(J,T) = (1,0) : 1.725 MeV
$\langle p^2_{3/2}(J,T) \|V\| p_{1/2}p_{3/2}(J,T) \rangle$	(J,T) = (1,0) : 1.655 MeV
	(J,T) = (2,1) : -4.483 MeV
$\langle p_{3/2}d_{3/2}(J,T) \|V\| p_{1/2}d_{3/2}(J,T) \rangle$	(J,T) = (1,0) : 2.02 MeV
	(J,T) = (1,1) : 0.575 MeV
	(J,T) = (2,0) : -3.46 MeV
	(J,T) = (2,1) : 0.10 MeV
$\langle p_{3/2}d_{5/2}(J,T) \|V\| p_{1/2}d_{5/2}(J,T) \rangle$	(J,T) = (3,0) : -0.28 MeV
	(J,T) = (3,1) : -1.178 MeV
	(J,T) = (2,0) : 3.64 MeV
	(J,T) = (2,1) : 0.214 MeV

Average values of $|\langle 2p\text{-}1h|V|3p\text{-}2h\rangle|$

J	T	j_2	
1/2	1/2	$d_{3/2}$	1.209 MeV
3/2	1/2	$d_{3/2}$	0.962 MeV
1/2	1/2	$d_{5/2}$	0.675 MeV
3/2	1/2	$d_{5/2}$	0.850 MeV

3 EXPERIMENTAL TECHNIQUES AND EQUIPMENT

3.1 Introduction

The facilities at Triangle Universities Nuclear Laboratory, shown in Figure 3-1, were used in the acquisition of the data in this thesis. A deuteron beam incident on a ^{11}B foil was used to study the $^{11}B(d,\gamma_0)^{13}C$ reaction. For the case of the $^{12}C(n,\gamma_0)^{13}C$ reaction the experimental technique is not so straightforward. Neutron beams can not be accelerated directly, since neutrons are electrically neutral. The neutron beam was produced through the $^{2}H(d,n)^{3}He$ reaction by bombarding a deuterium-filled gas cell with a deuteron beam. The neutron beam thus produced was used to bombard a ^{12}C target, giving us the desired reaction. Consequences of producing neutron beams in this manner are poorer beam collimation and lower intensity than a charged particle beam. It is also true that neutron scattering in the target room can cause greater background problems than in the case of similar charged particle experiments. The gamma rays produced by both these reactions were observed with two NaI spectrometers.

3.2 Deuteron Beams

Unpolarized deuteron beams were produced by the direct-extraction negative ion source labeled in Figure 3-1 as Denis II. This beam was then accelerated through a model FN tandem Van de Graaff. It then proceeded through a pair of 90^{o} magnets and a 30^{o} bending magnet to get

Figure 3-1.

Triangle Universities Nuclear Laboratory. The NaI detectors used for the present work are located in Target Area # 4, on the hexagonally shaped track.

Cyclo-Graaff Laboratory

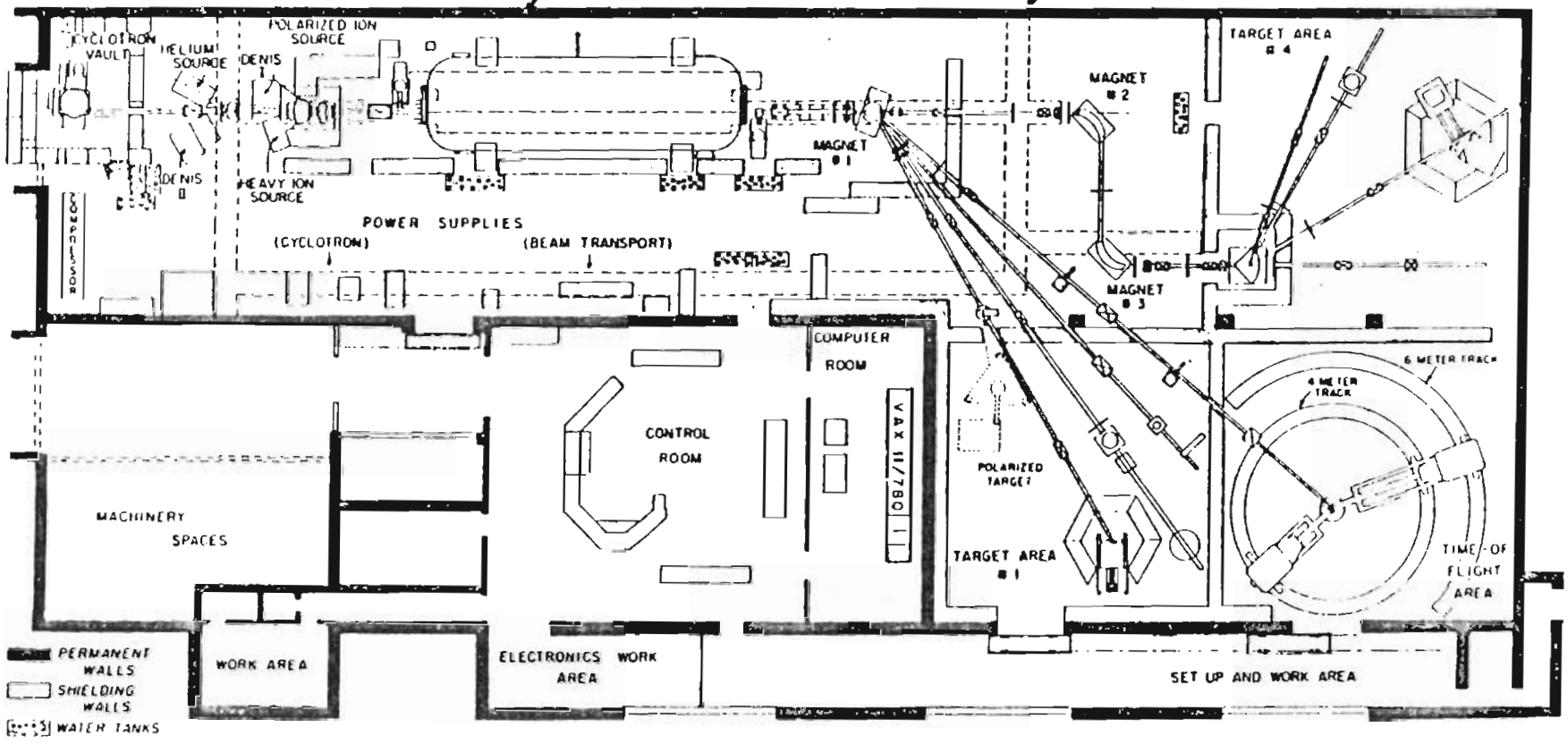

to the target room labeled number 4 in Figure 3-1, which contained the two NaI spectrometers. The beam was then passed through a quarter centimeter hole in a tantalum disk, used for collimation, before passing through the target foil. The beam on the collimation disk was minimized, but this procedure was not critical because of the high Q value (18.679 MeV) of the $^{11}B(d,\gamma_0)^{13}C$ reaction which produced gamma rays well seperated from those generated by stray beam. The beam ended up two meters into the lab wall in a tantalum lined Faraday cup. The integrated beam deposited in this Faraday cup was used in the determination of cross sections and in relative normalizations. Typical deuteron beam currents on target were in the range of 20 nA over the energy region corresponding to the $^{11}B(d,\gamma_0)^{13}C$ resonance. This was due to the fact that the high Q value of this reaction necessitated running the Van de Graaff with terminal voltages around one million volts, which is at the bottom of its designed energy range and resulted in poor transmission of the beam through the machine.

A lamb-shift polarized ion source (Clegg, 1970) was used to produce our polarized deuteron beams. Although this source produced lower intensity beams than the unpolarized source, the transmission through the Van de Graaff was fortuitously higher and the resulting on target beam intensities were similar to the unpolarized case. The beam polarizations were measured on the Faraday cup using the quench ratio method (Trainor, 1974). The beam polarization was typically 65 percent.

Vector and tensor deuteron beam polarizations for each of these magnetic substates as a function of magnetic field setting in the argon

Figure 3-2

Vector and Tensor beam polarizations for each of the magnetic substates as a function of magnetic field setting in the argon canal region of the polarized ion source. In this figure χ = B/B(critical), where B(critical) = 9.74 G is the field at which substate 3 would theoretically have no tensor polarization. The field at which substate 3 is actually purely vector polarized is below the theoretical value, and is shown by the arrow and dotted line in the figure (Clegg, 1970). The substates labeled 1 and 2 were used in the high field region to produce tensor polarized beams.

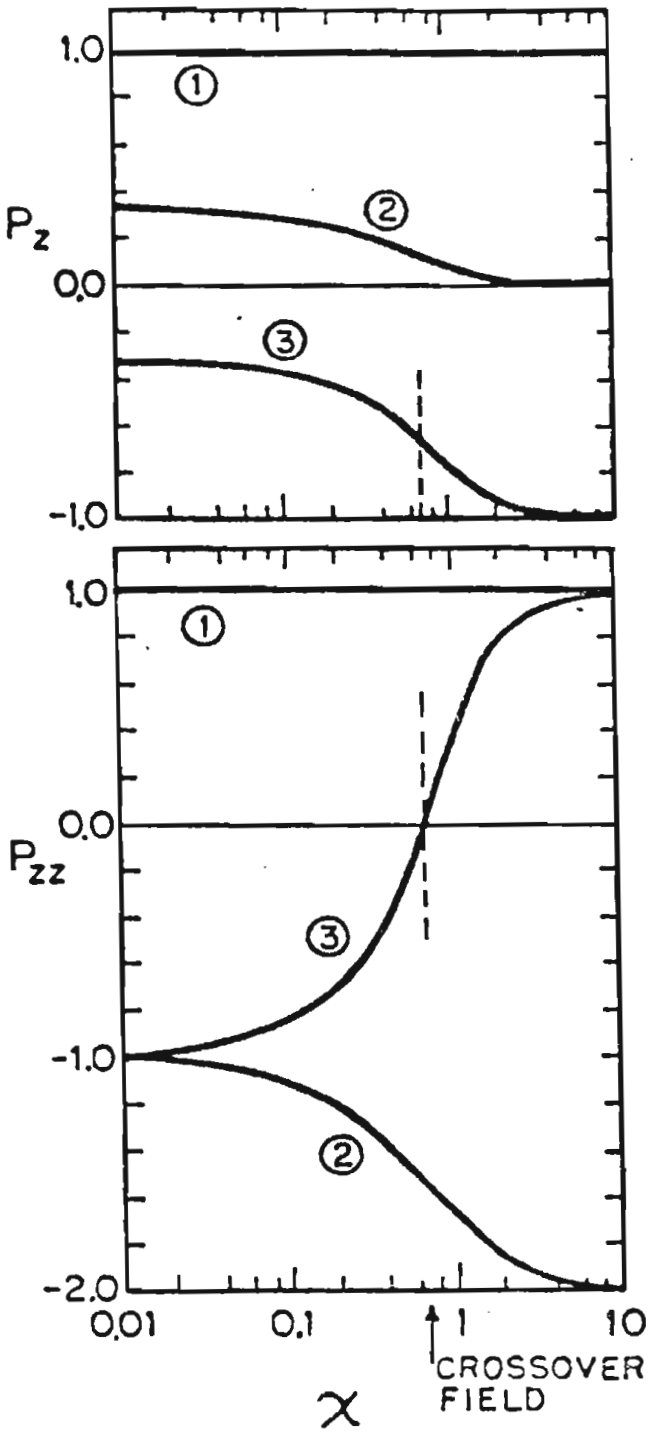
1.0
①
②
P_z
0.0
③
-1.0
1.0
①
0.0
P_{zz}
③
-1.0
②
-2.0
0.01
0.1
1
10
CROSSOVER FIELD
χ

canal region of the source are shown in Figure 3-2 (Tonsfeld, 1980). The arrow and dotted line show the setting used to produce a pure vector polarized beam (substate 3), while the substates labeled as 1 (m=1) and 2 (m=0) were used in the high field region ($\chi \sim 10$) to produce our tensor polarized beams.

3.3 Neutron Beams

The unpolarized and polarized deuteron beams used to make neutrons were produced as just mentioned with the addition that in each case the beam was pulsed before being injected into the Van de Graaff. The unpolarized deuterons were passed through a radio frequency chopper and a double drift buncher, producing a 2 nsec beam burst at a repetition rate of 2 MHz. This produced on target beam currents which were limited to 150 nA because of count rate limitations in the spectrometers. The polarized deuterons were ramped at the source and then sent through a double drift buncher and a chopper (Wender, 1980). This produced a beam burst on target of 2-3 nsec at a repetition rate of 4 MHz. The on target beam currents were typically 80 nA.

After passing the deuteron beam through a 7.6 cm long by 1.0 cm in diameter copper tube that served as a capacitive pickup to mark the arrival of the beam burst; the beam passed through a 0.4 cm hole in a tantalum disk used for collimation. The beam hitting the collimator was kept less than 1 nA in unpolarized runs and less than 5 nA in polarized runs. The beam then proceeded through an electron suppressor and into a

deuterium gas cell filled to a pressure of 6 atm. The entrance to the cell was a 5.6 μm Havar foil. The cell itself was 2.5 cm long and lined with tantalum. The integrated charge of the beam was collected in this cell for the purpose of relative normalizations and determinations of cross sections. The $^{2}H(d,n)^{3}He$ reaction produces forward peaked neutrons, most of which are in a 20^{o} cone. A computer program calculated the deuteron beam energy needed to produce the desired neutron energy in the center of the gas cell. This program allowed for energy loss in the entrance foil and in the gas. At the lowest part of the energy range studied (6.5 MeV neutrons) the energy spread of the neutron beam was on the order of a half of an MeV, while at the highest part (18.5 MeV neutrons) it was less than 200 keV. Therefore, for a few energies at the highest end of the range, the pressure in the cell was increased to about 7 atm which gave a somewhat greater beam spread, but still much less than the spread down at the low end of the energy range. This gas cell is shown in Figure 3-3.

Polarized neutrons were obtained by virtue of the excellent polarization transfer of the $^{2}H(\vec{d},\vec{n})^{3}He$ reaction (Lisowski, 1973). The polarized source was operated in a state where the vector and tensor beam polarizations were equal ($P_{zz} = P_{z} \equiv P_{d}$). Therefore, in the case of our experiments, the neutron polarization can be expressed as

$$P_{n} = \frac{0.95}{0.12 + P_{d}^{-1}}. \qquad 3\text{-}1$$

Also, the 0^{o} cross section is higher for tensor polarized deuterons than for unpolarized deuterons, so that

Figure 3-3

The neutron production target assembly. The one-inch long cell on the left was typically filled with deuterium gas to a pressure of 6 atm.

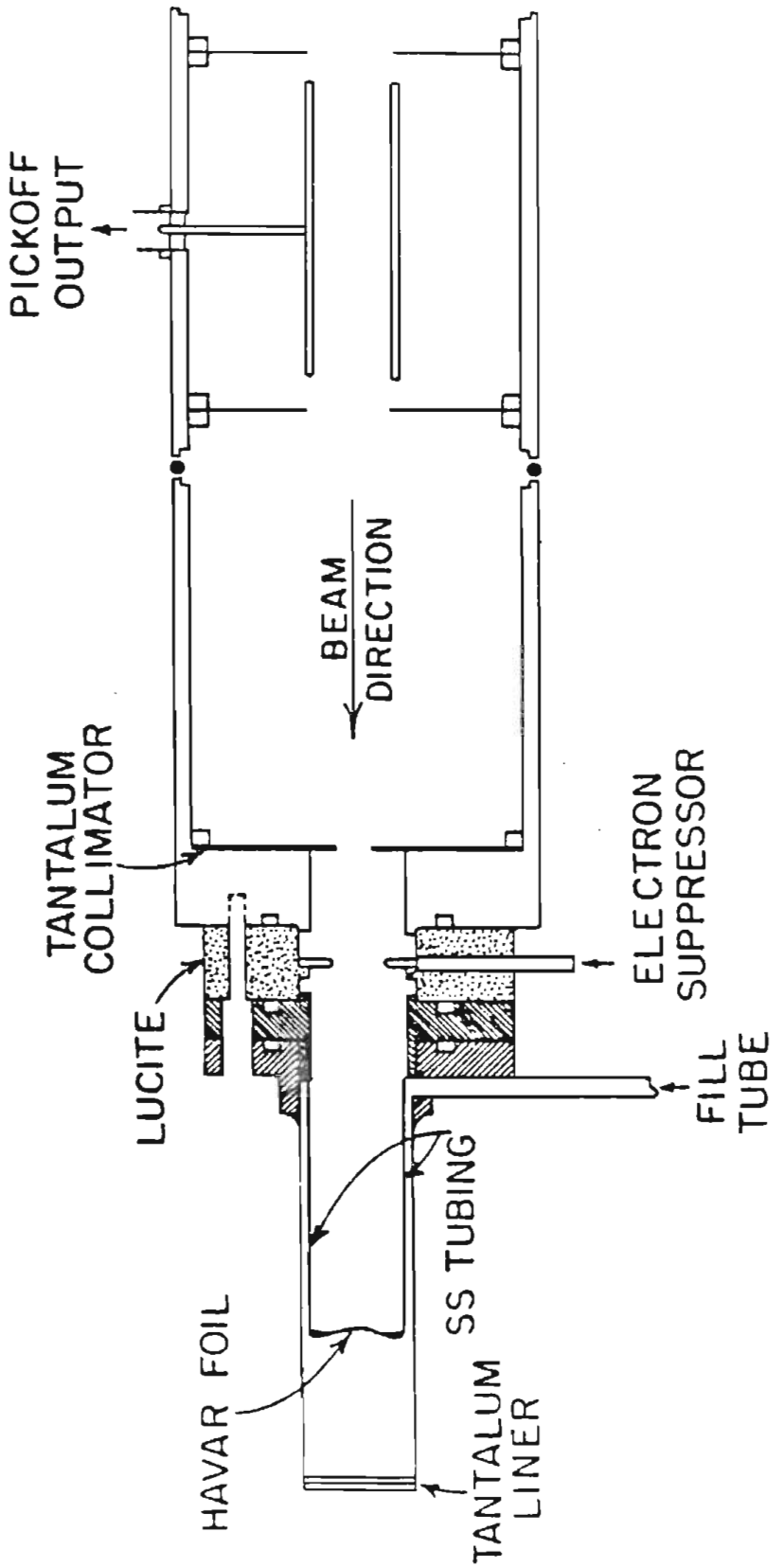
PICKOFF
OUTPUT
BEAM
DIRECTION
TANTALUM
COLLIMATOR
LUCITE
ELECTRON
SUPPRESSOR
FILL
TUBE
SS TUBING
HAVAR FOIL
TANTALUM
LINER

3-2 $\sigma(0^{o}) = \sigma_{u}[1.0 + 0.12P_{d}]$,

where σ_u is the unpolarized 0^{o} cross section for the $^{2}H(d,n)^{3}He$ reaction. Equations 3-1 and 3-2 are from Lisowski (Lisowski, 1973), while the 0^{o} $^{2}H(d,n)^{3}He$ cross sections are from Drosg (Drosg, 1978).

3.4 ^{11}B Targets

The targets for the $^{11}B(d,\gamma_0)^{13}C$ reaction study were self-supporting foils of ^{11}B isotope (98 percent enriched). The targets were made by vacuum deposition of the ^{11}B isotope onto glass slides. The ^{11}B isotope was placed into a tantalum crucible and covered with a small layer of potassium chloride. The crucible was at the focus of an electron gun, above which were suspended glass slides. The whole assembly was in an evacuated bell jar. The electron gun then heated up the contents of the crucible, causing a small layer of potassium chloride to be deposited on the slides first, followed by the deposition of the ^{11}B isotope. After cooling down, the ^{11}B foils were removed by placing the slides above a small tub of water such that only the very edge of the slides touched the water. The water level was then raised very slowly to allow the water to creep under the foils and dissolve the potassium chloride, allowing the foils to float free. The foils were then picked up on target rings, onto the back of which a few drops of glue were applied to hold them in place. The target rings were stainless steel rings about 1 mm thick and 2 cm in diameter, with the hole in the center being about 3/4 cm in diameter.

The targets produced in this manner were in the range of 100 $\mu g/cm^2$ in thickness. The target used in the cross section measurements was actually two targets, such as just described, placed one behind the other with a separation of about 2 mm. This double target had a thickness measured to be 232 $\mu g/cm^2$ with an uncertainty of about 10 percent. This target thickness was determined two ways: by comparison of the gamma ray yield of this target from the decay of the 15.11 MeV state in ^{12}C, populated by the $^{11}B(d,n)^{12}C$ reaction, with the yield of the same process for another ^{11}B target of known thickness (weighed to be 9.7 mg/cm^2); and by the observed energy loss of alpha particles from an ^{241}Am source passing through the target. The energy loss of the α particles was related to the target thickness using the computer program BABEL, which calculates the relationship using the relativistically correct Bethe Formula (Seltzer, 1964).

This double target suffered from the complication that if one were to rotate the target in the scattering chamber to an angle significantly different ($>15^o$) from the position where the target is normal to the beam, one can not then pass the beam through the target without hitting the target ring. We therefore kept the target normal to the beam and corrected for the effects of gamma ray attenuation through the target ring at detector angles where this could be the case. The correction factors were determined by a comparison made of the double target yield of the 15.11 MeV gamma ray decay in ^{12}C that was already mentioned, with the yield of the same decay for a single target that could be rotated. The ratio of target thicknesses was determined from a comparison of the

states seen in a charged particle monitor detector to be discussed later in this chapter. The maximum correction was 3 percent attenuation for the gamma rays at 90° with respect to the beam direction.

The energy loss of the deuterons in the ^{11}B double target ranged from about 65 keV down to 30 keV over the energy range which we studied (1.6 to 4.0 MeV). This is generally on the order of the energy spread of the deuteron beam, and it is taken into account in the analysis of the $^{11}B(d,\gamma_0)^{13}C$ reaction data in this thesis. Therefore, deuteron energies will be taken to mean center of target energies in this work, unless specifically referred to as deuteron beam energies.

3.5 ^{12}C Targets

The ^{12}C target was a 38.1 mm by 38.1 mm right-circular cylinder of graphite (natural carbon abundance, 99 percent) of mass 72.6 g. It was oriented with the symmetry axis perpendicular to the reaction plane. Various methods of dealing with background that was encountered when using this target are discussed in the following chapter.

3.6 Monitor Detectors

A silicon surface barrier detector was used as a monitor in the $^{11}B(d,\gamma_0)^{13}C$ reaction study. It was placed at backward angles relative to the beam direction, usually 150° to 165°, with 0° being defined as the beam direction. The detectors ranged from 400 to 2000 microns in

thickness and observed the charged particles generated in the d + ^{11}B reaction. The collimation for this detector was a 0.16 cm hole directly in front of the detector, with a 2.5 cm nose extending forward towards the target with a 0.32 cm collimator hole in it. In the $^{12}C(n,\gamma_0)^{13}C$ case a NE213 scintillator located at a distance of 260 cm from the target was used to monitor the neutron flux at 0^o. Pulse shape discrimination was used to separate the neutrons from the gamma rays. A time-of-flight spectrum was produced which clearly showed the neutrons from the $^{2}H(d,n)^{3}He$ reaction as well as the slower ones produced by deuteron breakup. Both monitors were used to verify the reliability of the beam current integration by comparing the relative number of counts in the monitor detectors for sequential runs to the relative total charge collected in those runs.

3.7 Gamma Ray Detectors

The gamma ray detectors used in this work were two 25.4 cm by 25.4 cm cylindrical NaI scintillators. Each was surrounded by a NE110 plastic anti-coincidence shield that was 12.5 cm thick (Suffert, 1968). Around this was passive shielding in the form of 10 cm of lead and 20 cm of lithium-carbonate-doped (50 percent by weight) paraffin. The paraffin moderates the fast neutrons and the thermal neutrons are attenuated by the lithium, because of the high cross section of the $^{6}Li(n,\alpha)$ reaction for thermal neutrons. Additionally, the right detector had a 0.15 cm sheet of cadmium, and the left detector a 0.6 cm boron-carbide-doped plastic sheet, set between the lead and the paraffin

for the purpose of thermal neutron attenuation. Boron and cadmium have high cross sections for the attenuation of thermal neutrons. The boron-carbonate-doped plastic was fifty percent by weight boron carbonate. Both detectors had tapered lead collimators such that the rear face of the detector was fully illuminated at the standard detector distance of 106 cm from the center of the target to the rear face of the scintillator. Both of these systems show a resolution of about 3 percent for 20 MeV gamma rays (Weller, 1980). This system is shown in the arrangement used for deuteron beams and a ^{11}B target in Figure 3-4. In the case of neutron beams and the ^{12}C target, additional passive shielding in the form of tungsten shadow bars was used to shield the detectors from neutrons produced in the gas cell. This arrangement is shown in Figure 3-5.

3.8 Electronics

A simplified schematic of the electronics associated with each of the NaI spectrometer systems is shown in Figure 3-6. The NaI detector was viewed by six gain matched RCA 8575 photo tubes. The anode signals from each tube were summed, amplified, and then clipped to 350 nsec by a partially terminated coaxial cable clipping line. The signal then went to both a fast linear gate and a TD101 differential discriminator. The TD101 contained two discriminators, one lower to provide timing information, while the other was set higher to provide the desired energy discrimination. The discriminator triggered a gate generator which opened the fast linear gate for 400 nsec, then held it closed for

Figure 3-4

Target and gamma ray detector geometry used in the $^{11}B(d,\gamma_0)^{13}C$ reaction study.

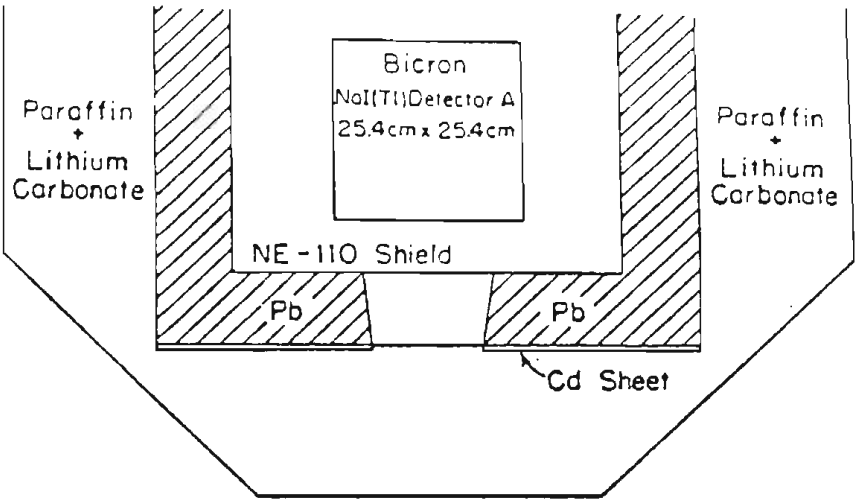
Bicron
NaI(Tl) Detector A
25.4cm x 25.4cm
Paraffin
+
Lithium
Carbonate
Paraffin
+
Lithium
Carbonate
NE-110 Shield
Pb
Pb
Cd Sheet

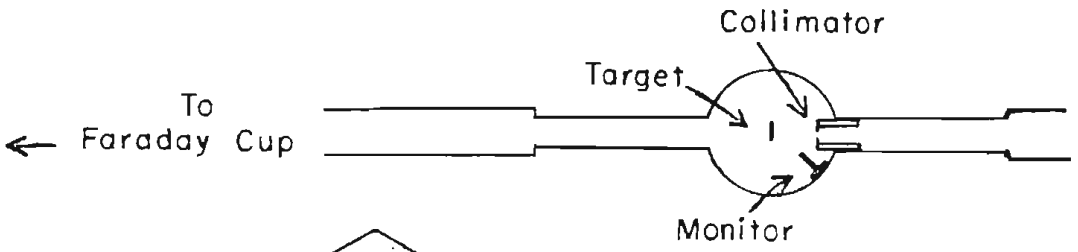
Collimator
Target
To
Faraday Cup
Monitor

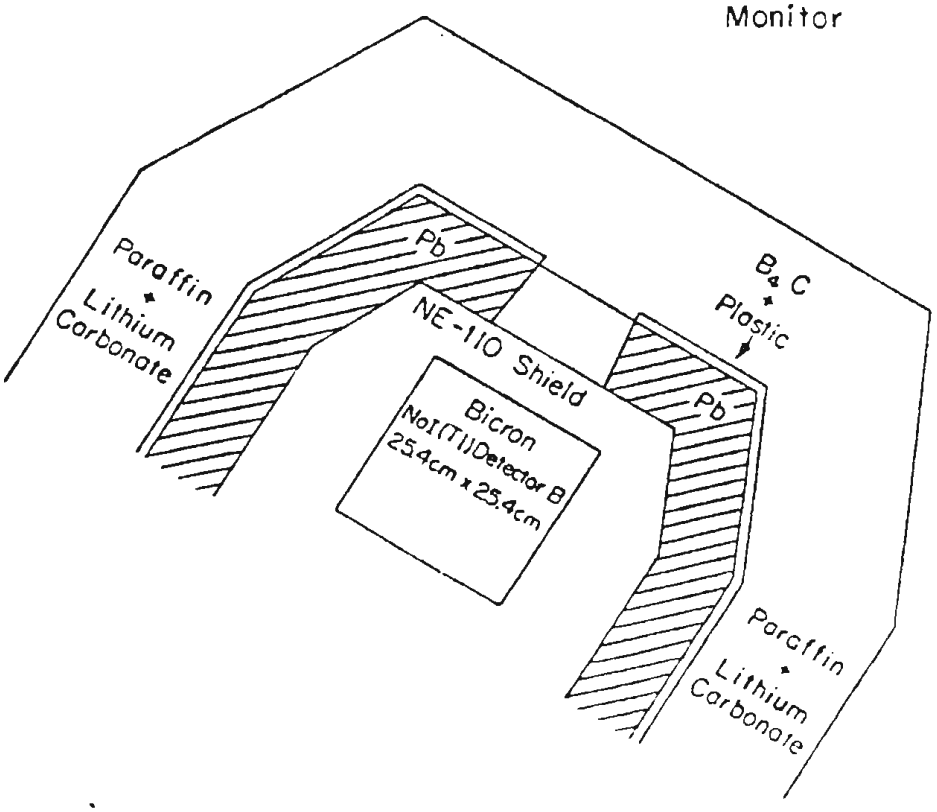
Paraffin
+
Lithium
Carbonate
Pb
NE-110 Shield
B4C
+
Plastic
Pb
Bicron
NaI(Tl) Detector B
25.4cm x 25.4cm
Paraffin
+
Lithium
Carbonate

Figure 3-5

Gas cell, target, and gamma ray detector geometry used in the $^{12}C(n,\gamma_0)^{13}C$ reaction study. The tungsten shadow bars used to shield the NaI detectors from the direct fast neutron flux are also shown here.

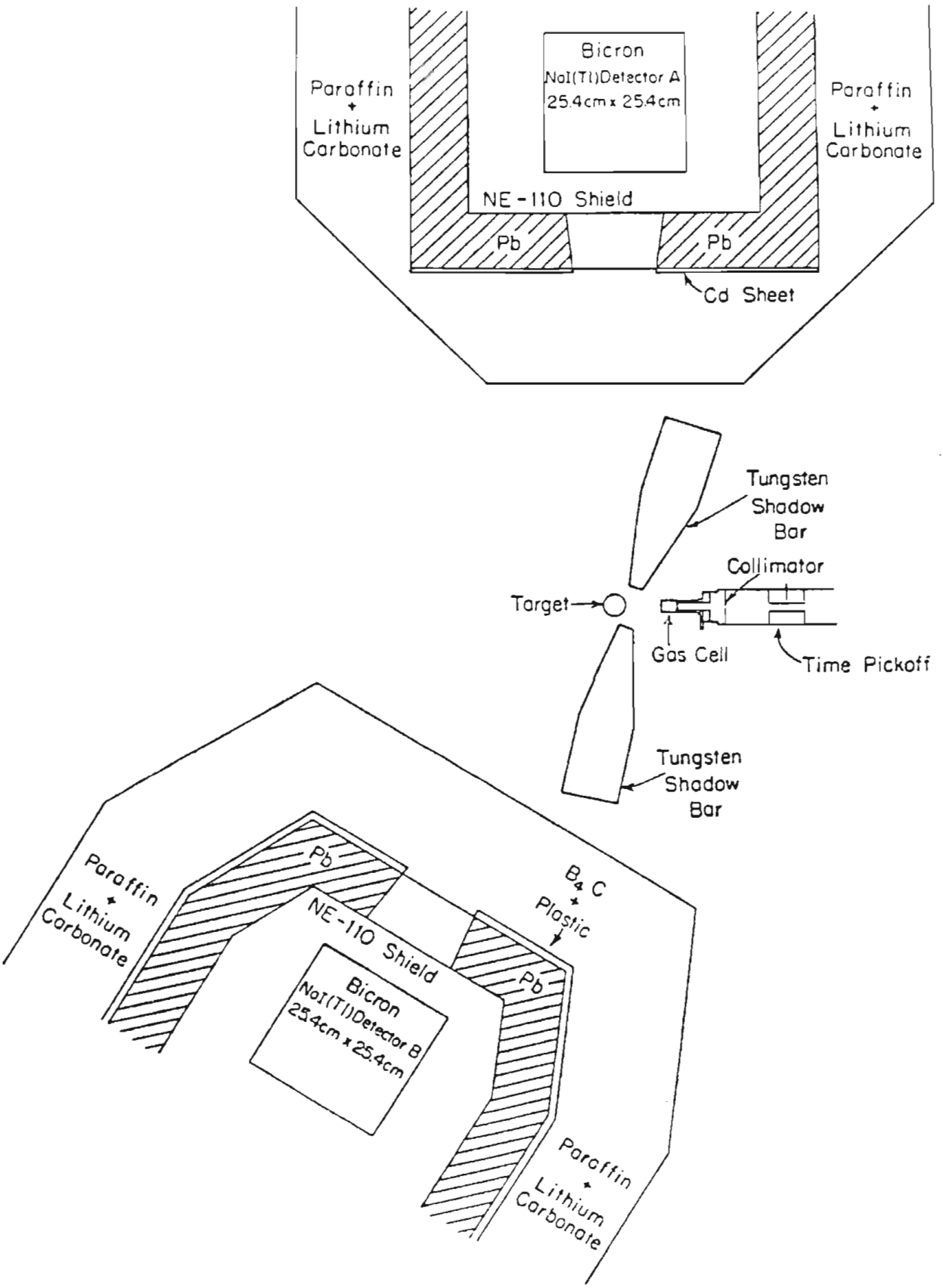
Bicron
NaI(Tl)Detector A
25.4cm x 25.4cm
Paraffin
+
Lithium
Carbonate
Paraffin
+
Lithium
Carbonate
NE-110 Shield
Pb
Pb
Cd Sheet
Tungsten
Shadow
Bar
Collimator
Target
Gas Cell
Time Pickoff
Tungsten
Shadow
Bar
Paraffin
+
Lithium
Carbonate
Pb
NE-110 Shield
B4C
+
Plastic
Pb
Bicron
NaI(Tl)Detector B
25.4cm x 25.4cm
Paraffin
+
Lithium
Carbonate

Figure 3-6

A simplified schematic of the electronics associated with the NaI spectrometer systems.

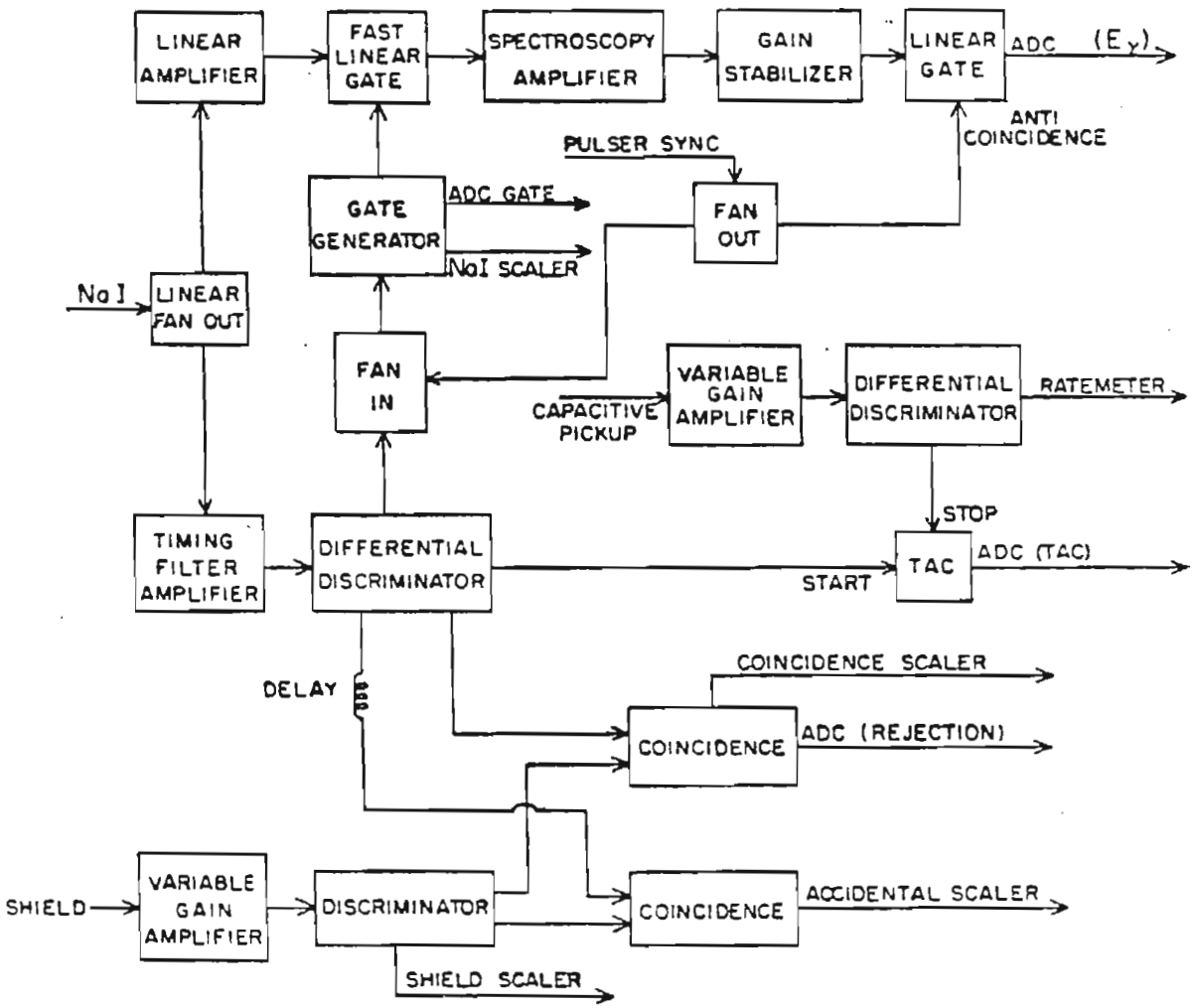
LINEAR AMPLIFIER
FAST LINEAR GATE
SPECTROSCOPY AMPLIFIER
GAIN STABILIZER
LINEAR GATE
ADC (E_Y)
ANTI COINCIDENCE
PULSER SYNC
GATE GENERATOR
ADC GATE
NaI SCALER
FAN OUT
NaI
LINEAR FAN OUT
FAN IN
CAPACITIVE PICKUP
VARIABLE GAIN AMPLIFIER
DIFFERENTIAL DISCRIMINATOR
RATEMETER
STOP
TIMING FILTER AMPLIFIER
DIFFERENTIAL DISCRIMINATOR
START
TAC
ADC (TAC)
COINCIDENCE SCALER
DELAY
COINCIDENCE
ADC (REJECTION)
SHIELD
VARIABLE GAIN AMPLIFIER
DISCRIMINATOR
COINCIDENCE
ACCIDENTAL SCALER
SHIELD SCALER

10 μsec. This arrangement reduced the effect of signal pile-up from the NaI detector. The linear signal was then amplified, passed through a Canberra 2050 analogue-digital gain stabilizer, and sent to an ADC. The Canberra 2050 module was employed to reduce the problem of occasional gain shifts in the NaI. It compensated for these shifts, which it monitored using a pulse from an LED located in the center of the rear surface of the NaI. This LED pulsed at a rate of 800 Hz and simulated a gamma ray with an energy chosen to be well below the region of the data. The LED pulse was gated out before the ADC to avoid causing dead time in the computer.

The pulses from the shield around the NaI crystal were sent through a variable gain amplifier, a fast discriminator, and then to a coincidence module along with the output of the NaI TD101 discriminator. Coincidences were events that occurred within 60 nsec of each other in both the NaI and the shield. The coincidence output was used to route the corresponding events into a different spectrum in the computer. This represented the rejected spectrum. Thus this method allowed us to reject cosmic rays and most of those events which do not deposit their full energy in the NaI or are below our desired discriminator threshold. Without this feature we would not have been able to extract the gamma rays of interest in this experiment from the spectrum. In order to correct for the effect of accidental coincidences, a second coincidence circuit was set up like the first, with the difference being that the shield pulses were now delayed by 330 nsec. This allowed us to monitor the rate of accidental coincidences,

which in these experiments ranged from less than 1 percent to 10 percent.

The efficiency and resolution of this system could be varied by changing the gain on the shield using the variable gain amplifier already mentioned. Two standard modes for which the efficiency has been measured were used. They are referred to as "high rejection" and "low rejection", where the former has greater energy resolution and lower efficiency than the latter. "High rejection" was typically used in the $^{11}B(d,\gamma_0)^{13}C$ study, while both rejection modes were used in the $^{12}C(n,\gamma_0)^{13}C$ case.

In the $^{12}C(n,\gamma_0)^{13}C$ investigation a pulsed beam was used, and a time-of-flight requirement was added to the system. The output of the NaI TD101 was sent to the start of a time-to-amplitude converter (TAC), and the time pick-off signal from the beam was sent to the stop. The TAC output was sent to an ADC, and a spectrum which clearly showed separation between neutron and gamma ray events was stored in the computer. A logical gate was set on the gamma ray peak in this spectrum so that the events corresponding to the gamma rays were stored in a separate spectrum from the other events. This allowed us to distinguish between gamma ray and neutron events in the NaI, and also to reduce background that is uncorrelated in time.

3.9 Data Acquisition

Each detector had three linear spectra sent to the computer: NaI

energy, TAC, and shield rejection logic. It should be noted that the shield rejection logic spectrum was not a true linear spectrum, but instead a logical signal where the presence of a signal indicated a coincidence between the NaI and Shield, and the absence of one indicated no coincidence. These signals were sent into the computer via a LeCroy 2259A 12 input ADC. Each detector also had four scaler signals associated with it: NaI counts, coincidence counts, accidental coincidence counts, and shield counts. Additional scalers fed into the computer were beam current integration (BCI), time pick-off, monitor gate scaler, and a time scaler. An additional linear spectrum was stored for the monitor energy signal in a separate ADC.

The data was acquired using a VAX 11/780 computer and the scalers were displayed on a VT100 computer terminal, both of which were manufactured by the Digital Equipment Corporation. The linear spectra were displayed on a Tektronix 4010 graphics terminal. The ADCs and scalers were resident in a CAMAC crate. The crate was interfaced to the computer system using a BiRa MBD-11 microprogrammed branch driver (Roberson, 1981). The XSYS software system (Gould, 1981) and the computer program CAP (King, 1983) were used for data acquisition.

A total of thirteen spectra were acquired for each NaI spectrometer. First the three linear spectra mentioned at the beginning of this section were accumulated. The shield rejection logic spectrum was used to sort the NaI energy spectrum into accepted and rejected (i.e. coincidence) spectra. The TAC spectrum had three logical gates set in it that sorted the accepted and rejected NaI spectra into spectra

corresponding to gamma ray events, events below the gamma ray time window, and events above the gamma ray time window. The TAC spectrum was itself sorted into three spectra corresponding to gates set in the NaI energy spectrum. Because runs usually took several hours to accumulate, the data was occasionally written onto tape and disk storage files and the data areas and scalers were then cleared. Therefore, the thirteenth data area was an accumulation of the data area corresponding to NaI energy events that were in the gamma ray TAC window and in the accepted spectra. One could choose not to clear this data area out when the others were cleared. A linear spectrum was also stored for the monitor energy signal. It should be noted that in the case of unpulsed beam, there were no TAC spectra and all events were automatically sorted as being gamma ray events. A typical linear spectrum for the unpulsed $^{11}B(d,\gamma_0)^{13}C$ case, and linear and TAC typical spectra for the $^{12}C(n,\gamma_0)^{13}C$ case are shown in Figure 3-7.

Besides storing and displaying the already mentioned scalers, various calculated values were also stored and displayed. The most relevant of these, which were used to correct the data offline, were computer dead times and accidental coincidence count rates. The dead times were calculated by comparing the number of stored linear signals to the number of associated scaler counts. These dead times for the NaI detectors were usually less than a percent. The accidental coincidence count rates were determined by the ratio of accidental coincidence to coincidence scaler counts.

Offline analysis of the NaI accepted spectra was done using XSYS

Figure 3-7

Typical spectra. The uppermost figure is an example of the accepted NaI energy spectra obtained in the $^{11}B(d,\gamma_0)^{13}C$ reaction study. The peak centered near 20.5 MeV corresponds to gamma rays going to the ground state of ^{13}C. The bottom two figures correspond to spectra obtained in the $^{12}C(n,\gamma_0)^{13}C$ reaction study, in which case the beam was pulsed. The middle figure is an example of the accepted, in the gamma ray TAC window, NaI energy spectra. The peak centered near 21 MeV corresponds to the gamma rays leading to the ground state of ^{13}C. The bottom figure is the corresponding time-of-flight TAC, with the gamma ray TAC window displayed.

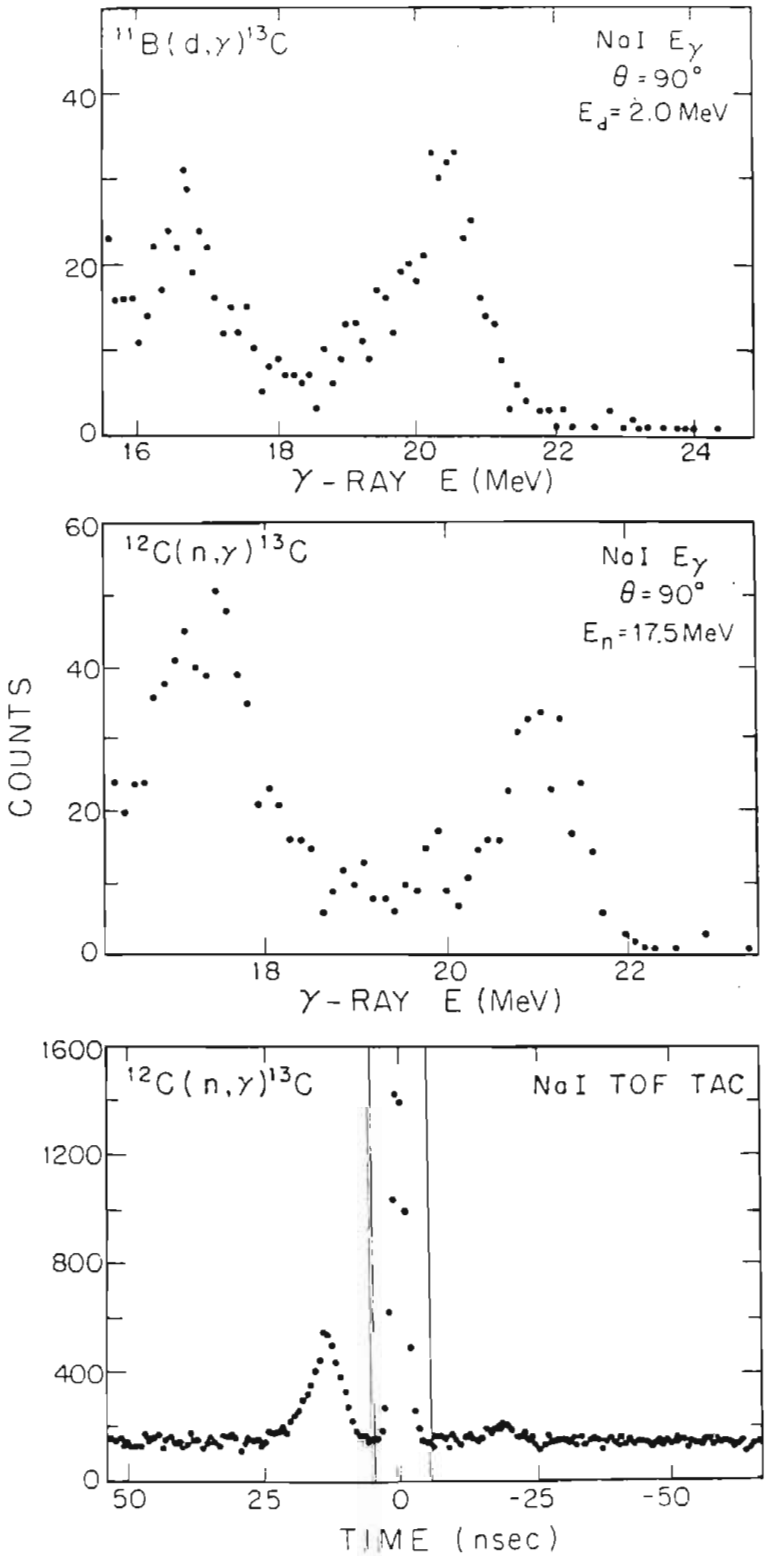
$^{11}B(d,\gamma)^{13}C$
NaI E_γ
$\theta = 90°$
$E_d = 2.0$ MeV
40
20
0
16
18
20
22
24
γ - RAY E (MeV)
$^{12}C(n,\gamma)^{13}C$
NaI E_γ
$\theta = 90°$
$E_n = 17.5$ MeV
COUNTS
60
40
20
0
18
20
22
γ - RAY E (MeV)
$^{12}C(n,\gamma)^{13}C$
NaI TOF TAC
1600
1200
800
400
0
50
25
0
-25
-50
TIME (nsec)

and the program MULFIT (King, 1983). This program fits the data to a standard line shape (Turner, 1978) of the response of the NaI detector. It corrects for accidental coincidence count rate and computer dead time, and normalizes to either BCI or to counts extracted from the monitor linear spectrum. The final results obtained from this program are as follows: a sum of the data in the region determined by the fit to be that of the peak; and a sum, in the same region, of the area under the line shape acquired from the fit. This latter sum can be used when unfolding multiple gamma ray peaks from the data. The program also allowed for various methods of background subtraction, the nature of which will be discussed in the next chapter.

4 ABSOLUTE CROSS SECTIONS

4.1 Cross Sections for the $^{11}B(d,\gamma_0)^{13}C$ Reaction

The cross section for a given angle and energy for this case is given by

$$\sigma(\theta,E) = \frac{N_\gamma}{N_d\, N_t\, \Omega\, \varepsilon}, \tag{4-1}$$

where N_γ is the number of counts in the detector for the gamma ray of interest, Ω is the solid angle of the detector, ε is the efficiency of the detector system, N_d is the number of deuterons incident on the target, and N_t is the number of target particles per unit cross section of the target.

N_γ was determined by the program MULFIT (King, 1983). This program fits the peak of interest to an empirically determined gamma ray response function (Turner, 1978) in order to determine the centroid and width (FWHM) of the peak. The peak is then summed 2 widths below and 1.1 widths above the centroid. This program also corrects this sum for dead time in the computer and for accidental count rejections in the spectrometer. In this experiment Ω was 0.045 sr for the detector distance of 41.75 inches, which was measured from the center of the target to the back face of the NaI crystal.

The efficiency (ε) is defined as the ratio of N_γ to the total number of gamma rays of the energy being studied that enter the collimator of the spectrometer. The method used for determining this

efficiency has been previously published (Weller, 1980). The data for the $^{11}B(d,\gamma_0)^{13}C$ reaction were taken with the spectrometer anticoincidence shields in the "High rejection" mode as described in the previous chapter. The efficiencies in this mode for the various gamma ray energies studied are shown in Table 4-1. In this table "Left Detector" refers to the detector to the left of the beam direction, and similarly for the other detector. For this study, 90° differential cross section measurements were taken over the region of the secondary doorway state resonance in ^{13}C. The combined measurements for the two detectors are tabulated in Table 4-2 and are shown in Figure 4-1. Total cross sections for this reaction can be determined at those energies where angular distributions were measured. The total cross section is

$$\sigma_T = 4\pi A_0, \qquad 4\text{-}2$$

where A_0 is an angle-independent quantity that can be extracted from the data, as will be seen in the next chapter. The values of these quantities are listed in Table 5-1 of that chapter. All cross sections contain an overall normalization error of ten to fifteen percent.

4.2 Cross Sections for the $^{12}C(n,\gamma_0)^{13}C$ Reaction

The cross section for a given energy and angle for this case is given by

$$\sigma(\theta,E) = \frac{N_\gamma \; f \; r_{gs}^2}{N_A \; N_d \; n_g \; \ell \; \sigma_n(0^{\circ}) \; \varepsilon \; \Omega}, \qquad 4\text{-}3$$

where ε, Ω, and N_d have the same definitions as in equation 4-1. N_γ

Table 4-1. "High rejection" spectrometer efficiencies, as used in the $^{11}B(d,\gamma_0)^{13}C$ reaction study.

	Efficiencies	
Gamma Ray Energy (MeV)	Left Detector	Right Detector
20.01	0.210	0.205
20.06	0.210	0.205
20.10	0.210	0.205
20.14	0.210	0.205
20.18	0.210	0.205
20.35	0.209	0.204
20.52	0.209	0.204
20.69	0.209	0.204
20.86	0.208	0.203
21.03	0.208	0.203
21.20	0.208	0.203
21.62	0.207	0.202
22.02	0.206	0.201

Table 4-2. 90° cross sections for the $^{11}B(d,\gamma_0)^{13}C$ reaction.

Deuteron Beam Energy (MeV)	Center of Target Energy (MeV)	90° Cross Section (μb/sr)
1.65	1.62	0.53 $\pm$ 0.03
1.70	1.67	0.70 $\pm$ 0.04
1.75	1.72	0.79 $\pm$ 0.04
1.80	1.77	0.83 $\pm$ 0.04
2.00	1.97	1.20 $\pm$ 0.06
2.20	2.18	0.80 $\pm$ 0.04
2.40	2.38	0.79 $\pm$ 0.04
2.60	2.58	0.61 $\pm$ 0.03
2.80	2.78	0.50 $\pm$ 0.03
3.00	2.98	0.59 $\pm$ 0.03
3.50	3.48	0.70 $\pm$ 0.04

Note: Errors shown represent the statistical uncertainties associated with the data.

Figure 4-1.

90^{o} excitation function of the $^{11}B(d,\gamma_0)^{13}C$ reaction. The plotted points are listed in Table 4-2. The error bars shown represent the statistical uncertainties associated with the data points.

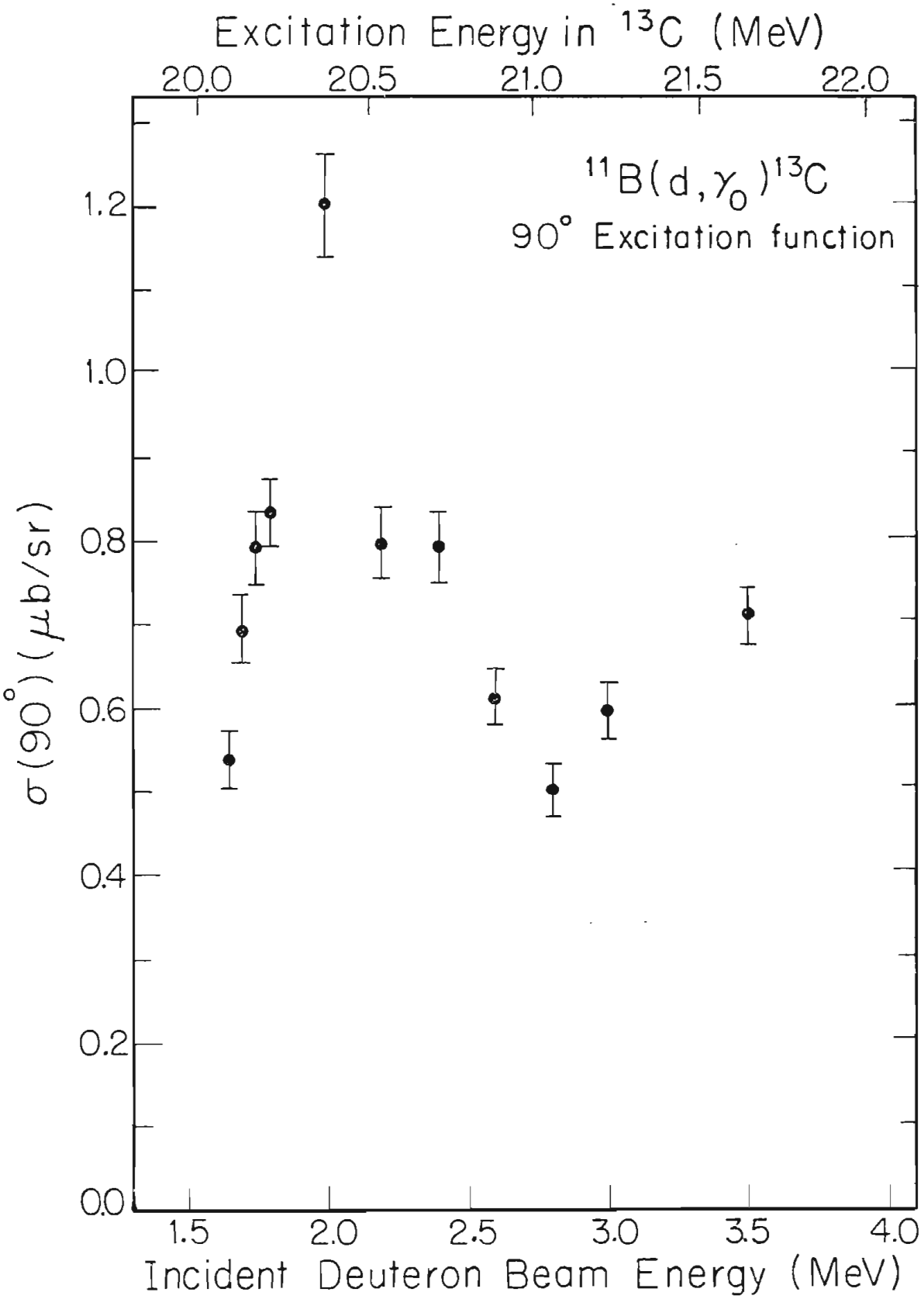
Excitation Energy in ^{13}C (MeV)
20.0
20.5
21.0
21.5
22.0
$^{11}B(d,\gamma_0)^{13}C$
90° Excitation function
1.2
1.0
0.8
0.6
0.4
0.2
0.0
$\sigma(90^\circ)$ (μb/sr)
1.5
2.0
2.5
3.0
3.5
4.0
Incident Deuteron Beam Energy (MeV)

differs however, due to the fact that the beam was pulsed for this reaction study. N_γ in this case includes a correction for missed beam pulse pickoffs; furthermore, N_γ now also reflects a background subtraction. It was found necessary with this reaction to take a background spectrum with no target in order to obtain the proper yields for the target-in spectrum. The counts in the target-out spectrum in the region of the peak were corrected for the same quantities as in the target-in spectrum, then normalized to the same amount of beam current integration as in the target-in spectrum and subtracted from the target-in peak. The subtracted peak was then used to generate N_γ. The anticoincidence shields in this study were run in both rejection modes. The efficiencies as a function of the various gamma ray energies studied are shown in Table 4-3. The notation in this table is the same as in Table 4-1.

N_A in equation 4-3 is the number of atoms in the target. The distance from the center of the gas cell to the center of the target (8.9 cm) is represented by r_{gs}. The density of deuterium in the gas cell in units of atoms/cm^3 is n_g. The length of the gas cell (2.54 cm) is ℓ. $\sigma_n(0^o)$, the 0^o differential cross section for the $^2H(d,n)^3He$ reaction in mb/sr, was taken from a work by M. Drosg (Drosg, 1978).

The final part of equation 4-3 is a finite geometry correction factor f. The Monte-Carlo code, SPINFIX, was used to generate this correction. A detailed description of this code can be found in a thesis by M. Jensen (Jensen, 1981). The code corrects for the effects of the finite size of the experimental apparatus, including the effects

Table 4-3. "Low rejection" and "High rejection" spectrometer efficiencies, as used in the $^{12}C(n,\gamma_0)^{13}C$ reaction study.

Gamma Ray Energy (MeV)	Efficiencies	
	Left Detector	Right Detector
* indicates "Low rejection" value.		
10.94	0.210	0.205
11.40	0.211	0.206
11.86	0.212	0.207
12.32	0.212	0.207
12.78	0.213	0.208
13.24	0.213	0.208
13.70	0.214	0.209
14.16	0.214	0.209
14.62	0.214	0.209
15.08	0.214	0.209
16.00	0.214	0.209
16.00	0.276*	0.262*

Table 4-3. Continued.

γ-Ray Energy (MeV)	Left Detector	Right Detector
17.38	0.213	0.208
18.53	0.212	0.207
19.13	0.273*	0.259*
19.22	0.211	0.207
19.68	0.210	0.206
20.05	0.210	0.205
20.05	0.271*	0.256*
20.60	0.209	0.204
20.78	0.270*	0.255*
20.97	0.208	0.203
21.06	0.208	0.203
21.70	0.207	0.202
21.70	0.267*	0.252*
21.98	0.267*	0.252*
22.25	0.206	0.201

of gamma ray attenuation, and neutron attenuation and multiple scattering in the target. The program also takes into account the large effects which arise from the energy dependence in the angular distribution of the neutrons, which is folded over the target geometry. Gamma ray cross sections (Storm, 1970) and neutron total and elastic scattering cross sections (Garber, 1973) were used in SPINFIX to generate the corrections. SPINFIX corrects the angular distributions taken with the neutron beam in different spin states seperatly. The program does not take into account effects due to polarization in the neutron elastic scattering. The correction factors at the various neutron energies used in the 90^{o} cross section measurements are shown in Table 4-4 as an example of the energy dependence of these factors. A typical example of the cross section data used in the input of SPINFIX, and the correction factors resulting, as a function of lab angle, are listed in Table 4-5. In this example "Spin Up" refers to incident neutrons with their spin polarized normal to the rotation plane of the detectors and pointed towards the ceiling. "Spin Down" is the same way except that it points towards the floor.

Differential cross sections were measured at 90^{o} in this study over the region of the pygmy and giant dipole resonances in ^{13}C. The combined data from the two detectors are tabulated in Table 4-6 and shown in Figure 4-2. A line obtained by drawing it through the major features of the data in a figure published in a study of the mirror reaction $^{12}C(p,\gamma_0)^{13}N$ (Berghofer, 1976) is shown in Figure 4-3 along with our $^{12}C(n,\gamma_0)^{13}C$ data for the purpose of comparison. It has been

Table 4-4. "SPINFIX" correction factors to the 90° excitation function of the $^{12}C(n,\gamma_0)^{13}C$ reaction.

Neutron Beam Energy (MeV)	Factor
6.5	1.6466
7.0	1.6616
7.5	1.6766
8.0	1.6916
8.5	1.7066
9.0	1.7216
9.5	1.7366
10.0	1.7516
10.5	1.7666
11.0	1.7812
12.0	1.8166
13.5	1.8582
15.5	1.9136

Table 4-4. Continued.

Neutron Beam Energy (MeV)	Factor
16.0	1.9316
16.4	1.9525
17.0	1.9616
17.5	1.9766
18.2	2.0163
18.5	2.0303

Table 4-5. Typical SPINFIX input and resulting correction factors.

Note: All angles are lab angles.

Incident neutron beam energy = 12.0 MeV

Gamma ray total absorption cross section = 0.333 barns

Legendre coefficients for neutron elastic scattering in mb/sr:

$A_0 \rightarrow A_6$: 72.34, 117.19, 148.29, 162.03, 91.14, 39.79, 28.21

Neutron total elastic scattering cross section = 1.44 barns

The resulting correction factors:

Angle	Unpolarized	Spin Up	Spin Down
50°	1.8713	1.8597	1.9037
55°	1.8617	1.8513	1.8896
60°	1.8555	1.8452	1.8785
70°	1.8405	1.8319	1.8561
90°	1.8166	1.8114	1.8238
100°	1.8108	1.8064	1.8163
110°	1.8036	1.8001	1.8077
125°	1.7989	1.7961	1.8018
130°	1.7967	1.7939	1.7994
140°	1.7940	1.7905	1.7971
150°	1.7819	1.7762	1.7869

Table 4-6. 90^{o} cross sections for the $^{12}C(n,\gamma_0)^{13}C$ reaction.

Neutron Beam Energy (MeV) at Center of Gas Cell	Energy Spread (MeV)	90^{o} Cross Section (μb/sr)
Note: * denotes 7 atm gas cell pressure, all others are 6 atm		
6.5	0.65	4.67 ± 0.36
7.0	0.57	4.82 ± 0.33
7.5	0.51	5.86 ± 0.39
8.0	0.46	4.85 ± 0.32
8.5	0.42	6.88 ± 0.32
9.0	0.39	6.87 ± 0.31
9.5	0.36	6.70 ± 0.30
10.0	0.33	4.96 ± 0.27
10.5	0.31	4.87 ± 0.27
11.0	0.30	4.22 ± 0.29
12.0	0.27	3.88 ± 0.18
13.5	0.23	2.86 ± 0.14
15.5	0.24*	2.16 ± 0.13

Table 4-6. Continued.

Neutron Beam Energy (MeV) at Center of Gas Cell	Energy Spread (MeV)	90° Cross Section (μb/sr)
19.72	16.0	0.23*	2.60 ± 0.16 ✓
20.09	16.4	0.22*	3.62 ± 0.22 ✓
20.64	17.0	0.22*	5.09 ± 0.29 ✓
21.10	17.5	0.21*	5.60 ± 0.33 ✓
21.75	18.2	0.20*	4.59 ± 0.29
22.02	18.5	0.20*	4.41 ± 0.26

Note: Errors shown represent the statistical uncertainties associated with the data.

Figure 4-2

90^{o} excitation function of the $^{12}C(n,\gamma_0)^{13}C$ reaction. The plotted points are listed in Table 4-6. The error bars shown represent the statistical uncertainties associated with the data points.

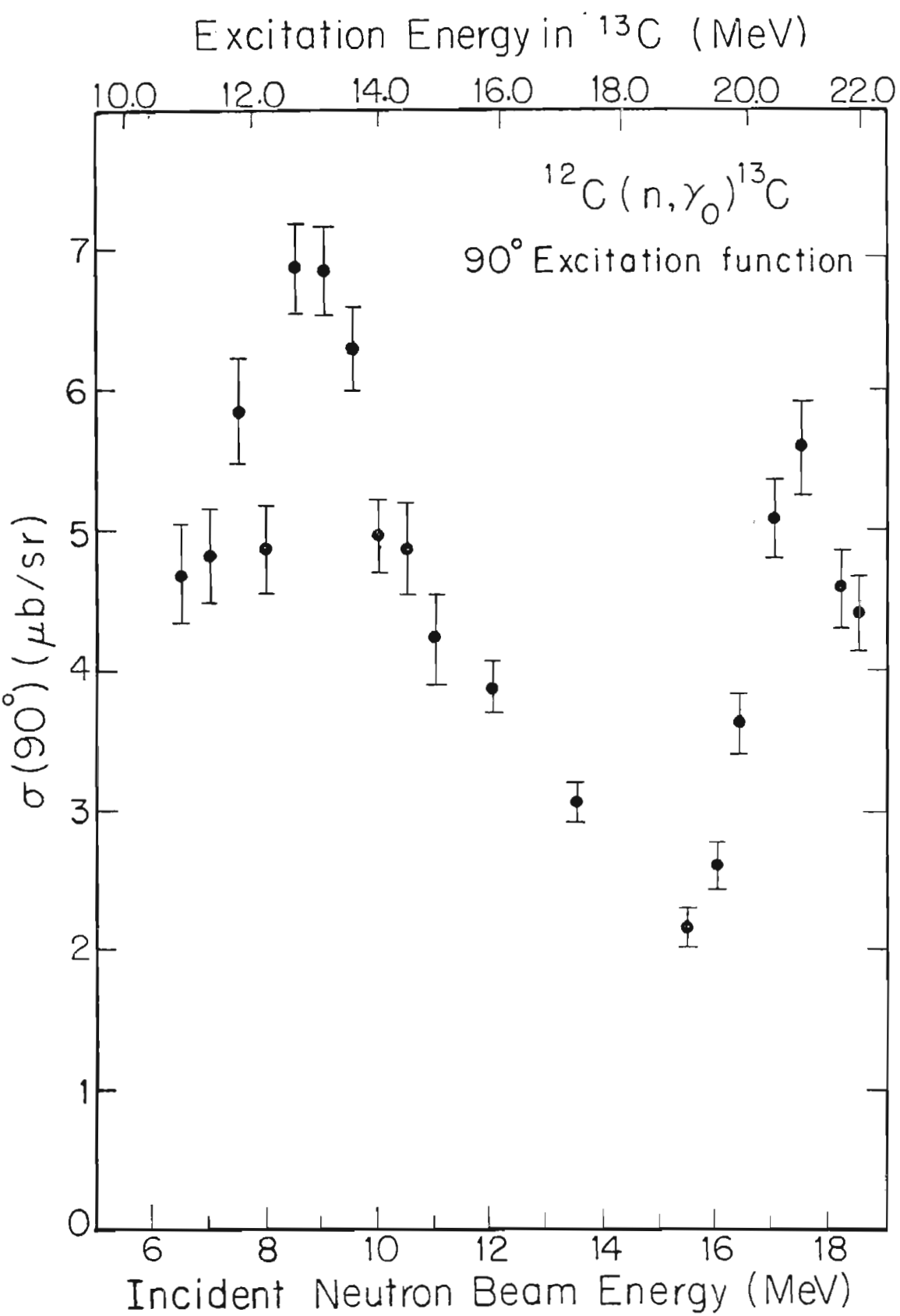
Excitation Energy in ^{13}C (MeV)
10.0
12.0
14.0
16.0
18.0
20.0
22.0
$^{12}C(n,\gamma_0)^{13}C$
90° Excitation function
$\sigma(90^\circ)$ (μb/sr)
0
1
2
3
4
5
6
7
6
8
10
12
14
16
18
Incident Neutron Beam Energy (MeV)

Figure 4-3

90^{o} excitation functions for the $^{12}C(n,\gamma_0)^{13}C$ and $^{12}C(p,\gamma_0)^{13}N$ reactions. The data for the former is from Table 4-6, while the data for the latter is from (Berghofer, 1976). The error bars shown represent the statistical uncertainties associated with the data points.

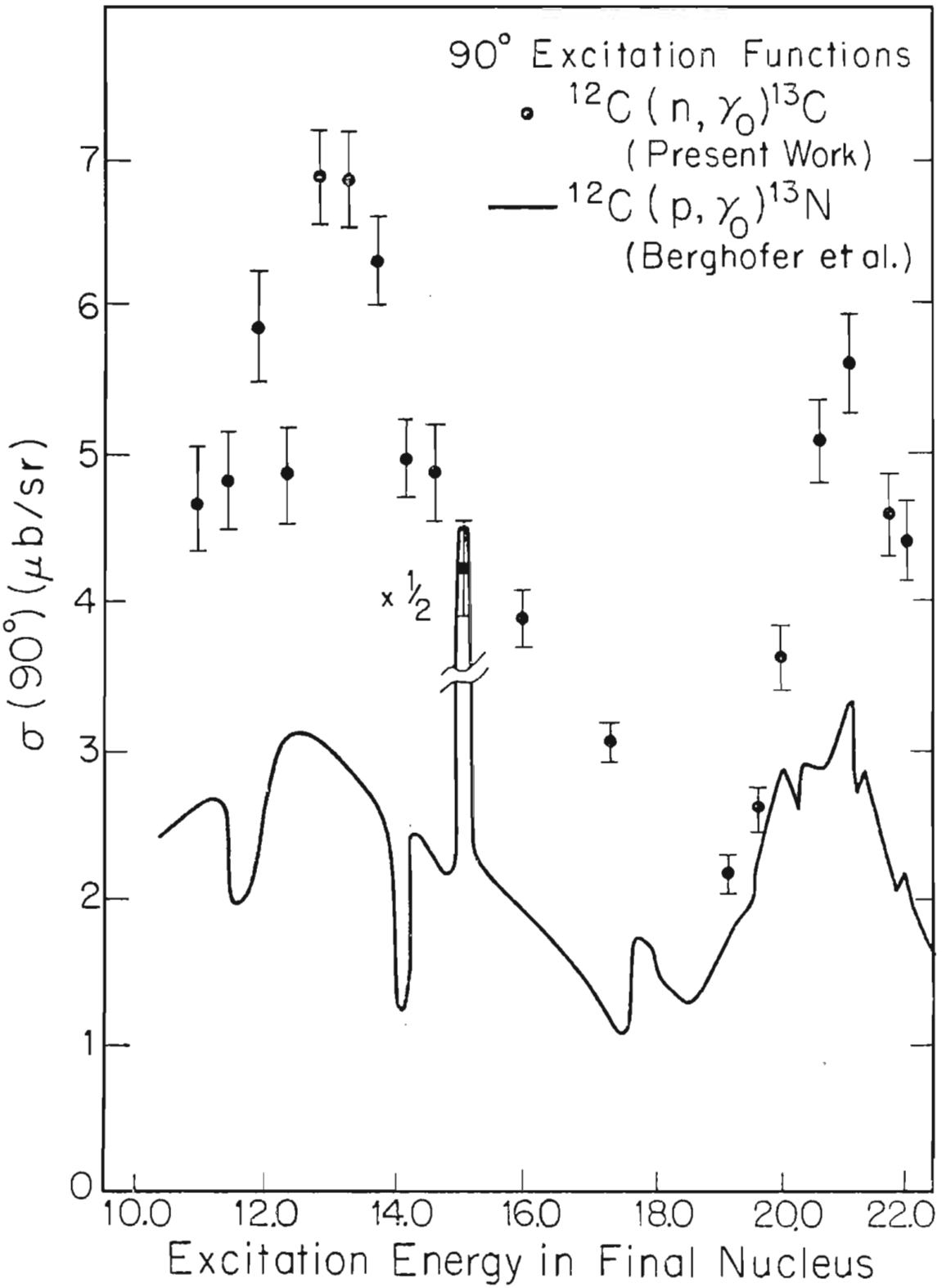
90° Excitation Functions
$^{12}C(n,\gamma_0)^{13}C$
(Present Work)
$^{12}C(p,\gamma_0)^{13}N$
(Berghofer et al.)
x ½
σ(90°) (μb/sr)
0
1
2
3
4
5
6
7
10.0
12.0
14.0
16.0
18.0
20.0
22.0
Excitation Energy in Final Nucleus

shown that Coulomb effects do not change the strong features of the cross section very much (Marangoni, 1977). The relative shapes of the cross section excitation functions in Figure 4-3 are in reasonable agreement with this statement, however, the absolute cross sections are larger by a factor of two in the $^{12}C(n,\gamma_0)^{13}C$ case, a feature for which there is, at present, no suitable explanation. Comparing our data to another study of the 90° cross sections of the $^{12}C(n,\gamma_0)^{13}C$ reaction (Bergqvist, 1984) and the detail balanced cross sections resulting from a study of the $^{13}C(\gamma,n_0)^{12}C$ reaction (Woodworth, 1979), gives the result that all three data sets have the same general features. The peaks of the pygmy and giant dipole resonances have approximatly the same relative cross section in all data sets, although both the $^{13}C(\gamma,n_0)^{12}C$ data and our data give the pygmy resonance a slightly higher cross section than the giant dipole resonance. The detail balanced absolute cross sections resulting from the $^{13}C(\gamma,n_0)^{12}C$ study are larger than ours by a factor of 1.4. The other $^{12}C(n,\gamma_0)^{13}C$ study (Bergqvist, 1984) gives the pygmy resonance a slightly smaller cross section than the giant dipole resonance. The absolute cross sections from this study are smaller than ours by factors ranging from 1.2 at the peak of the giant dipole resonance to 1.7 at the peak of the pygmy resonance. As already mentioned, equation 4-2 gives the total cross section at those energies where angular distributions of cross section were measured. The A_0 values are given in table 5-1. All cross sections contain an overall normalization error of ten to fifteen percent.

4.3 Photodisintegration Cross Sections

The time-reversed photodisintegration cross sections can be obtained from the radiative capture cross sections by the principle of detail balance. The equation which relates the two is

$$4\text{-}4 \qquad \sigma(\gamma,N_0) = 2\,\frac{2J_T+1}{2J_R+1}\,\frac{A_T}{A_R}\,\frac{E_x-Q}{E_x^2}\,M_pc^2\,\sigma(N,\gamma_0),$$

where J_T and J_R are the spins, while A_T and A_R are the atomic weights of the capture target and residual nuclei, respectively. M_pc^2 is the energy equivalent of the incident particle, Q is the Q-value of the capture reaction, and E_x is the excitation energy in the final nucleus before gamma ray emission. The photodisintegration cross sections are shown in Chapter 7 along with the results of the secondary doorway state analysis.

5 ANGULAR DISTRIBUTIONS

5.1 Angular Distribution Measurements

Angular distributions of cross section were measured for the $^{12}C(n,\gamma_0)^{13}C$ reaction at incident neutron energies of 12.0, 13.5, 14.75, 16.4, 17.2, 18.2 and 18.5 MeV. For the $^{11}B(d,\gamma_0)^{13}C$ reaction angular distributions of cross section were measured at incident deuteron beam energies of 1.6, 1.8, 2.0 and 4.0 MeV. Using a vector polarized beam, angular distributions of vector analyzing power were measured for the $^{12}C(\vec{n},\gamma_0)^{13}C$ reaction at incident neutron energies of 12.0, 14.75, 16.4 and 18.2 MeV; and for the $^{11}B(\vec{d},\gamma_0)^{13}C$ reaction at 2.0 and 4.0 MeV. Angular distributions of the tensor analyzing power $T_{20}(\theta)$ were taken with a tensor polarized deuteron beam at incident deuteron beam energies of 2.0 and 4.0 MeV. The vector polarized beam was also used with the $^{11}B(\vec{d},\gamma_0)^{13}C$ reaction to measure 55° and 125° vector analyzing powers at 1.6 and 1.8 MeV incident deuteron beam energies, and with the $^{12}C(\vec{n},\gamma_0)^{13}C$ reaction to measure 125° analyzing powers at 15.4, 17.4 and 18.8 MeV incident neutron energies.

5.2 Cross Section Angular Distributions

The angular distribution of the differential cross section can be expanded in terms of Legendre polynomials as

$$\sigma(\theta) = \sum_{k=0}^{k_{max}} A_k P_k(\cos\theta), \qquad 5\text{-}1$$

where the P_k are the Legendre polynomials and the A_k are the fitting coefficients. The data were fit by weighted least squares to

$$5\text{-}2 \qquad \sigma(\theta)/A_0 = 1 + \sum_{k=1}^{k_{max}} a_k P_k(\cos\theta),$$

where $a_k = A_k/A_0$. This form of the equation has the advantage of generating coefficients (a_k) which are independent of the absolute cross section, reflecting only the angular information of the distribution. The sum over k extends to $k_{max} \leq 2L$, where L is the multipolarity of the gamma ray transition. In both the $^{11}B(d,\gamma_0)^{13}C$ and $^{12}C(n,\gamma_0)^{13}C$ cases the data were found to be consistent with fitting to $k_{max} = 2$. This is in line with the expected dominance of electric dipole radiation in this region, as discussed in the Introduction. Pure E1 radiation would also have $a_1 = 0$ since the odd order Legendre coefficients are finite only if states of opposite parity are simultaneously being observed in the reaction. The fits in fact found the a_1 coefficients to be small, and refitting with $a_1 = 0$ did not change a_2 significantly. This fact was used at 15 MeV incident neutron energy to obtain an a_2 when only 125° and 90° cross section points were obtained. The Legendre polynomial fits to the angular distributions with more than three data points resulted in values of chi-square per point for these fits that were always less than 1.0, indicating a good fit to the data (Bevington, 1969). One can then be confident in extracting a_1 and a_2 coefficients from the distributions with only three data points which result in a exact fit, and therefore no value for chi-square. The fits to equation (5-2) are shown in Figure 5-1 for $^{12}C(n,\gamma_0)^{13}C$ and Figure 5-2 for $^{11}B(d,\gamma_0)^{13}C$. The A_0 and a_k coefficients obtained are listed in

Figure 5-1.

Angular distribution of cross section for the $^{12}C(n,\gamma_0)^{13}C$ reaction at various incident neutron energies. The curves are Legendre polynomial fits through k=2 as shown in equation (5-2). The error bars shown represent the statistical uncertainties associated with the data points.

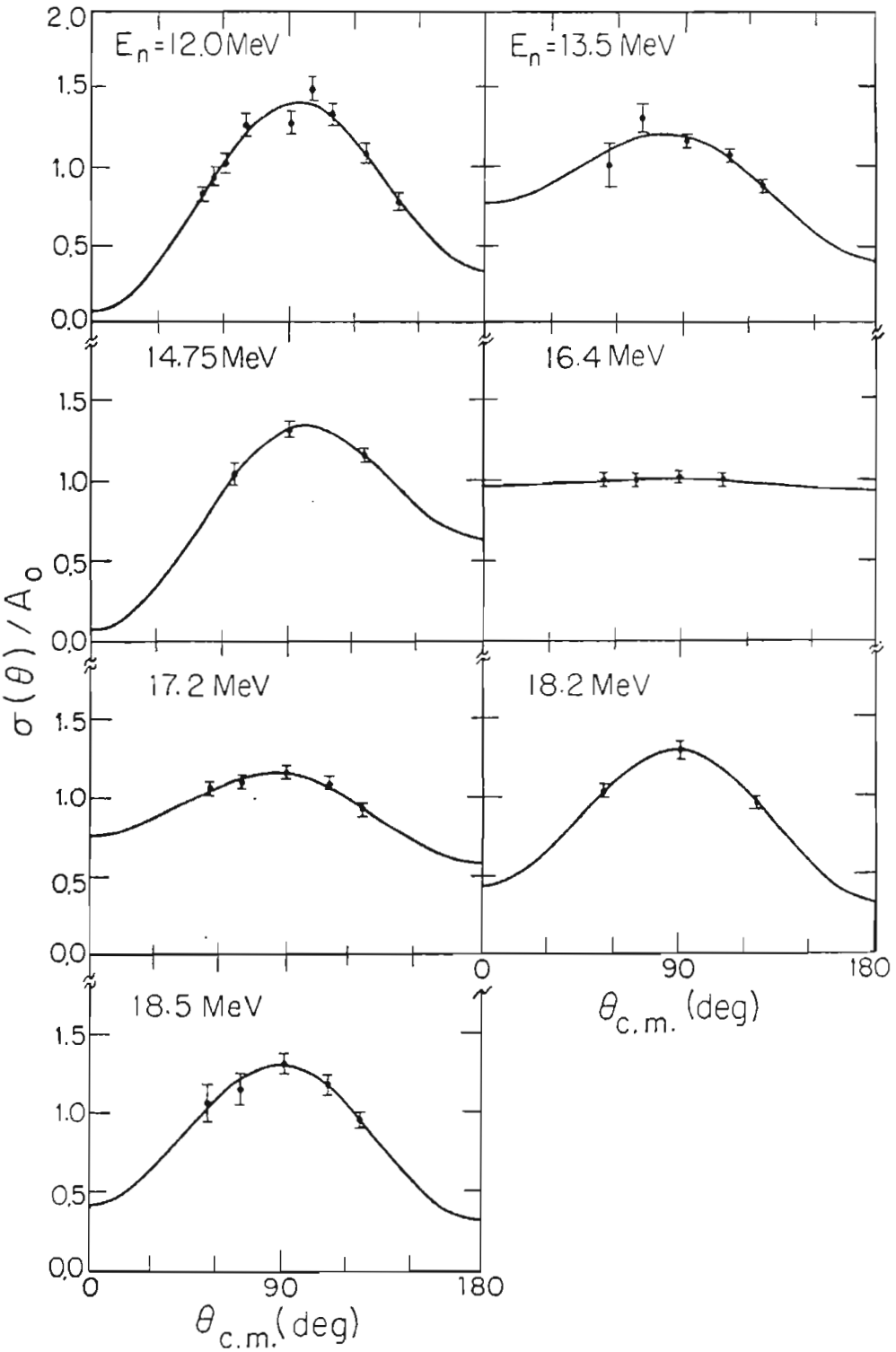
E_n=12.0MeV
E_n=13.5 MeV
14.75MeV
16.4 MeV
17.2 MeV
18.2 MeV
18.5 MeV
$\sigma(\theta)/A_0$
$\theta_{c.m.}$ (deg)
$\theta_{c.m.}$ (deg)
0.0
0.5
1.0
1.5
2.0
0
90
180

Figure 5-2

Angular distribution of cross section for the $^{11}B(d,\gamma_0)^{13}C$ reaction at various incident deuteron beam energies. The curves are Legendre polynomial fits through k=2 as shown in equation (5-2). The error bars shown represent the statistical uncertainties associated with the data points.

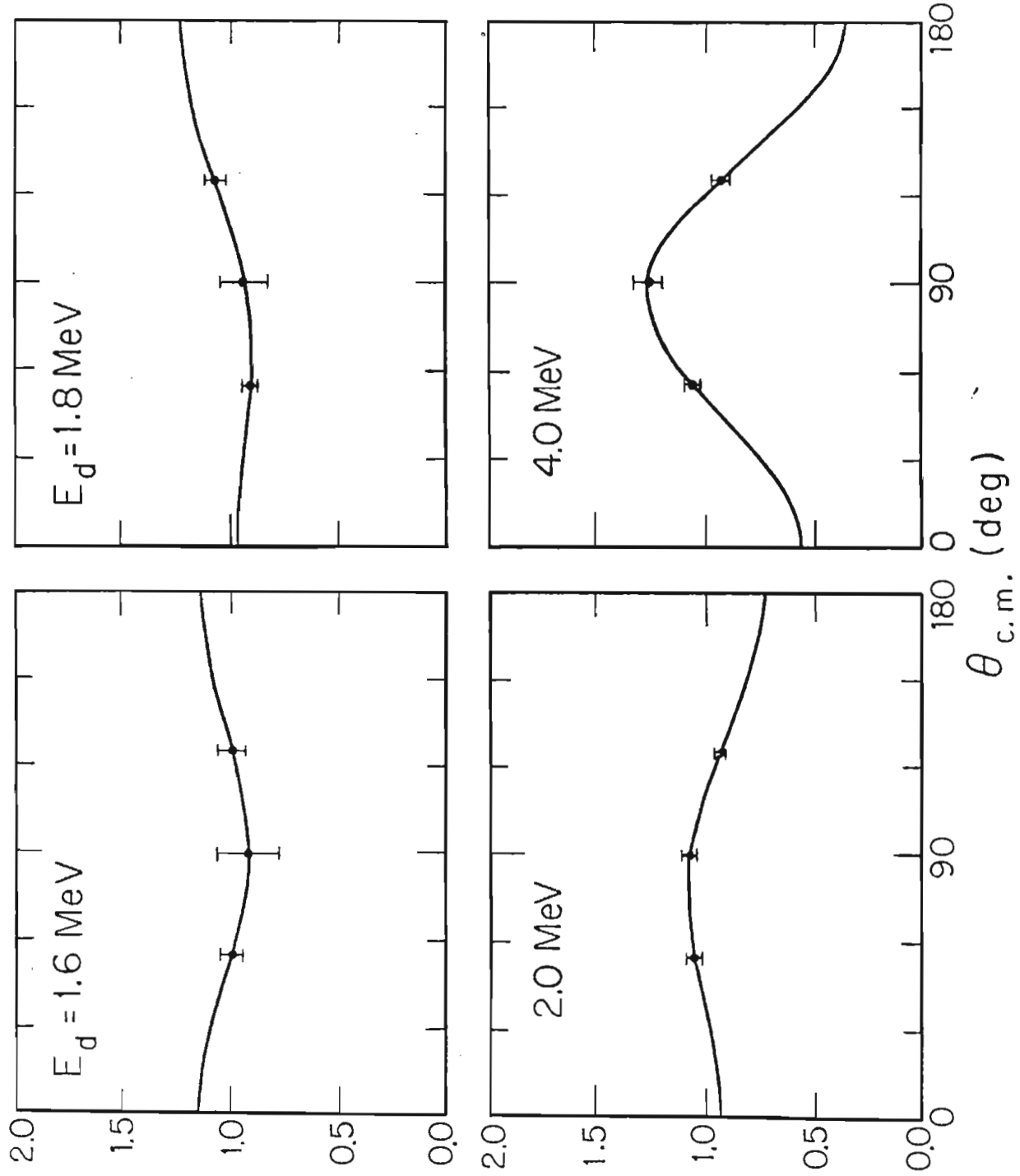
E_d = 1.8 MeV
E_d = 1.6 MeV
4.0 MeV
2.0 MeV
$\sigma(\theta) / A_o$
$\theta_{c.m.}$ (deg)
0.0
0.5
1.0
1.5
2.0
0
90
180

Table 5-1. A_0 and a_k coefficients.

$^{12}C(n,\gamma_0)^{13}C$

E_n(MeV)	E_x(MeV)	A_0(μb)	a_1	a_2
12.0	16.02	2.16 ± 0.18	-0.13 ± 0.04	-0.80 ± 0.08
13.5	17.40	2.27 ± 0.13	0.19 ± 0.08	-0.41 ± 0.15
14.75	18.56	1.80 ± 0.10	-0.29 ± 0.19	-0.64 ± 0.19
15.4	19.16	1.90 ± 0.09	*	-0.02 ± 0.14
16.4	20.08	3.38 ± 0.18	0.01 ± 0.08	0.02 ± 0.14
17.2	20.82	4.50 ± 0.11	0.09 ± 0.04	-0.32 ± 0.09
18.2	21.74	3.30 ± 0.09	0.04 ± 0.05	-0.64 ± 0.12
18.5	22.02	3.23 ± 0.17	0.04 ± 0.08	-0.62 ± 0.17

* Fit with $a_1 = 0.0$

$^{11}B(d,\gamma_0)^{13}C$

E_d(MeV)	E_x(MeV)	A_0(μb)	a_1	a_2
1.6	20.00	0.65 ± 0.10	0.00 ± 0.07	0.15 ± 0.30
1.8	20.17	0.96 ± 0.15	-0.14 ± 0.04	0.11 ± 0.22
2.0	20.35	0.99 ± 0.15	0.10 ± 0.03	-0.16 ± 0.07
4.0	22.06	0.45 ± 0.07	0.09 ± 0.04	-0.54 ± 0.14

Note: All non-exact fits have a chi-square per point of less than 1.0.

Table 5-1 along with their errors. These errors are the diagonal elements of the error matrix that results from a Legendre polynomial fit to the data (Bevington, 1969).

5.3 Analyzing Power Angular Distributions

Following the notation of Seyler and Weller (Seyler, 1979), the differential cross section for a polarized spin 1/2 beam is:

$$5\text{-}3 \qquad \sigma(\theta,\phi) = \sigma(\theta)[1+p_y A_y(\theta)].$$

$\sigma(\theta)$ is the unpolarized cross section, p_y is the beam polarization and $A_y(\theta)$ is the vector analyzing power. This leads directly to the expression for vector analyzing power for a spin 1/2 beam:

$$5\text{-}4 \qquad A_y(\theta) = \frac{1}{p_y}\frac{N_+ - N_-}{N_+ + N_-},$$

where N_+ is the number of spin up counts and N_- is the number of spin down counts defined according to the Madison convention (Barschall, 1970).

For two detectors at the same angle on opposite sides of the beam line this can be rewritten as:

$$5\text{-}5 \qquad A_y(\theta) = \frac{1}{p_y}\frac{r-1}{r+1}$$

$$\text{with} \quad r^2 = \frac{L_+ R_-}{L_- R_+},$$

where L_+ and R_+ have replaced N_+ for spin up in the left and right detectors respectively and similarly with L_- and R_-. This form of the

equation eliminates, to first order, systematic errors due to beam current integration and instrumental asymmetries.

For a spin one beam, again following Seyler and Weller (Seyler, 1979), the differential cross section becomes:

$$5\text{-}6 \qquad \sigma(\theta,\phi) = \sigma(\theta)[1 + \frac{3}{2}p_y A_y(\theta) + t_{20}T_{20}(\theta) + 2\mathrm{Re}t_{21}T_{21}(\theta) + 2\mathrm{Re}t_{22}T_{22}(\theta)].$$

This can also be expanded in terms of Legendre and associated Legendre polynomials such that

$$5\text{-}7 \qquad \sigma(\theta,\phi) = A_0 \sum_{k=0}^{k_{max}} [a_k P_k(\cos\theta) + b_k p_y P_k^1(\cos\theta) + c_k t_{20} P_k(\cos\theta) + d_k \mathrm{Re}t_{21} P_k^1(\cos\theta) + e_k \mathrm{Re}t_{22} P_k^2(\cos\theta)].$$

The Legendre polynomials used here are given by the formula

$$5\text{-}8 \qquad P_n(x) = \frac{1}{2^n n!}\frac{d^n}{dx^n}(x^2-1)^n$$

where $n = 0,1,2\ldots$

The associated Legendre polynomials are given by

$$5\text{-}9 \qquad P_n^m(x) = (1-x^2)^{m/2}\frac{d^m}{dx^m}P_n(x).$$

At this point it is useful to introduce the notation:

5-10

$x\text{-}z \equiv$ the plane of rotation of the detector system

$\hat{k}_{in} \equiv$ the beam direction (always in x-z)

$\hat{s} \equiv$ the polarization axis of the beam

$\beta \equiv$ the angle between $\hat{k}_{in}$ and $\hat{s}$

ϕ $\equiv$ the angle between x-z and $\hat{s} \times \hat{k}_{in}$,

such that with $\beta = 90^\circ$ and $\phi = 0^\circ$, $\hat{s}$ points up.

This notation is illustrated in Figure 5-3. This notation leads to (Darden, 1970):

5-11
$$p_y = P_z \sin\beta\cos\phi$$

$$t_{20} = \frac{P_{zz}}{2\sqrt{2}}(3\cos^2\beta - 1)$$

$$Ret_{21} = \frac{P_{zz}\sqrt{3}}{4}\sin 2\beta \sin\phi$$

$$Ret_{22} = \frac{-P_{zz}\sqrt{3}}{4}\sin^2\beta\cos 2\phi$$

for a deuteron beam, where P_z and P_{zz} are the vector and tensor beam polarizations, respectively.

To obtain the b_k coefficients of equation (5-7) for a deuteron beam, we run the polarized source in a state where $P_{zz} = 0$, $\beta = 90^\circ$, $\phi = 0^\circ$ for the state "+" and $\phi = 180^\circ$ for the state "-". This procedure was described in chapter 3. This allows us to write

5-12
$$\sigma_+ - \sigma_- = A_0(p_y^+ - p_y^-)\sum_{k=1}^{k_{max}} b_k P_k^1(\cos\theta)$$

$$\frac{\sigma_+}{p_y^+} - \frac{\sigma_-}{p_y^-} = \left(\frac{1}{p_y^+} - \frac{1}{p_y^-}\right)A_0\sum_{k=0}^{k_{max}} a_k P_k(\cos\theta)$$

$$A_0\sum_{k=0}^{k_{max}} a_k P_k(\cos\theta) = \left(\frac{\sigma_+}{p_y^+} - \frac{\sigma_-}{p_y^-}\right)\Big/\left(\frac{1}{p_y^+} - \frac{1}{p_y^-}\right)$$

$$= \frac{p_y^-\sigma_+ - p_y^+\sigma_-}{p_y^- - p_y^+}$$

Figure 5-3

This figure illustrates the polarization notation given in definitions 5-8.

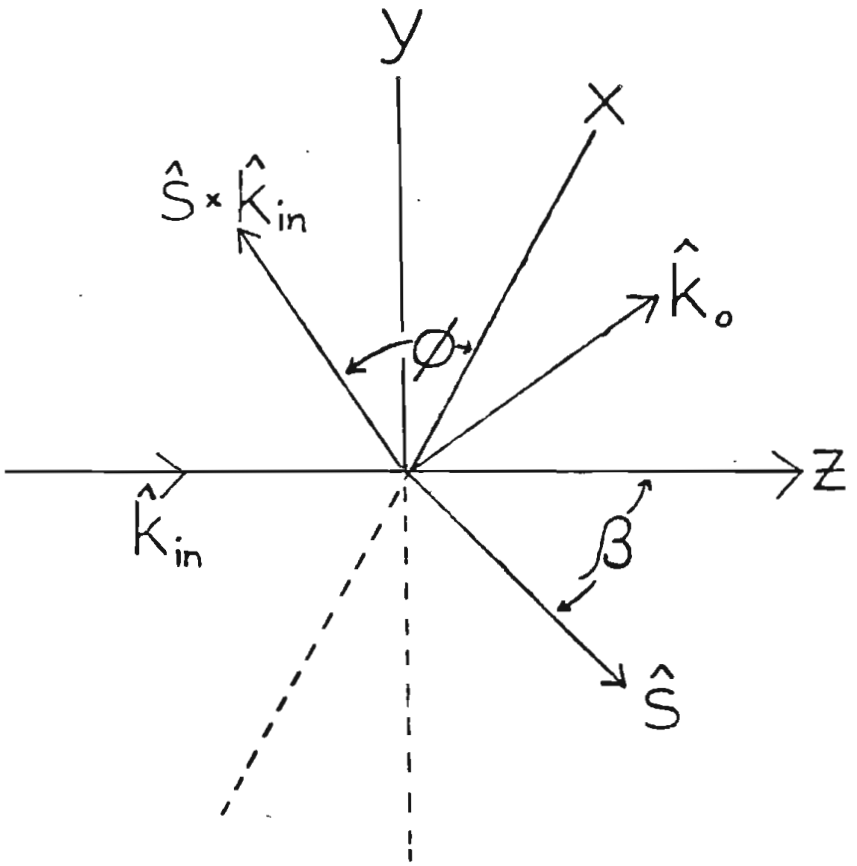
y
x
$\hat{S} \times \hat{K}_{in}$
$\hat{K}_o$
ϕ
z
$\hat{K}_{in}$
β
$\hat{S}$

$$\sum_{k=1}^{k_{max}} b_k P_k^1(\cos\theta) = \frac{p_y^+\sigma_- - p_y^-\sigma_+}{\sigma_+ - \sigma_-} \sum_{k=0}^{k_{max}} a_k P_k(\cos\theta).$$

In this notation σ_+ denotes the differential cross section with the beam in the + state, and σ_- denotes the differential cross section with the beam in the - state. After comparing to equation (5-6), inserting $p_y^+ = p_y = -p_y^-$ and noting that $\frac{N_+}{N_-} = \frac{\sigma_+}{\sigma_-}$, we now have the result:

5-13 $$\sum_{k=1}^{k_{max}} b_k P_k^1(\cos\theta) = \frac{\frac{3}{2}A_y(\theta)\sigma(\theta)}{A_0}$$

$$A_y(\theta) = \frac{2}{3p_y}\frac{N_+ - N_-}{N_+ + N_+}.$$

The TUNL polarized ion source produces a polarization of $p_y = -2Q/3$ for a vector polarized deuteron beam, where Q is the percent polarization of the beam. The result for spin 1/2 particles is:

5-14 $$\sum_{k=1}^{k_{max}} b_k P_k^1(\cos\theta) = \frac{A_y(\theta)\sigma(\theta)}{A_0},$$

where $A_y(\theta)$ is the form found in equation (5-4).

The $^{12}C(\vec{n},\gamma_0)^{13}C$ data were fit to equation (5-14) and the $^{11}B(\vec{d},\gamma_0)^{13}C$ data to (5-13) via a weighted least squares method. The fits are shown in Figure 5-4 and Figure 5-5, and the resulting b_k coefficients are shown in Table 5-2. As with the cross section angular distributions it was found to be sufficient to fit to $k_{max} = 2$. All of the analyzing power angular distributions have three or more points, which is sufficient to result in a value for chi-square since there is no associated Legendre polynomial with k=0. The average chi-square per point was less than 1.0 for all fits. Also, the odd polynomials were again small and b_2 was not significantly affected when refitting with b_1

Figure 5-4

Angular distribution of the product of analyzing power and cross section for the $^{12}C(\vec{n},\gamma_0)^{13}C$ reaction at various incident neutron energies. The curves are associated Legendre polynomial fits through k=2 as shown in equation (5-14). The error bars shown represent the statistical uncertainties associated with the data points.

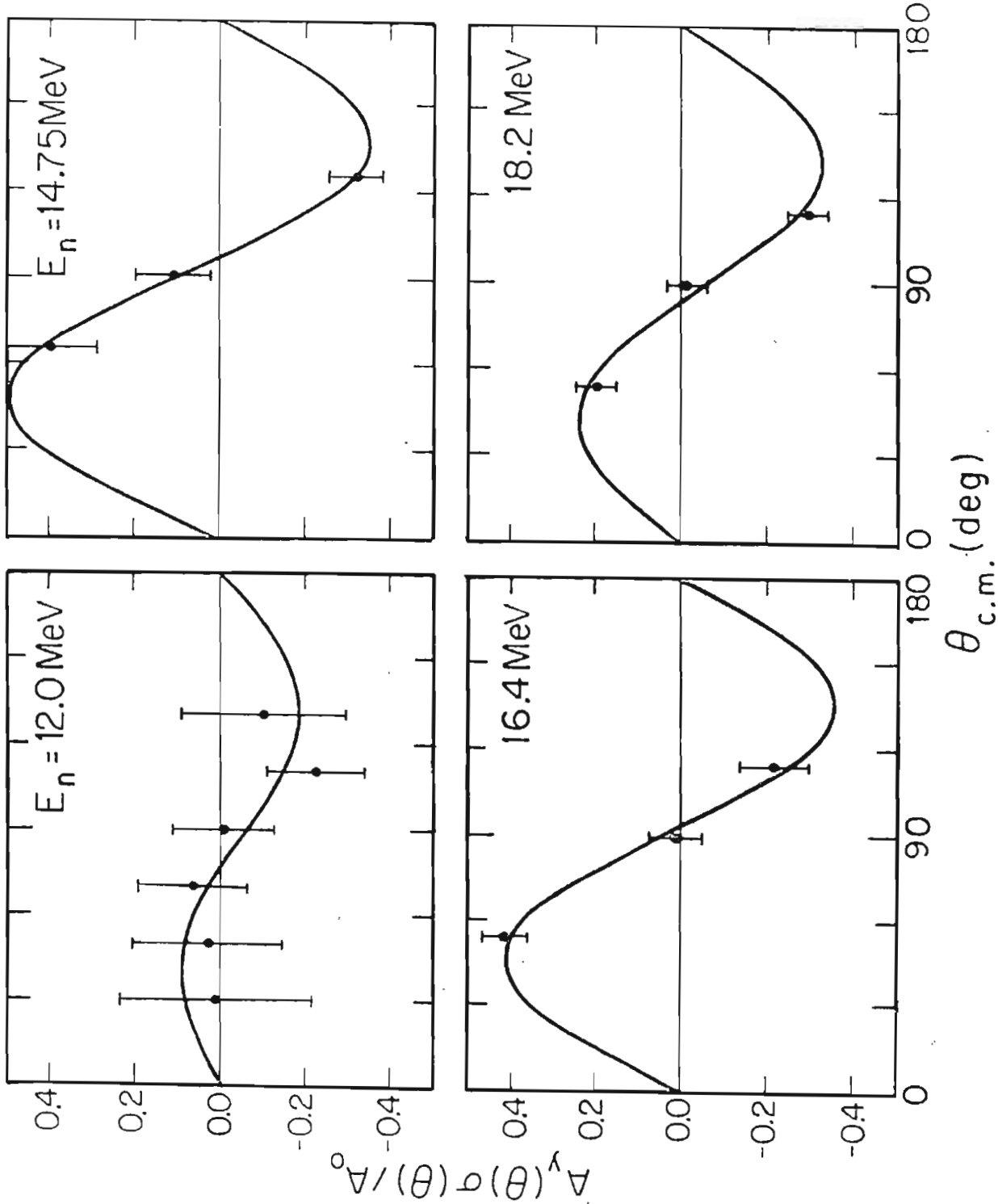
E_n=14.75MeV
E_n=12.0MeV
18.2 MeV
16.4 MeV
$A_y(\theta)\sigma(\theta)/A_o$
$\theta_{c.m.}$ (deg)
0.4
0.2
0.0
-0.2
-0.4
0
90
180

Figure 5-5

Angular distribution of the product of analyzing power and cross section for the $^{11}B(\vec{d},\gamma_0)^{13}C$ reaction at incident deuteron beam energies of 2.0 and 4.0 MeV. The curves are associated Legendre polynomial fits through k=2 as shown in equation (5-13). The error bars shown represent the statistical uncertainties associated with the data points.

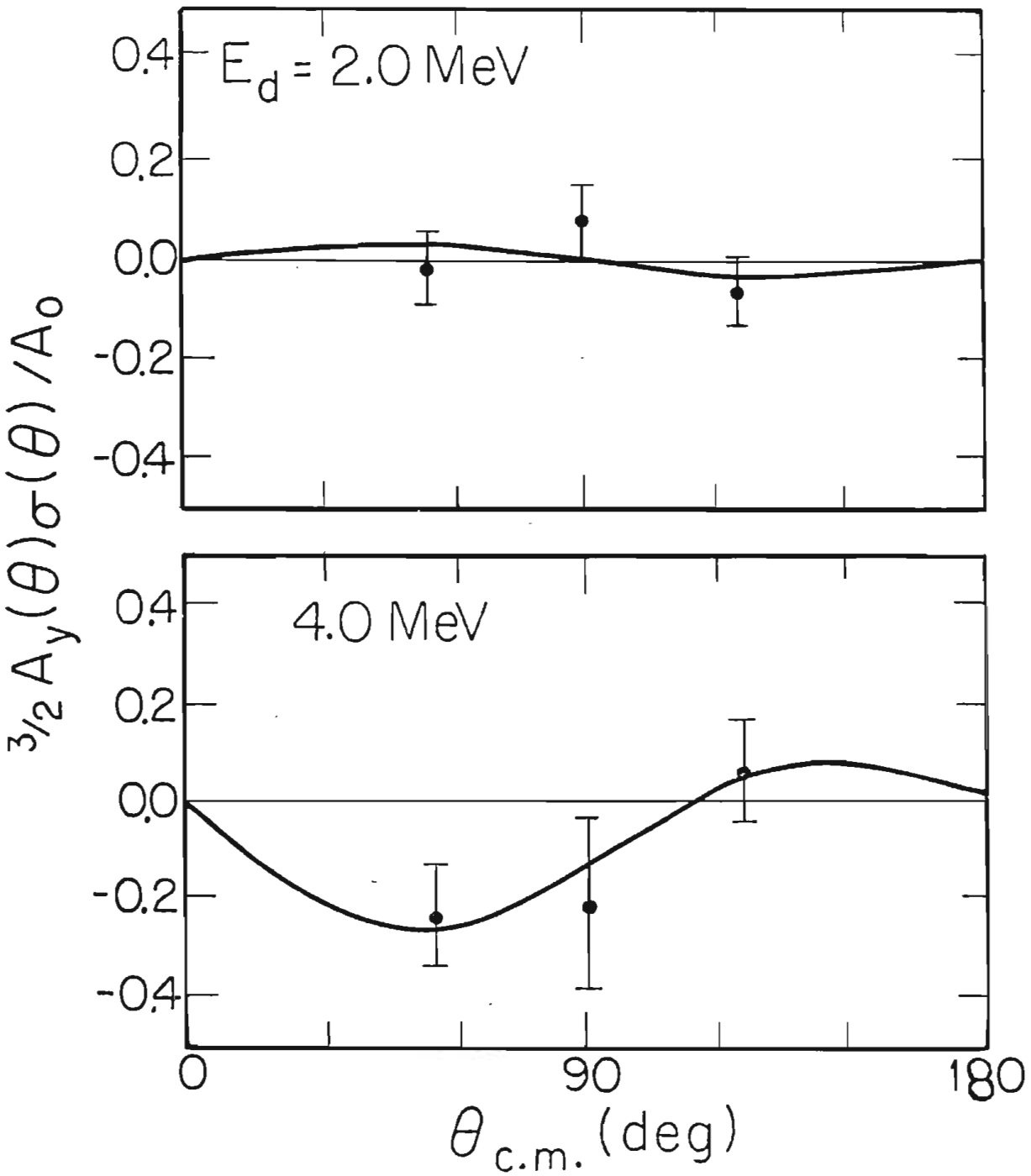
E_d = 2.0 MeV
4.0 MeV
0.4
0.2
0.0
-0.2
-0.4
0
90
180
$\theta_{c.m.}$ (deg)
$^3/_2 A_y(\theta)\sigma(\theta)/A_0$

Table 5-2. b_k coefficients.

$^{12}C(\vec{n},\gamma_0)^{13}C$

E_n(MeV)	E_x(MeV)	b_1	b_2	b_2*
12.0	16.02	0.05 ± 0.05	0.08 ± 0.05	0.08 ± 0.05
14.75	18.56	0.11 ± 0.06	0.28 ± 0.05	0.20 ± 0.05
15.4	19.16	———	———	0.32 ± 0.05
16.4	20.08	-0.04 ± 0.04	0.26 ± 0.04	0.27 ± 0.05
17.4	21.01	———	———	0.17 ± 0.05
18.2	21.74	0.06 ± 0.03	0.19 ± 0.03	0.15 ± 0.05
18.8	22.30	———	———	0.15 ± 0.05

* Fit with $b_1 = 0.0$

$^{11}B(\vec{d},\gamma_0)^{13}C$

E_d(MeV)	E_x(MeV)	b_1	b_2	b_2*
1.6	20.00	———	———	0.07 ± 0.09
1.8	20.17	———	———	-0.07 ± 0.05
2.0	20.35	0.00 ± 0.05	0.02 ± 0.04	0.02 ± 0.04
4.0	22.06	-0.13 ± 0.08	-0.11 ± 0.05	-0.11 ± 0.05

* Fit with $b_1 = 0.0$

Note: All non-exact fits have a chi-square per point of less than 1.0.

= 0. This fact was used in that a number of b_2 coefficients were then obtained from 125° analyzing power measurements alone. To be consistent, the b_2 values obtained from 125° data only were used in the doorway analysis which will be discussed later.

In the case of deuteron beams it is also possible to obtain tensor analyzing powers. To obtain the c_k coefficients of equation (5-7), we now run the source in a mode where $P_z \neq 0$, $P_{zz} \neq 0$, ϕ is undetermined, and $\beta = 0^\circ$. This gives

5-15 $$p_y = \mathrm{Re}t_{21} = \mathrm{Re}t_{22} = 0 \text{ and}$$
$$t_{20} = P_{zz}/\sqrt{2}.$$

Now we call t_1 the moment of state "1" and t_2 the moment of state "2", and write

5-16 $$\sigma_1 - \sigma_2 = A_0(t_1 - t_2)\sum_{k=0}^{k_{max}} c_k P_k(\cos\theta)$$

$$\frac{\sigma_1}{t_1} - \frac{\sigma_2}{t_2} = \left(\frac{1}{t_1} - \frac{1}{t_2}\right)A_0\sum_{k=0}^{k_{max}} a_k P_k(\cos\theta)$$

$$A_0\sum_{k=0}^{k_{max}} a_k P_k(\cos\theta) = \left(\frac{\sigma_1}{t_1} - \frac{\sigma_2}{t_2}\right)/\left(\frac{1}{t_1} - \frac{1}{t_2}\right)$$

$$= \frac{\sigma_1 t_2 - \sigma_2 t_1}{t_2 - t_1}$$

$$\sum_{k=0}^{k_{max}} c_k P_k(\cos\theta) = \frac{\sigma_1 - \sigma_2}{\sigma_2 t_1 - \sigma_1 t_2}\sum_{k=0}^{k_{max}} a_k P_k(\cos\theta)$$

The states produced by the TUNL polarized ion source, as discussed in chapter 3, make it convenient to write $t_1(P_{zz} = -2) = t_{20} = -2t_2(P_{zz} =$

1). Using this and comparing the above result to equation (5-6) yields the result:

$$5\text{-}17 \qquad \sum_{k=0}^{k_{max}} c_k P_k(\cos\theta) = \frac{T_{20}(\theta)\sigma(\theta)}{A_0}$$

$$T_{20}(\theta) = \frac{1}{t_{20}} \frac{\sigma_1 - \sigma_2}{\sigma_2 + \frac{1}{2}\sigma_1}.$$

Note: $t_{20} = -\sqrt{2}Q$, where Q is the percent polarization of the beam.

Tensor polarized distributions were taken at 2.0 and 4.0 MeV incident deuteron beam energies for the $^{11}B(\overleftrightarrow{d},\gamma_0)^{13}C$ reaction. The notation $\overleftrightarrow{d}$ means a tensor polarized deuteron beam was used. The distributions were then fit to equation (5-17) using a weighted least squares method with $k_{max} = 2$ as with the a_k and b_k coefficients. The resulting c_k coefficients are:

$$5\text{-}18 \qquad \begin{array}{lll} & c_0 = 0.06 \pm 0.03 & c_0 = -0.11 \pm 0.04 \\ 2.0\text{ MeV:} & c_1 = 0.07 \pm 0.05 & 4.0\text{ MeV:} \quad c_1 = -0.13 \pm 0.09 \\ & c_2 = -0.25 \pm 0.10 & c_2 = 0.44 \pm 0.16. \end{array}$$

These fits are shown in Figure 5-6. We find the odd term c_1 to be small; refitting with $c_1 = 0$ yields no significant change:

$$5\text{-}19 \qquad \begin{array}{lll} 2.0\text{ MeV:} & c_0 = 0.05 \pm 0.03 & 4.0\text{ MeV:} \quad c_0 = -0.13 \pm 0.04 \\ & c_2 = -0.25 \pm 0.10 & c_2 = 0.33 \pm 0.14. \end{array}$$

When fitting to c_0, c_1, and c_2 the three point angular distribution at 2.0 MeV incident deuteron beam energy results in an exact fit, and so has no value for chi-square. The remaining fits are not exact and yield

Figure 5-6

Angular distribution of the product of tensor analyzing power and cross section for the $^{11}B(\vec{d},\gamma_0)^{13}C$ reaction at the incident deuteron beam energies of 2.0 and 4.0 MeV. The curves are Legendre polynomial fits as in equation (5-17), through k=2. The error bars shown represent the statistical uncertainties associated with the data points.

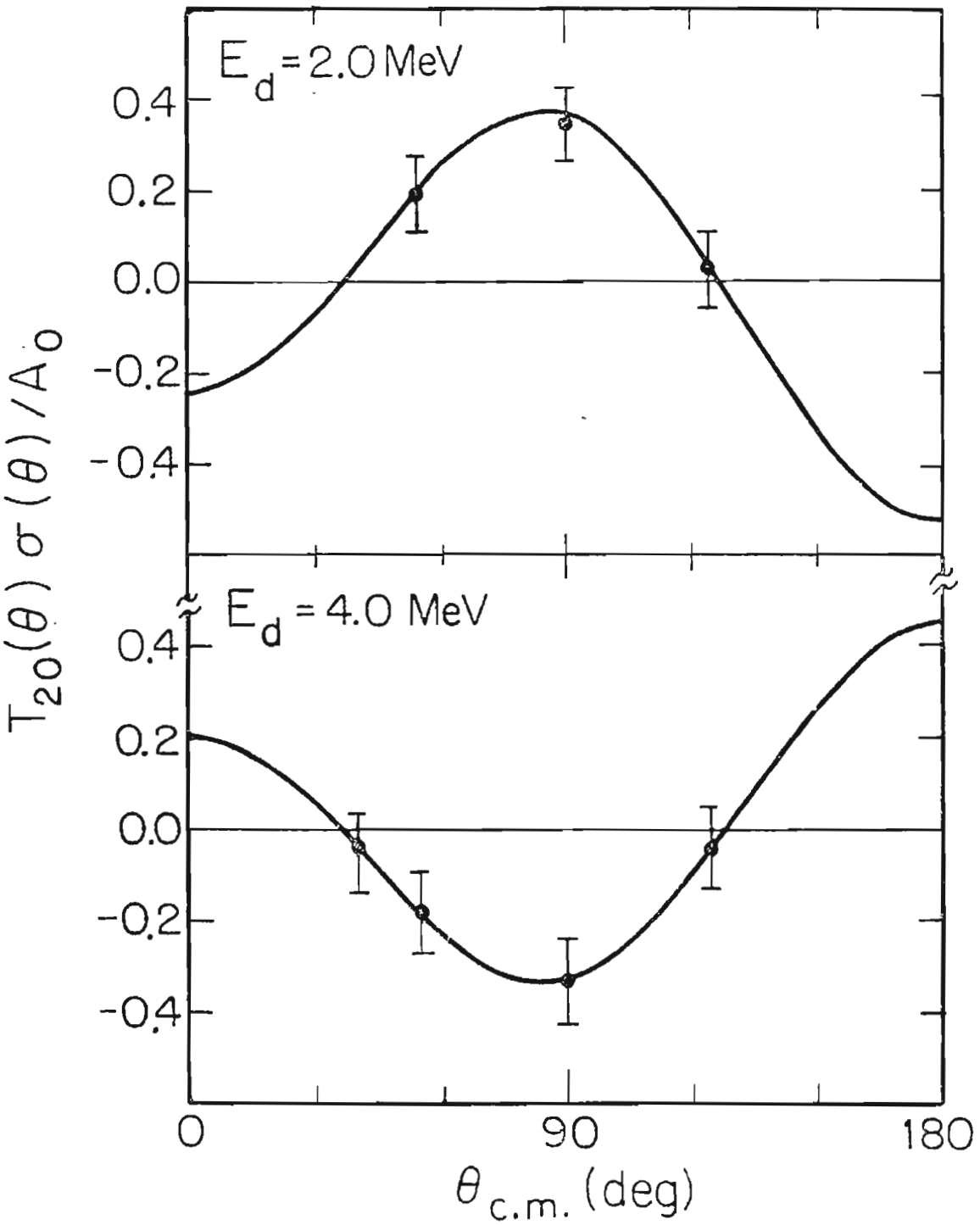
E_d = 2.0 MeV
E_d = 4.0 MeV
$T_{20}(\theta)\,\sigma(\theta)/A_0$
0.4
0.2
0.0
-0.2
-0.4
0
90
180
$\theta_{c.m.}$ (deg)

a value for chi-square per point that was always less than 1.0, indicating a good fit to the data. The $c_1 = 0$ fits were chosen as the ones to be used in the doorway analysis which will be described later.

6 TRANSITION MATRIX ANALYSIS

6.1 Introduction

The angular distributions of cross section and analyzing power can provide further information on the reaction if we rewrite the Legendre polynomial coefficients in terms of transition matrix elements as described by Seyler and Weller (Seyler, 1979). In the case of the $^{12}C(\vec{n},\gamma_0)^{13}C$ reaction, this provides us with a model-independent determination of the amplitudes and phases for E1 gamma rays. As mentioned earlier, the data are consistent with a pure E1 analysis. In the case of the $^{11}B(\vec{d},\gamma_0)^{13}C$ reaction, however, a model-independent analysis is not possible because of the large number of amplitudes and phases. In this case there are 8 amplitudes and 7 relative phases even for a pure E1 analysis.

6.2 Reaction Formalism

The channel spin angular momentum coupling scheme was chosen for use in this work. For the reaction a(x,L)c, we have

$$\vec{x} + \vec{a} = \vec{s} \qquad 6\text{-}1$$
$$\vec{l} + \vec{s} = \vec{b}$$
$$\vec{L} + \vec{c} = \vec{b},$$

where the notation is

6-2 $\vec{a}$ - Total intrinsic angular momentum of the target

$\vec{x}$ - Total intrinsic angular momentum of the incident particle

$\vec{c}$ - Total intrinsic angular momentum of the residual nucleus

$\vec{\ell}$ - Orbital angular momentum of the incident particle

$\vec{s}$ - Channel spin of the reaction

$\vec{L}$ - Multipolarity of the gamma ray

$\vec{b}$ - Total angular momentum of the system.

The reduced transition matrix element is written as

6-3 $$T = \langle pL(c)J\pi \,||R||\, \ell(xa)sJ\pi \rangle,$$

where p is the mode (1 = electric, 0 = magnetic) of the gamma ray transition, and π is the total parity of the system. This complex T-matrix can be written as a real amplitude and a phase. In this work, the E1 amplitudes and phases for a given reaction are expressed as $^{2s+1}\ell_J$ and (ϕ_s, ℓ, J), respectively. A schematic representation of the possible E1 transitions and of their amplitudes for both the $^{12}C(\vec{n},\gamma_0)^{13}C$ reaction ($\vec{a}$=0, $\vec{x}$=1/2, $\vec{c}$=1/2) and the $^{11}B(\vec{d},\gamma_0)^{13}C$ reaction ($\vec{a}$=3/2, $\vec{x}$=1, $\vec{c}$=1/2) is shown in Figure 6-1.

6.3 Model-Independent Analysis for $^{12}C(\vec{n},\gamma_0)^{13}C$

For the $^{12}C(\vec{n},\gamma_0)^{13}C$ reaction there are two amplitudes and one relative phase if we consider only E1 transitions. The Legendre coefficients can be written in terms of these as

Figure 6-1.

Possible E1 decay schemes and their amplitudes for the $^{12}C(\vec{n},\gamma_0)^{13}C$ and $^{11}B(\overleftrightarrow{d},\gamma_0)^{13}C$ reactions.

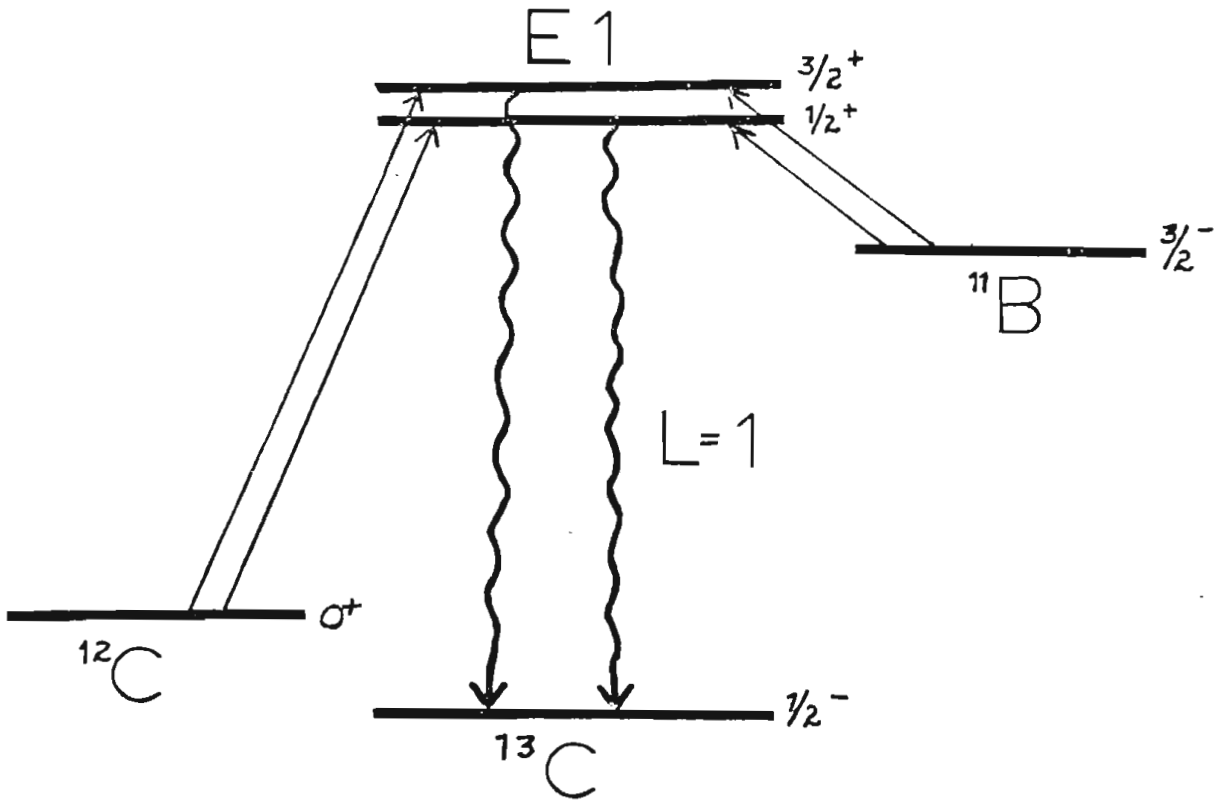

$^{11}B(d,\gamma_0)^{13}C$

ℓ	s	b	amp
1	1/2	1/2	$^2P_{1/2}$
1	1/2	3/2	$^2P_{3/2}$
1	3/2	1/2	$^4P_{1/2}$
1	3/2	3/2	$^4P_{3/2}$
1	5/2	3/2	$^6P_{3/2}$
3	3/2	3/2	$^4F_{3/2}$
3	5/2	1/2	$^6F_{1/2}$
3	5/2	3/2	$^6F_{3/2}$

$^{12}C(n,\gamma_0)^{13}C$

ℓ	s	b	amp
0	1/2	1/2	$^2S_{1/2}$
2	1/2	3/2	$^2D_{3/2}$

6-4
$$A_0 = {}^2S^2_{1/2} + 2{}^2D^2_{3/2}$$
$$A_0 a_2 = -2{}^2S_{1/2}{}^2D_{3/2}\cos(\phi_d-\phi_s) - {}^2D^2_{3/2}$$
$$A_0 b_2 = -{}^2S_{1/2}{}^2D_{3/2}\sin(\phi_d-\phi_s),$$

where the phase is uniquely defined by the index ℓ. If we write $s = {}^2S_{1/2}/\sqrt{A_0}$ and $d = \sqrt{2}{}^2D_{3/2}/\sqrt{A_0}$, we can now rewrite 6-4 as

6-5
$$1 = s^2 + d^2$$
$$a_2 = -\frac{d^2}{2} - \sqrt{2}sd\cos(\phi_d-\phi_s)$$
$$b_2 = -\frac{sd}{\sqrt{2}}\sin(\phi_d-\phi_s).$$

Using this form of the equations we can obtain values for s, d, and $\phi_d-\phi_s$ at six different energies where both a and b coefficients were obtained. Because of the fact that we have three unknowns and three measurements at each energy (A_0, a_2, and b_2), we will obtain exact solutions at each energy. To get an idea of the error on these solutions a chi-square (Bevington, 1969) was formulated for equations 6-5. Each parameter was varied individually until it changed the chi-square from the value of 0.0 obtained with the exact fit to 1.0. This degree of variation was then used as the error on that parameter. The results of this analysis are shown in Figure 6-2 along with the same analysis for the mirror reaction $^{12}C(\vec{p},\gamma_0)^{13}N$. The data of Helmer et. al. (Helmer, 1980) was used in the latter analysis. The solid line shown in Figure 6-2 is an overlay of the results obtained from the secondary doorway state analysis to be discussed in the next chapter.

The quadratic nature of the solutions to equations 6-5 results in

Figure 6-2

Model-independent E1 analysis of the $^{12}C(\vec{n},\gamma_0)^{13}C$ and $^{12}C(\vec{p},\gamma_0)^{13}N$ reactions. The dots represent the dominant d-wave solutions, while the X's represent the dominant s-wave solutions. The solid curve overlying the $^{12}C(\vec{n},\gamma_0)^{13}C$ solutions results from the secondary doorway state analysis discussed in Chapter 7.

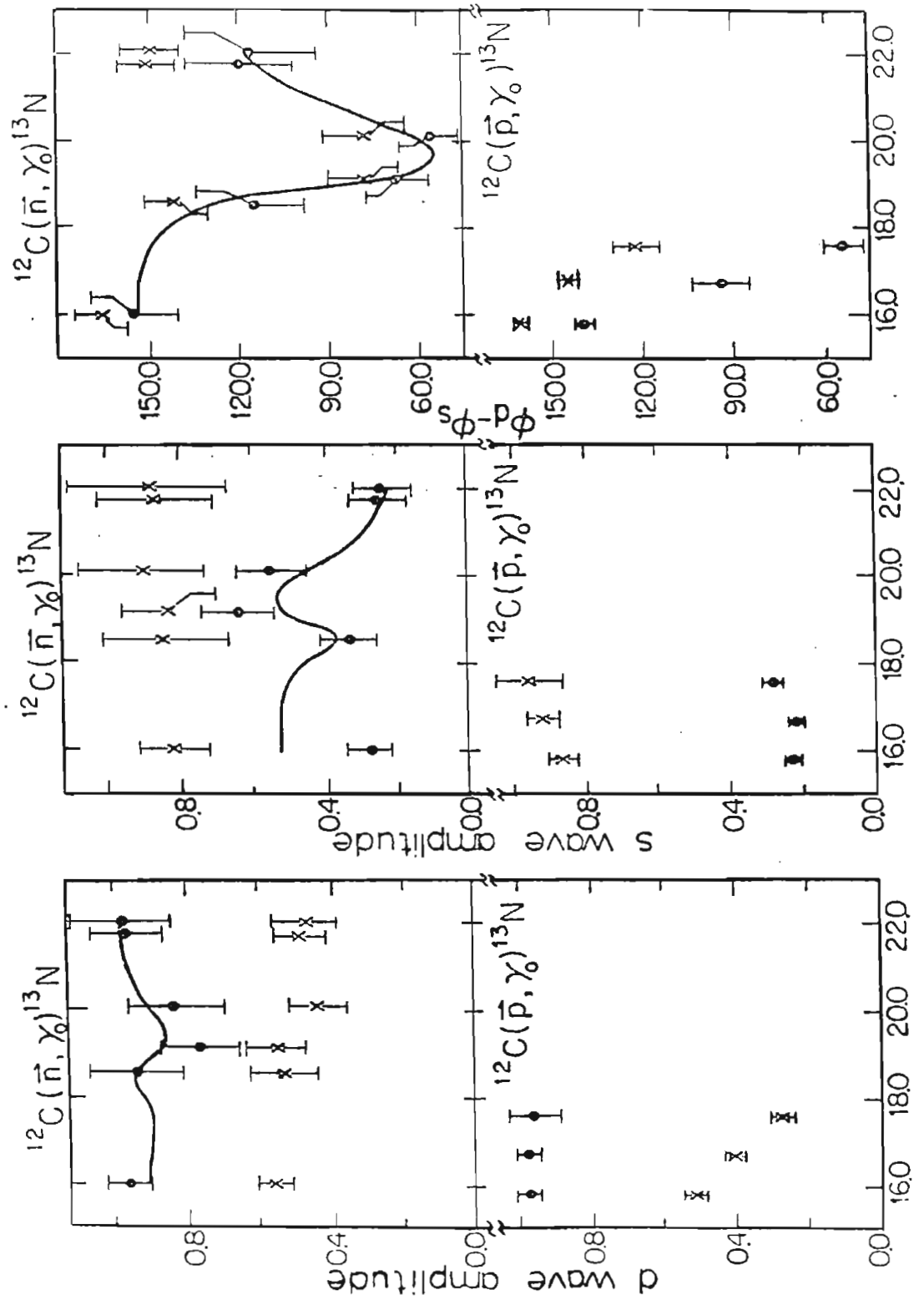
$^{12}C(\vec{n},\gamma_0)^{13}N$
$^{12}C(\vec{p},\gamma_0)^{13}N$
d wave amplitude
s wave amplitude
$\phi_s - \phi_p$
E_x (MeV) in final nucleus

two solutions. The overlay of the results obtained from the secondary doorway state analysis chooses the dominate d-wave solution as the correct one. The dominate d-wave solution obtained in model-independent E1 analyses of nucleon capture reactions has, in previous works, been chosen to be correct on the basis of DSD calculations in cases where such calculations can successfully describe the data (Weller, 1980). In light of this fact, it is not surprising that the secondary doorway state analysis chooses the dominate d-wave solution as the correct one. It should be remembered, however, that the secondary doorway state analysis, unlike the DSD, does not depend upon any specific nuclear model to describe the nuclear states involved in the reaction. Therefore, the secondary doorway state analysis chooses the dominant d-wave solution as correct independently of any nuclear model, unless of course, the reaction theory itself is considered to be a nuclear model.

It is interesting to compare the results, shown in Figure 6-2, for the mirror reactions $^{12}C(\vec{n},\gamma_0)^{13}C$ and $^{12}C(\vec{p},\gamma_0)^{13}N$. In nuclear reactions between isospin allowed states, such as these, one expects the nuclear force to mediate the reaction. We therefore expect similar results for these two reactions. Looking at the dominant d-wave solutions in Figure 6-2 we can see the similarity between the two reactions in the energy range where the data overlap. This supports our expectations about the strong force dominance of this reaction and leads us to expect the $^{12}C(\vec{p},\gamma_0)^{13}N$ reaction to show an energy dependence similar to that of the $^{12}C(\vec{n},\gamma_0)^{13}C$ reaction if the data were continued into that energy region.

6.4 The Form of the T-matrix for $^{11}B(\vec{d},\gamma_0)^{13}C$

As already mentioned, the $^{11}B(\vec{d},\gamma_0)^{13}C$ reaction has 8 amplitudes and 7 relative phases for a pure E1 analysis. The expansion of the Legendre coefficients in terms of these is shown in Table 6-1. The complexity of these equations is obvious. To describe the data using these 15 unknowns runs the risk of obtaining a result whose physical significance is uncertain. To try to simplify the description of the data a cluster model (Wildermuth, 1966) of the ^{13}C ground state was used in the $^{11}B(\vec{d},\gamma_0)^{13}C$ analysis.

6.5 Cluster Model Application to $^{11}B(\vec{d},\gamma_0)^{13}C$ Analysis

The cluster model applied to the ^{13}C ground state represents this state as a deuteron and a ^{11}B core. This configuration does not describe the complete wave function for the ^{13}C ground state, but only a finite portion of the wave function which can have this configuration. This stems from the fact that the wave functions for neutrons and protons in the ^{13}C ground state have a finite probability of having quantum numbers which are the same as that of a deuteron. It is this "deuteron-like" part of the wave function that we are representing with this model. To construct this state we refer back to the simple shell model for protons and neutrons. To represent a physically realizable state the deuteron must correspond to the simple shell model states of the proton and neutron which comprise it. In ^{13}C the valence nucleons

Table 6-1. Legendre coefficients expanded in terms of E1 T-matrix elements in the channel spin representation for the $^{11}B(\vec{d},\gamma_0)^{13}C$ reaction.

The following notation is used in this table: $T_1T_2 \equiv T_1T_2\cos(\phi_2-\phi_1)$, except for the b_2 coefficients where cosine is replaced by sine.

$$A_0 = 0.167\,{}^2P^2_{1/2} + 0.167\,{}^4P^2_{1/2} + 0.167\,{}^6F^2_{1/2} + 0.333\,{}^2P^2_{3/2} + 0.333\,{}^4P^2_{3/2} + 0.333\,{}^4F^2_{3/2} + 0.333\,{}^6P^2_{3/2} + 0.333\,{}^6F^2_{3/2}$$

$$A_0a_2 = -0.333\,{}^2P_{1/2}\,{}^2P_{3/2} + 0.105\,{}^4P_{1/2}\,{}^4P_{3/2} - 0.316\,{}^4P_{1/2}\,{}^4F_{3/2} + 0.258\,{}^6F_{1/2}\,{}^6P_{3/2} - 0.211\,{}^6F_{1/2}\,{}^6F_{3/2} - 0.167\,{}^2P^2_{3/2} + 0.133\,{}^4P^2_{3/2} + 0.200\,{}^4P_{3/2}\,{}^4F_{3/2} - 0.133\,{}^4F^2_{3/2} - 0.033\,{}^6P^2_{3/2} + 0.327\,{}^6P_{3/2}\,{}^6F_{3/2} + 0.033\,{}^6F^2_{3/2}$$

$$A_0b_2 = -0.083\,{}^2P_{1/2}\,{}^2P_{3/2} + 0.118\,{}^2P_{1/2}\,{}^4P_{3/2} - 0.059\,{}^2P_{1/2}\,{}^4F_{3/2} - 0.093\,{}^4P_{1/2}\,{}^2P_{3/2} - 0.011\,{}^4P_{1/2}\,{}^4P_{3/2} - 0.074\,{}^4P_{1/2}\,{}^4F_{3/2} - 0.019\,{}^4P_{1/2}\,{}^6P_{3/2} + 0.095\,{}^4P_{1/2}\,{}^6F_{3/2} - 0.047\,{}^6F_{1/2}\,{}^4P_{3/2} + 0.063\,{}^6F_{1/2}\,{}^4F_{3/2} - 0.168\,{}^6F_{1/2}\,{}^6P_{3/2} + 0.032\,{}^6F_{1/2}\,{}^6F_{3/2} + 0.177\,{}^2P_{3/2}\,{}^4P_{3/2} + 0.059\,{}^2P_{3/2}\,{}^4F_{3/2} + 0.067\,{}^4P_{3/2}\,{}^4F_{3/2} - 0.061\,{}^4P_{3/2}\,{}^6P_{3/2} + 0.100\,{}^4F_{3/2}\,{}^6F_{3/2} - 0.061\,{}^6P_{3/2}\,{}^4F_{3/2} + 0.163\,{}^6P_{3/2}\,{}^6F_{3/2}$$

Table 6-1. Continued

$$A_0c_0 = -0.105\,{}^2P_{1/2}\,{}^4P_{1/2} + 0.316\,{}^2P_{1/2}\,{}^6F_{1/2} + 0.094\,{}^4P^2_{1/2} + 0.141\,{}^4P_{1/2}\,{}^6F_{1/2} - 0.094\,{}^6F_{1/2} + 0.067\,{}^2P_{3/2}\,{}^4P_{3/2} - 0.200\,{}^2P_{3/2}\,{}^4F_{3/2} - 0.490\,{}^2P_{3/2}\,{}^6P_{3/2} + 0.400\,{}^2P_{3/2}\,{}^6F_{3/2} - 0.151\,{}^4P^2_{3/2} - 0.226\,{}^4P_{3/2}\,{}^4F_{3/2} + 0.485\,{}^4P_{3/2}\,{}^6P_{3/2} + 0.453\,{}^4P_{3/2}\,{}^6F_{3/2} + 0.151\,{}^4F^2_{3/2} + 0.339\,{}^4F_{3/2}\,{}^6F_{3/2} - 0.069\,{}^6P_{3/2}\,{}^4F_{3/2} - 0.132\,{}^6P^2_{3/2} + 0.139\,{}^6P_{3/2}\,{}^6F_{3/2} - 0.104\,{}^6F_{3/2}$$

$$A_0c_2 = -0.033\,{}^2P_{1/2}\,{}^4P_{3/2} + 0.100\,{}^2P_{1/2}\,{}^4F_{3/2} + 0.245\,{}^2P_{1/2}\,{}^6P_{3/2} - 0.200\,{}^2P_{1/2}\,{}^6F_{3/2} + 0.105\,{}^4P_{1/2}\,{}^2P_{3/2} + 0.060\,{}^4P_{1/2}\,{}^4P_{3/2} - 0.179\,{}^4P_{1/2}\,{}^4F_{3/2} + 0.110\,{}^4P_{1/2}\,{}^6P_{3/2} - 0.089\,{}^4P_{1/2}\,{}^6F_{3/2} - 0.316\,{}^6F_{1/2}\,{}^2P_{3/2} + 0.045\,{}^6F_{1/2}\,{}^4P_{3/2} - 0.134\,{}^6F_{1/2}\,{}^4F_{3/2} - 0.146\,{}^6F_{1/2}\,{}^6P_{3/2} + 0.119\,{}^6F_{1/2}\,{}^6F_{3/2} - 0.033\,{}^2P_{3/2}\,{}^4P_{3/2} + 0.100\,{}^2P_{3/2}\,{}^4F_{3/2} + 0.245\,{}^2P_{3/2}\,{}^6P_{3/2} - 0.200\,{}^2P_{3/2}\,{}^6F_{3/2} - 0.094\,{}^4P^2_{3/2} + 0.173\,{}^4P_{3/2}\,{}^6P_{3/2} + 0.283\,{}^4P_{3/2}\,{}^6F_{3/2} - 0.094\,{}^4F^2_{3/2} + 0.173\,{}^6P_{3/2}\,{}^4F_{3/2} + 0.047\,{}^6P^2_{3/2} - 0.115\,{}^6P_{3/2}\,{}^6F_{3/2} + 0.024\,{}^6F^2_{3/2}$$

are all in 1P states which have one quanta of excitation each; therefore, the deuteron state in the cluster model must have 2 quanta of excitation, making it a 2S or a 1D state. The ground state of ^{13}C has a total angular momentum of 1/2; therefore, a deuteron and a ^{11}B core in a relative 2S state must have a relative spin of 1/2. Similarly, a 1D state can only lead to relative spins of 3/2 or 5/2. If we assume that the relative spins of the deuteron and the ^{11}B core do not change in the transition from the initial to the final state, then it follows that the incoming partial waves of channel spin $\vec{s}$=1/2 can lead only to a 2S oscillator cluster model ground state in ^{13}C, and, similarly, that $\vec{s}$=3/2, 5/2 can lead only to a 1D ground state. We can now drop the channel spin index s by defining ground state spectroscopic factors, S and D, for the 2S and 1D states such that:

6-6 $$S^2 + D^2 = 1.0.$$

This constraint equation allows S and D to act as only one unknown instead of two. The final simplification is to drop the J dependence on the phase of the incoming partial waves, leaving ℓ to define the phases uniquely.

The expansion of the Legendre polynomial coefficients in terms of the cluster model representation of the T-matrix elements is shown in Table 6-2. This form of the T-matrix elements should be considered as a heuristic modeling attempt. The results obtained when using this form of the T-matrix in a secondary doorway state analysis will be discussed in the next chapter. The obvious benefit of this procedure is the

Table 6-2. Legendre coefficients expanded in the cluster model form of the E1 T-matrix elements for the $^{11}B(\vec{d},\gamma_0)^{13}C$ reaction.

This table uses the notation: $\ell 1_{J1}\ell 2_{J2} \equiv \ell 1_{J1}\ell 2_{J2}\cos(\phi_{\ell 2}-\phi_{\ell 1})$, except for the b_2 coefficients where cosine is replaced by sine.

$$A_0 = 0.333(0.500\,S^2+0.500\,D^2)\,P^2_{1/2} + (0.333\,S^2+0.666\,D^2)\,P^2_{3/2} + 0.167D^2F^2_{1/2} + 0.666D^2F^2_{3/2}$$

$$A_0a_2 = -0.228(1.461\,S^2-0.461D^2)\,P_{1/2}P_{3/2} - 0.067(2.493\,S^2-1.493\,D^2)\,P^2_{3/2} - 0.211D^2F_{1/2}F_{3/2} - 0.100D^2F^2_{3/2} + 0.258D^2P_{3/2}F_{1/2} - 0.316D^2P_{1/2}F_{3/2} + 0.527D^2P_{3/2}F_{3/2}$$

$$A_0b_2 = -0.038(1.553\,SD-0.553\,D^2)\,P_{1/2}F_{3/2} - 0.215D^2F_{1/2}P_{3/2} + 0.228(0.259\,SD+0.741\,D^2)\,P_{3/2}F_{3/2}$$

$$A_0c_0 = -0.011(9.545\,SD-8.545\,D^2)\,P^2_{1/2} - 0.094D^2F^2_{1/2} - 0.221(1.914\,SD-0.914\,D^2)\,P^2_{3/2} + 0.457(0.692\,SD+0.308\,D^2)\,P_{1/2}F_{1/2} + 0.497(0.402\,SD+0.598\,D^2)\,P_{3/2}F_{3/2} + 0.386D^2F^2_{3/2}$$

$$A_0c_2 = 0.487(0.651\,SD+0.349\,D^2)\,P_{1/2}P_{3/2} - 0.015D^2F_{1/2}F_{3/2} - 0.368(0.272\,SD+0.728\,D^2)\,P_{1/2}F_{3/2} + 0.338(0.627\,SD+0.373\,D^2)\,P^2_{3/2} - 0.417(0.758\,SD+0.242\,D^2)\,F_{1/2}P_{3/2} - 0.070D^2F^2_{3/2} + 0.241(-0.415\,SD+1.415\,D^2)\,P_{3/2}F_{3/2}$$

reduction of 15 unknowns to 6: 4 amplitudes, 1 relative phase, and 2 spectroscopic factors (counted as only 1 unknown because of their relation through the constraint equation 6-6).

7 SECONDARY DOORWAY STATE ANALYSIS

7.1 Introduction

As explained in Chapters 1 and 2, direct capture or a DSD model can not account for the features of our data. In order to attempt to give an explanation of our data a secondary doorway state form of the reaction mechanism was used. A simplified illustration of the way in which the $^{11}B(d,\gamma_0)^{13}C$ and $^{12}C(n,\gamma_0)^{13}C$ reactions can proceed by this reaction mechanism is shown in Figure 7-1. The observables were generated by expanding in terms of the T-matrix elements described in Chapter 6, in the form of equations 6-4 for the $^{12}C(\vec{n},\gamma_0)^{13}C$ case, and as in Table 6-2 for the $^{11}B(\overleftrightarrow{d},\gamma_0)^{13}C$ case. The secondary doorway equation (2-33) was used as the form of the T-matrix. This equation is reproduced here as equation 7-1.

$$7\text{-}1 \qquad T^{\alpha}_{\ell j} = \frac{g_1^{\gamma} g_1^{\alpha\ell j} \exp(i\theta_1^{\alpha\ell})\,(E-E_{2r}+\frac{i}{2}\Gamma_2) \;+\; g_1^{\gamma} g_2^{\alpha\ell j} \exp(i\theta_2^{\alpha\ell})\,|V|}{(E-E_{1r}+\frac{i}{2}\Gamma_1)\,(E-E_{2r}+\frac{i}{2}\Gamma_2) \;-\; |V|^2}.$$

It should be noted here that this form of the T-matrix must be multiplied by a factor of $\lambda\!\!\!^{-}/2$, since this factor is implicitly in the T-matrix in terms of which the cross section was expanded in Chapter 6. $\lambda\!\!\!^{-}$ here is the reduced wavelength of the incident beam (Weller, 1980).

7.2 Energy Dependence of the T-matrix

In order to describe the data over the energy range studied, it is necessary to construct an energy independent set of parameters for

Figure 7-1.

A simplified illustration of the way in which the $^{11}B(d,\gamma_0)^{13}C$ and $^{12}C(n,\gamma_0)^{13}C$ reactions can proceed by the secondary doorway state reaction mechanism.

Primary and Secondary Doorway States in ^{13}C

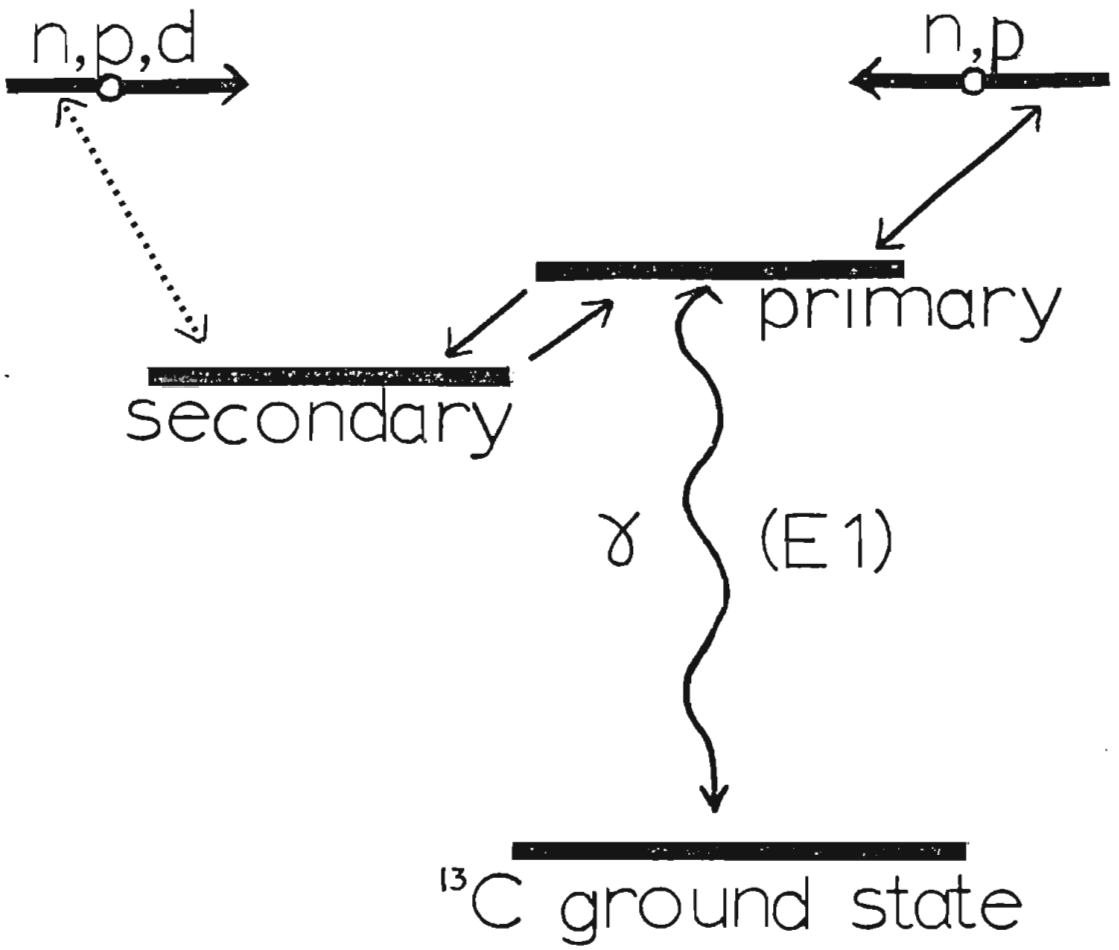

.....This channel would not exist in a "pure" secondary doorway state.

equation 7-1. To do this one must explicitly account for the energy dependence of the partial escape widths Γ_d^α, where α is the escape channel (neutrons, deuterons, or gamma rays) and d is the state (1=primary doorway, 2=secondary doorway). The g's in equation 7-1 are the square roots of these partial escape widths.

For the particle escape channels one must account for the Coulomb penetrabilities and the potential scattering phase shifts. To do this one replaces the simple $g_d^{\alpha\ell j}$ in equation 7-1 by

$$7\text{-}2 \qquad (2P_{\alpha\ell}(E))^{1/2}\exp(i\Omega_{\alpha\ell})g_d^{\alpha\ell j},$$

where:

$$7\text{-}3 \qquad P_{\alpha\ell}(E) = \frac{ak_\alpha}{F_{\alpha\ell}^2(k_\alpha)+G_{\alpha\ell}^2(k_\alpha)},$$

and

$$7\text{-}4 \qquad \Omega_{\alpha\ell} = \sum_{m=1}^{m=\ell}(\tan^{-1}\frac{\eta_\alpha}{m}) - \tan^{-1}(F_{\alpha\ell}(k_\alpha)/G_{\alpha\ell}(k_\alpha))$$

$$\eta_\alpha = 0.1574\ Z_\alpha Z_x (M_\alpha/E)^{1/2}$$

In these expressions, Z_α and Z_x are the charge of the incident and target particles, respectively; M_α is the reduced mass of the system, and E is the lab energy of the incident particle. $P_{\alpha\ell}(E)$ is the Coulomb penetrability, k_α is the wave number of the incoming particle in the center of mass frame. The letter a stands for the radius of the target, while $F_{\alpha\ell}(k_\alpha)$ and $G_{\alpha\ell}(k_\alpha)$ are the regular and irregular solutions of the Coulomb equation (Gove, 1959; Vogt, 1959). These quantities are calculated by the computer program COULM, which is based on a work by B.

Buck and collaborators (Buck, 1960). The $g_d^{\alpha j}$ that we now have in equation 7-2 is energy independent. It should be noted that it was especially important to include this effect in the $^{11}B(d,\gamma_0)^{13}C$ case where the proximity of the resonance to the Coulomb barrier for the incoming deuterons seriously affected the observed width of the resonance.

The energy dependence of the gamma ray partial escape width is proportional to E^{2L+1}, where L is the multipolarity of the gamma ray transition and E is the excitation energy given up by the gamma ray decaying state (Enge, 1966). One then removes the energy dependence from the g_d^{γ} of equation 7-1 by multiplying it by a factor of $(E^{2L+1}/C)^{1/2}$, where C is a constant chosen such that the correction factor is 1.0 at the peak of the giant dipole resonance. This choice of C lets one directly compare a measured Γ^{γ} at the peak of the giant dipole resonance to the results obtained from the secondary doorway state analysis. The simplifying nature of this choice will be obvious later in this chapter. It should be noted that while this correction is not negligible, it is not critically important to the analysis, and leaving it out would not keep one from obtaining a fit to the data. This is because the energy region over which these resonant states interact is small compared to their excitation energy in ^{13}C.

As an example of the way in which all the factors we have mentioned combine with the T-matrix to form an observable, the total cross section expressions for the $^{12}C(n,\gamma_0)^{13}C$ and $^{11}B(d,\gamma_0)^{13}C$ reactions are shown below. These are the forms which were fit to the cross section data to obtain the parameters of the T-matrices.

7-5 For neutron capture:

$$\sigma_T = 4\pi(\lambda\!\!\!^{-}/2)^2 \sum_{\ell,j} \frac{2j+1}{2}\, 2P_{n\ell}(E)\, \frac{E_\gamma^3}{(20.57)^3}\, |T^n_{\ell j}|^2$$

where:

$$T^n_{\ell j} = \frac{g_1^{\gamma} g_1^{n\ell j} \exp(i\theta_1^{n\ell})\,(E - E_{2r} + \frac{i}{2}\Gamma_2) + g_1^{\gamma} g_2^{n\ell j} \exp(i\theta_2^{n\ell})\,|V|}{(E - E_{1r} + \frac{i}{2}\Gamma_1)(E - E_{2r} + \frac{i}{2}\Gamma_2) - |V|^2}$$

For deuteron capture:

$$\sigma_T = 4\pi(\lambda\!\!\!^{-}/2)^2 \sum_{\ell,j} \frac{2j+1}{12}\, 2P_{d\ell}(E)\, \frac{E_\gamma^3}{(20.57)^3}\, |T^d_{\ell j}|^2$$

where:

$$T^d_{\ell j} = \frac{g_1^{\gamma} g_2^{d\ell j} \exp(i\theta_2^{d\ell})\,|V|}{(E - E_{1r} + \frac{i}{2}\Gamma_1)(E - E_{2r} + \frac{i}{2}\Gamma_2) - |V|^2}$$

The reason for the simplified form of the T-matrix used in the $^{11}B(d,\gamma_0)^{13}C$ case will be discussed in the next section.

7.3 Data Fitting Procedure

The data were fitted in terms of equation 7-1 with the energy dependence corrections as just described. The parameters of equation 7-1 were varied until an optimal fit was obtained. The best fit is said to be the one with the best average chi-square (Bevington, 1969) per point.

The data for the neutron channel were fit with the computer program RES4C, while the deuteron channel data used the computer program RES4. Both programs used the subroutine ROCORD to vary the parameters

and find the minimum chi-square. There are several parameters common to both data sets: the resonant energies and widths (E_1, E_2, Γ_1, Γ_2) and the interaction potential (V). Each program was allowed to vary only the resonant energy and width corresponding to its own data set, while both programs were allowed to vary the interaction potential. The fitting process was then iterated between the two programs until a unique set of these common parameters was found. Many different starting sets for these parameters were tried to ensure that the final solution was unique.

To get an idea of the sensitivity of each parameter, each was varied individually until it changed the average chi-square per point by one. This was then quoted as the error on that parameter. It should be noted that not every parameter affects the entire data set. Because of this, each parameter was varied against only those data to which it was sensitive. The average chi-square per point for each sub-data set was normalized to the same value as that for the entire data set during the error analysis. This ensured that the quoted errors for all the parameters reflected the same degree of sensitivity, and the error on any one parameter could therefore be compared directly with the error on any other parameter.

It was shown in Chapter 5 that the angular distribution coefficients (a_2, b_2, c_2) are independent of the absolute cross section. This is equivalent to saying that they are independent of the denominator of equation 7-1 because it drops out of the expression for these coefficients (i.e., $a_2 = A_2/A_0$). If we now assume that only the

secondary doorway state can deuteron decay (because of its multiparticle components in the valence shell) then the first term in the numerator of equation 7-1 also drops out. This assumption is supported by the fact that if the first term in 7-1 is included during the fitting, the fitting routine must set this term equal to zero in order to obtain an acceptable fit. Also, if the primary doorway state could deuteron decay, a broad resonance would appear in the $^{11}B(d,\gamma_0)^{13}C$ cross section data at the position of the giant dipole resonance, something for which there is absolutely no evidence. We are therefore left with only the second term in the numerator of equation 7-1 to determine the angular distribution coefficients. This has the effect of allowing only the relative strengths of the g's to determine the angular distribution coefficients in the $^{11}B(\overleftrightarrow{d},\gamma_0)^{13}C$ case. This means they are independent of E_2, Γ_2, V, and the absolute magnitude of the g's, as well as all the parameters of the primary doorway state. The beauty of this is that it allows us to test our cluster model assumptions independently of testing the doorway state hypothesis. For this reason the angular distribution coefficients in this case were fit by varying only the relative magnitude of the g's. The cross section data were then fit independently by varying the absolute magnitude of the g's (without varying their relative magnitudes) along with E_2, Γ_2, and V.

It was found that the quality of the fit could be greatly enhanced by subtracting a flat background from the $^{12}C(n,\gamma_0)^{13}C$ data before fitting. A background of 1.94 ± 0.17 μb was subtracted from the A_0 data. This procedure assumes that the background has the same angular

distribution characteristics as the doorway states. This behavior is the same as that predicted by the DSD model where the resonant state has the same angular distribution characteristics as the direct capture background on which it is built (Weller, 1980). This lack of structure in the angular distribution resulting from the giant dipole resonance has been discussed previously (Barrett, 1973).

7.4 Results of the Secondary Doorway State Fitting

The average chi-square per point for the entire data set was approximately four. It should be noted, however, that if a handful of the points that deviated the most from the fit was thrown out, then the average chi-square per point could be reduced to approximately two while leaving the resulting fit essentially unchanged. The true test of the quality of the fit is the degree to which it is able to describe the major features of the data.

The parameters of equation 7-1 resulting from the fitting are shown in Table 7-1. It should be noted that in Table 7-1 the phases that have a value of 0^{o} have been set to that value, and are not a result of the fitting. This was done because only the relative phases are significant. The results of the fitting are shown in Figure 7-2 for the $^{12}C(n,\gamma_0)^{13}C$ data. The success at fitting the cross section and angular distribution data is obvious. The fast energy dependence of the angular distribution data is reproduced strikingly well. It is to be remembered here that direct capture and DSD are unable to explain such

Table 7-1. Secondary doorway state parameters as in equation 7-1.

Note: energies are excitation energies in ^{13}C.

Common Parameters

$E_1 = 20.57 \pm 0.84$ MeV $E_2 = 20.20 \pm 0.07$ MeV

$\Gamma_1 = 5.64 \pm 0.43$ MeV $\Gamma_2 = 0.56 \pm 0.09$ MeV

$|V| = 850 \pm 78$ keV

$^{13}C(\gamma, n_0)^{12}C$

	Primary (i=1)	Secondary (i=2)
$g_1^{\gamma} g_i^{n\ell j}(\ell=0, j=\frac{1}{2})$	5.5 ± 4 keV	6.3 ± 5 keV
$g_1^{\gamma} g_i^{n\ell j}(\ell=2, j=\frac{3}{2})$	11.4 ± 1 keV	14.5 ± 3 keV
$\theta_i^{n\ell}(\ell=0)$	0°.	$112. \pm 40^{\circ}$
$\theta_i^{n\ell}(\ell=2)$	$192. \pm 20^{\circ}$	$197. \pm 12^{\circ}$

$^{13}C(\gamma, d_0)^{11}B$

$g_1^{\gamma} g_2^{d\ell j}(\ell=1, j=\frac{1}{2})$	0.8 ± 7 keV	$\theta_2^{d\ell}(\ell=1)$	0°.
$g_1^{\gamma} g_2^{d\ell j}(\ell=1, j=\frac{3}{2})$	17.4 ± 1 keV	$\theta_2^{d\ell}(\ell=3)$	$155. \pm 18^{\circ}$.
$g_1^{\gamma} g_2^{d\ell j}(\ell=3, j=\frac{1}{2})$	10.6 ± 16 keV		
$g_1^{\gamma} g_2^{d\ell j}(\ell=3, j=\frac{3}{2})$	32.5 ± 5 keV		

Figure 7-2.

The dots are the results of the current study, where the cross sections have been detail balanced to give the $^{13}C(\gamma,n_0)^{12}C$ cross sections. The points labeled with an X are an overlay of $^{13}C(\gamma,n_0)^{12}C$ data from (Woodworth, 1979) which have been multiplied by a factor of 0.7 as discussed in (Woodworth, 1984). The data shown in this figure are: the total cross section, the 90^{o} differential cross section, the cross section angular distribution coefficient a_2, and the vector analyzing power angular distribution coefficient b_2. The solid line is the result of the secondary doorway state analysis of the current data. The dotted line in the total cross section plot is the background that was subtracted off for the analysis.

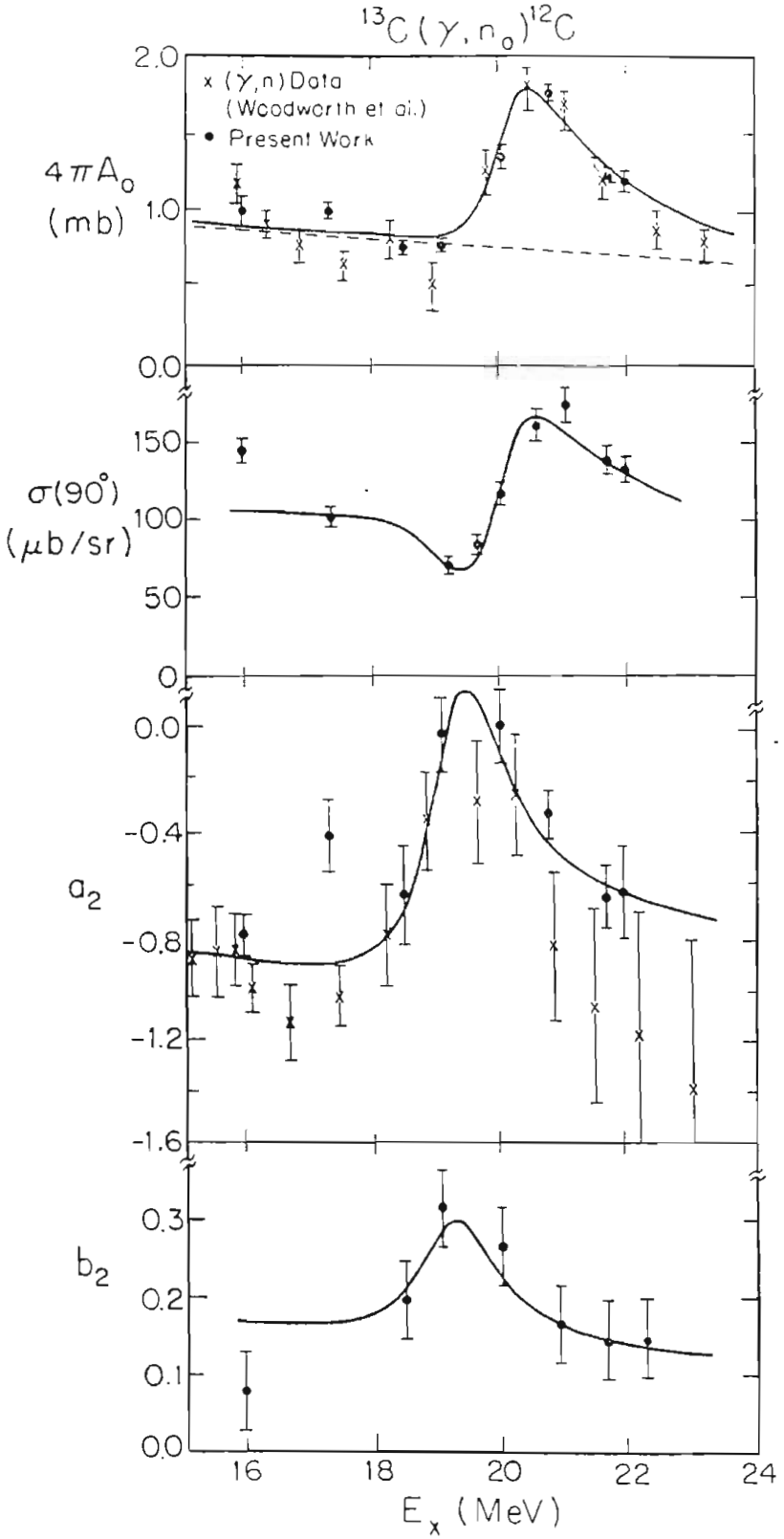
$^{13}C(\gamma, n_0)^{12}C$
x (γ,n) Data
(Woodworth et al.)
• Present Work
$4\pi A_0$
(mb)
2.0
1.0
0.0
$\sigma(90^\circ)$
$(\mu b/sr)$
150
100
50
0
a_2
0.0
-0.4
-0.8
-1.2
-1.6
b_2
0.3
0.2
0.1
0.0
16
18
20
22
24
E_x (MeV)

structure in the angular distribution data.

The fits to the 90° cross section and angular distribution data for the $^{11}B(d,\gamma_0)^{13}C$ reaction are shown in Figure 7-3. It should be noted that the absolute cross sections found in this study agree well with those found in the previously mentioned earlier study (Weller, 1973). An overlay of the data from that study is also shown in Figure 7-3. As mentioned in section 7.3, the angular distribution data in this case are independent of the secondary doorway state analysis. Therefore, the fact that a_2 and b_2 are well described by the fit represents a measure of success for the simple cluster model of this reaction channel. The energy dependence in this case is due almost entirely to the Coulomb penetrabilities, since this resonance is right at the Coulomb barrier for the incident deuterons. It should be noted here that the fit chose the ground state deuteron spectroscopic factor (equation 6-6) to be 98 ± 15 percent $\ell = 2$. The fit of the secondary doorway state to the 90° cross sections is also critically sensitive to the Coulomb barrier. The fitting yields a width for the secondary doorway state of 0.56 ± 0.09 MeV and an energy for this state of 20.20 ± 0.07 MeV. This can be related to what one would expect for an observed width and energy of this state by the following constraint equation (Calarco, 1977; Seyler, 1983):

$$7\text{-}6 \qquad \Gamma_{secd} = \Gamma_2 + \frac{|V|\,\Gamma_1}{(E_2-E_1)^2+\frac{1}{4}\Gamma_1^2}$$

$$E_{secd} = E_2 + \frac{|V|(E_2-E_1)}{(E_2-E_1)^2+\frac{1}{4}\Gamma_1^2}.$$

Figure 7-3

The data shown as dots are the results of the current study. The top figure shows the 90^{o} differential cross section data, with the points labeled with an X being an overlay resulting from the data of a previous study (Weller, 1973). Both data sets have been detail balanced to give $^{13}C(\gamma,d_0)^{11}B$ cross sections. Also shown are the cross section angular distribution coefficients a_2, and the vector analyzing power angular distribution coefficients b_2. The solid line is the result of the secondary doorway state analysis of the current data.

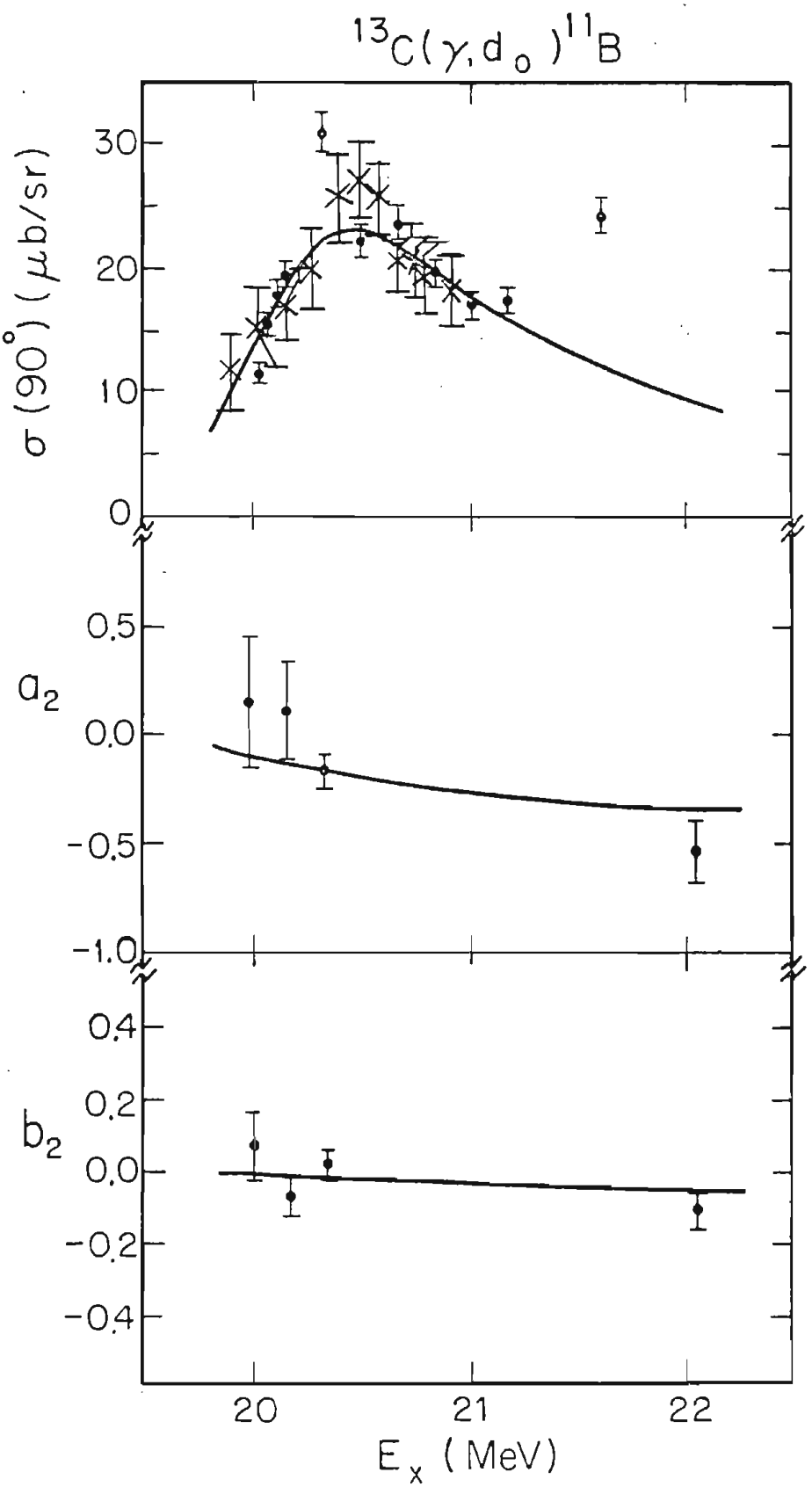
$^{13}C(\gamma, d_0)^{11}B$
$\sigma(90^\circ)$ (μb/sr)
30
20
10
0
a_2
0.5
0.0
-0.5
-1.0
b_2
0.4
0.2
0.0
-0.2
-0.4
20
21
22
E_x (MeV)

Using Table 7-1 we obtain: $\Gamma_{secd} = 1.06$ MeV, $E_{secd} = 20.17$ MeV. These values are what one would expect without the effects of the Coulomb barrier. It is obvious when one compares these values with the actual data that the Coulomb barrier plays an important role in this reaction. It would have been impossible to have determined the correct width and resonance energy without taking this into account.

The total cross section data for the $^{11}B(d,\gamma_0)^{13}C$ reaction is shown in Figure 7-4 along with the secondary doorway state fit. Because of the relatively few number of points compared to the 90^o cross section data, this data did not play an important role in determining the energy and width of the secondary doorway state. The points near the peak of the resonance show good agreement with the fit. The simple shell model is, however, apparently inadequate to explain the cross section data near $E_x = 22$ MeV, even though it worked in the region of the secondary doorway state resonance.

The c_0 and c_2 Legendre polynomial coefficients resulting from the angular distribution of the tensor analyzing power $T_{20}(\theta)$ are shown in Figure 7-5. The line is the prediction resulting from the fit to a_2 and b_2 that was shown in Figure 7-3. Attempts to include c_0 and c_2 in the fitting procedure produced results insignificantly different from those shown; therefore, they were not included in the fitting procedure. The predictions run in the region between the experimentally determined c_2 values and do a poor (but not extremely bad) job of predicting the data. While this shows the limitations of our simple cluster model, it also shows the great value of tensor beams in testing models of

Figure 7-4

The total cross section data of the current study is shown, where it has been detail balanced to give $^{13}C(\gamma,d_0)^{11}B$ cross sections. The solid line is the result of the secondary doorway state analysis.

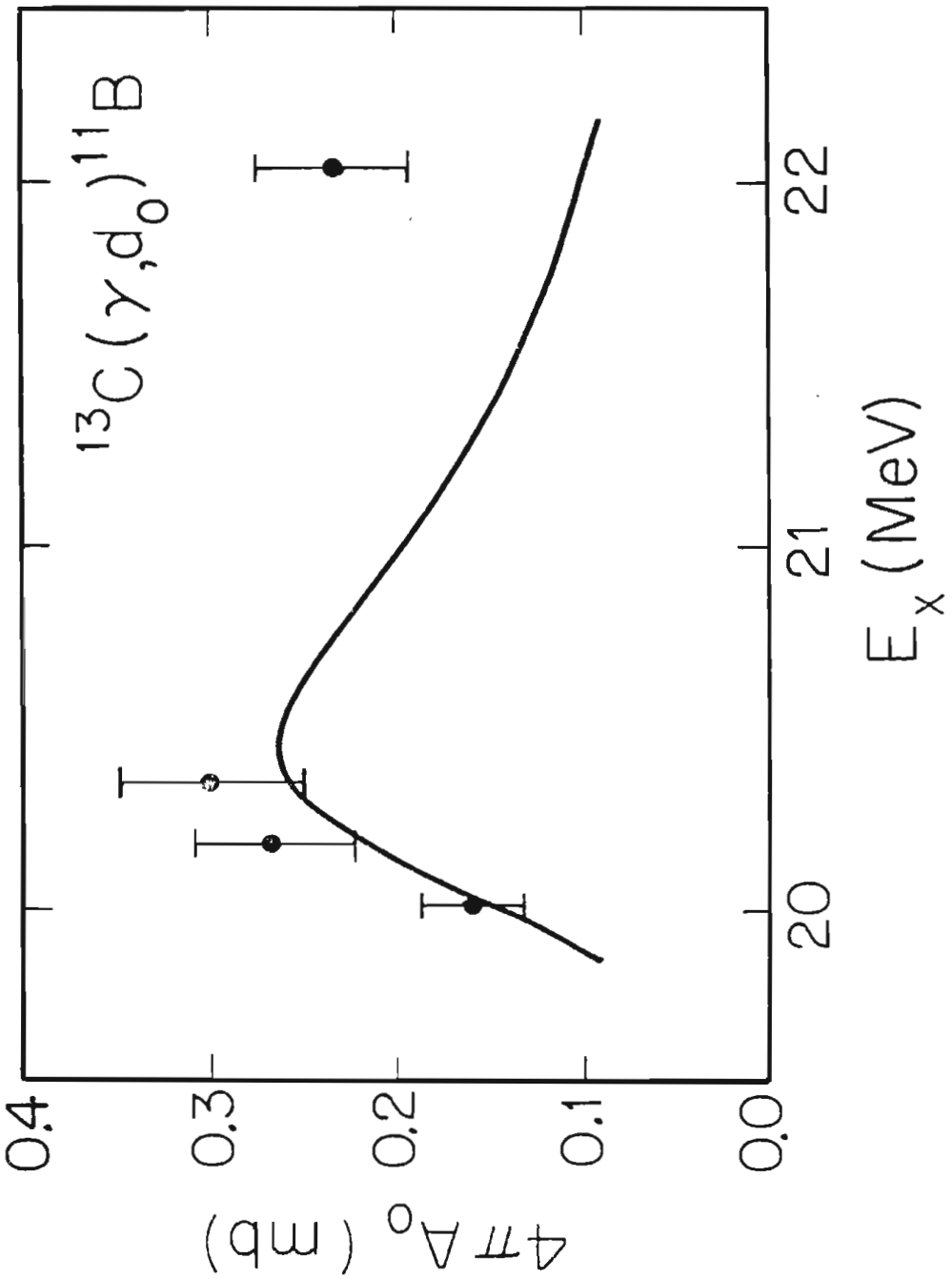
$^{13}C(\gamma,d_0)^{11}B$
$4\pi A_o$ (mb)
0.0
0.1
0.2
0.3
0.4
20
21
22
E_x (MeV)

Figure 7-5

The data are the results of the current study for the tensor analyzing power $T_{20}(\theta)$ angular distribution coefficients c_0 and c_2. The solid line is an overlay of the prediction for these quantities resulting from the secondary doorway state analysis of the current data.

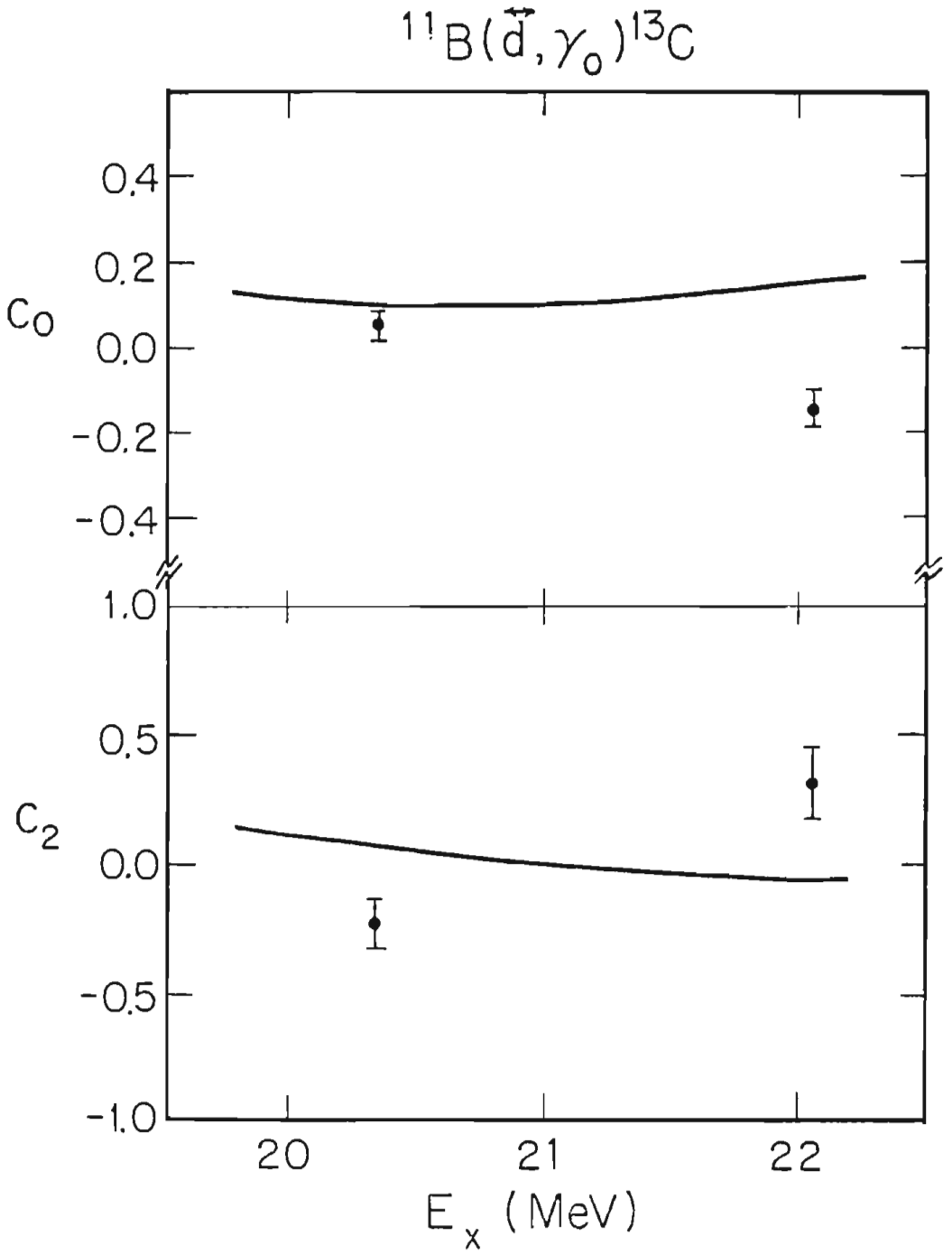
$^{11}B(\vec{d},\gamma_0)^{13}C$
C_0
0.4
0.2
0.0
-0.2
-0.4
1.0
C_2
0.5
0.0
-0.5
-1.0
20
21
22
E_x (MeV)

complicated nuclear configurations. The physics determining c_0 and c_2 is probably different from that determining the a's and b's. Figure 7-5 shows that our simple model is not sufficient to explain these effects. Obtaining a successful fit to these data would require dropping the cluster model and using all of the fifteen unknowns discussed in Chapter 6. However, such a procedure would probably obscure the results, masking the ability of the simple model to describe the a_2 and b_2 data without adding any significant new insight to the problem.

7.5 Interaction Matrix Element

From Table 7-1 we can see that the interaction matrix element derived from the fitting is $|V| = 850 \pm 78$ keV. It is interesting to compare this value to the shell model calculation of this quantity in Chapter 2, where the interaction matrix element was expanded in terms of two body matrix elements. As mentioned in that chapter, the giant dipole resonance in ^{13}C is expected to be dominated by transitions promoting a particle into the $d_{5/2}$ subshell. The results, from Table 2-2, for such matrix elements are:

7-7 $J = 1/2 \rightarrow |V| = 675$ keV

$J = 3/2 \rightarrow |V| = 850$ keV

Statistically weighted average $\rightarrow |V| = 800$ keV.

These values (particularly the J = 3/2, and the average value) are in excellent agreement with the experimentally determined value of 850 ± 78 keV. Inspection of Table 7-1 will reveal that most of the strength

determined by the fitting lies in the J = 3/2 channels. This excellent agreement lends substantial support to our assertion that this interaction is dominated by the strong force interaction between a primary and a secondary doorway state, the natures of which were discussed in Chapter 2.

7.6 Doorway State Strengths

As stated in Chapters 1 and 2, the classical dipole sum rule for ^{13}C is 193.85 mb·MeV, and 64 to 72 percent of this is exhausted by the giant dipole resonance (17 to 34 MeV in ^{13}C). Of this strength 70 to 95 mb·MeV (50 to 77 percent of the giant dipole strength) can be attributed to $^{13}C(\gamma,n_{tot})$ (Cook, 1957). The amount of sum rule contained in our data can be conveniently seen by looking at the fit to the cross section data of Figure 7-2. By summing the area under the $4\pi A_0$ fit in Figure 7-2 from about 19 to 24 MeV, we see that the $^{13}C(\gamma,n_0)^{12}C$ channel in the $T_<$ giant dipole resonance contains approximatly 7 mb·MeV. It should be remembered here that only the $T_<$ part of the giant dipole resonance can be populated by this reaction. Because of the background subtraction we can attribute only about half of this to the doorway states. This means that no more than about 10 percent of the $^{13}C(\gamma,n_{tot})$ strength contained in the giant dipole resonance region of ^{13}C can be attributed to the $^{13}C(\gamma,n_0)^{12}C$ reaction over the $T_<$ part of the giant dipole resonance. This small contribution from the $^{13}C(\gamma,n_0)^{12}C$ reaction is not surprising in light of an earlier study of the $^{13}C(\gamma,n_{tot})$ reaction which found that the average energy of the detected neutrons was small over the

giant resonance region, indicating that most of the neutrons leave ^{13}C in excited states (Jury, 1979).

As discussed in Chapter 2, a secondary doorway state typically has no gamma or particle decay modes. However, in this case the assumed shell model structure of "deuteron-like" configurations in the valence shell would make decay by deuterons plausible, as well as the more simple single-particle neutron and proton decays. Other allowed two-particle decay modes are below threshold at the position of the secondary doorway state and are thus forbidden. Therefore it seems resonable that if one accounts for the neutron, proton, and deuteron partial escape widths, any remaining width contained in the secondary doorway state must be its natural damping width.

From the fitting one extracts parameters that are the particle partial escape widths of the secondary doorway state multiplied by the gamma ray partial escape width of the primary doorway state:

$$7\text{-}8 \qquad \Gamma_1^{\gamma}\Gamma_2^{\alpha} = \sum_{j,\ell} (g_1^{\gamma} g_2^{\alpha\ell j})^2$$

where α = n for neutrons, and α = d for deuterons. From Table 7-1:

$$7\text{-}9 \qquad \Gamma_1^{\gamma}\Gamma_2^{n} = 250\ (\text{keV})^2$$

$$\Gamma_1^{\gamma}\Gamma_2^{d} = 1472\ (\text{keV})^2.$$

In order to extract the secondary doorway state information we must remove g_1^{γ} from these expressions. This quantity has not been measured, but it can be extracted from an estimate of the total absorption cross

section in ^{13}C at the peak of the $T_<$ giant dipole resonance. This estimate, which is taken from past measurements of the $^{13}C(\gamma,n_{tot})$ and $^{13}C(\gamma,p)^{12}B$ reactions, is approximatly 10 mb (Cook, 1957). From this value one can extract a gamma ray partial escape width (Hayward, 1970) for this case of approximatly 6 keV. Therefore we have:

7-10 $\Gamma_2^n = 42$ keV

$\Gamma_2^d = 245$ keV

where, $\Gamma_2 = 560$ keV.

If one makes the resonable assumption that the proton partial escape width would not exceed that of the neutron, then we see that this calculation accounts for no more than about 2/3 of the secondary doorway state width. The remaining width must therefore be accounted for as the damping width of the secondary doorway state. It should be noted that the uncertainties in this calculation are such that one should not claim an exact knowledge of the amount of damping in the secondary doorway state. The calculation does, however, give a good indication of a significant amount of this state's width being due to such damping.

8 CONCLUSIONS

It is valuable at this point to summarize the results of this study, which were brought to light throughout the main body of this thesis. The deuteron capture polarized and unpolarized angular distribution results will be considered first, since the fact that there is only a single decay channel (through the primary doorway state) in this case, and therefore no interference effects, allowed us to analyze this data independently of our testing of the secondary doorway state approach. We saw that the simple cluster model of a "deuteron like" state in ^{13}C provided a framework which allowed us to successfully describe the a_2 and b_2 coefficients, which were derived from the cross section and vector analyzing power angular distributions. The energy dependence was shown to be due to the proximity of the resonance to the Coulomb barrier for the incident deuterons. This model was not able to reproduce the c_0 and c_2 coefficients, which were derived from the angular distributions of the tensor analyzing power $T_{20}(\theta)$. This breakdown demonstrates the limitations of the cluster model and the value of tensor polarized beams in testing models of the complicated nuclear configurations.

The effects of the Coulomb barrier on the incident deuterons was also evident in the $^{11}B(d,\gamma_0)^{13}C$ cross section data. When the Coulomb effects were taken into account in our analysis, the width of the secondary doorway state which was extracted was significantly broader than that which was seen in the data. This extracted width of the

secondary doorway state agrees well with the value which was found for this quantity in a previously published analysis of the secondary doorway state effect, which was done before the $^{11}B(d,\gamma_0)^{13}C$ reaction study was added to the analysis (Woodworth, 1984). We have seen that when these data were analyzed simultaneously with the data we obtained for the neutron capture reaction channel, the results were impressive. The secondary doorway state analysis reproduced the strong energy dependence shown in both the cross section and vector analyzing power angular distributions of the neutron capture data.

As mentioned at the beginning of this thesis, we expect that the strong force interaction should be responsible for the interaction of the primary and secondary doorway states, since these are both T = 1/2 states. We therefore performed calculations of the matrix element for the interaction between these states which were modeled in the framework of the shell model. The very good agreement between the calculated value and the value which resulted from the secondary doorway state analysis of the data can be considered strong evidence that the strong force interaction is indeed responsible for this interaction of the doorway states.

In Chapter 6 a model-independent T-matrix analysis was performed on the $^{12}C(\vec{n},\gamma_0)^{13}C$ data, and resulted in two solutions (a dominant d-wave and a dominant s-wave solution). An overlay of the secondary doorway state analysis of Chapter 7 chose the dominant d-wave solution as the correct one. This is an appealing method for choosing the correct solution because of the nuclear model independence of a doorway

state analysis. An analogous model-independent analysis was performed on data resulting from a study of the mirror reaction $^{12}C(\vec{p},\gamma_0)^{13}N$ (Helmer, 1980). A comparison of the dominant d-wave solutions in the energy region in which the data overlap shows a definite similarity. This can be considered further evidence for the strong force dominance of the reaction.

In the preceding chapter a rough calculation was made of the particle escape partial width of the secondary doorway state. The value resulting from this calculation accounted for no more than 2/3 of the total width of the secondary doorway state. We are therefore led to expect that a significant amount of the total width is due to a damping of the state.

Bringing together all the conclusions of this study, one can say that there is strong evidence that a secondary doorway state effect exists in the ^{13}C system. As mentioned at the beginning of this thesis, a secondary doorway state effect has been previously observed in the ^{16}O system (Calarco, 1977). Unlike the current study, the interaction in that case was between states of different isospin, and the interaction was therefore Coulombic. Because of this, that case could not be used to test the effects of the strong force coupling of the states.

These observations of secondary doorway states using radiative capture reactions should be considered in terms of the general doorway state concept (Feshbach, 1967). Secondary doorways are a natural part of that concept, and the fact that we observe them lends credence to the importance of the doorway state reaction mechanism in nuclear physics.

9 REFERENCES

R.F. Barrett, L.C. Biedenharn, M. Danos, P.P. Delsanto, W. Greiner, and H.G. Wahsweiller

Rev. Mod. Phys. 45 (1973) 44

H.H. Barschall and W. Haeberli, eds.

Polarization Phenomena in Nuclear Reactions, Proc. of the Third Inter. Symp., Madison, WI, 1970

D. Berghofer, M.D. Hasinoff, R. Helmer, S.T. Lim, D.F. Measday, and K. Ebisawa

Nucl. Phys. A263 (1976) 109

I. Bergqvist

Lund Institute of Technology, private communication, 1984

G. Bertsch, J. Borysowicz, H. McManus, and W.G. Love

Nucl. Phys. A284 (1977) 399

Philip R. Bevington

Data Reduction and Error Analysis for the Physical Sciences

McGraw-Hill, New York, 1969

G.E. Brown

Nucl. Phys. 57 (1964) 339

B. Buck, R.N. Maddison, and P.E. Hodgson

Phil. Mag. 5 (1960) 1181

J.R. Calarco, S.W. Wissink, M. Sasao, K. Wienhard, and S.S. Hanna

Phys. Rev. Lett. 39 (1977) 925

T.B. Clegg, G.A. Bissenger, W. Haeberli, and P.A. Owen

"Lamb-Shift Polarized Ion Sources for Tandem Accelerators at Wisconsin and Triangle Universities Nuclear Laboratory"

in Barschall and Haeberli (1970), p. 835

C.F. Clement, A.M. Lane, and J.A. Rook

Nucl. Phys. 66 (1965) 273 and 293

B.C. Cook

Phys. Rev. 106 (1957) 300

S.E. Darden

"Description of Polarization and Suggestions for Additional Conventions"

in Barschall and Haeberli (1970), p. 39

A. deShalet and I. Talmi

Nuclear Shell Theory

Academic, New York, 1963

M. Drosg

Nucl. Sci. and Eng. 67 (1968) 190

P.M. Endt and M. Demeur, eds.

Nuclear Reactions

North-Holland, New York, 1959

Harald Enge

Introduction to Nuclear Physics

Addison-Wesley, Reading, Massachusetts, 1966

H. Feshbach, A.K. Kerman, and R.H. Lemmer

Ann. Phys. 41 (1967) 230

D.I. Garber and R.R. Kinsey

Neutron Cross Sections; Vol. II, Curves

Brookhaven National Laboratory

Upton, New York, 1973, 99 BNL 325

M. Goldhaber and E. Teller

Phys. Rev. 74 (1948) 1046

C.R. Gould, L.G. Holzsweig, S.E. King, Y.C. Lau, R.V. Poore, N.R. Roberson, and S.A. Wender

IEEE Trans. on Nucl. Sci. NS-28 , No. 5 (1981) 3708

H.E. Gove

"Resonance Reactions, Experimental"

in Endt and Demeur (1959), p. 259

Dean Halderson and R.J. Philpott

Nucl. Phys. A321 (1979) 295; and private communication.

E. Hayward

Photonuclear Reactions, U.S. Natl. Bur. Stand. Monograph No. 118 Washington, DC, 1970

R.L. Helmer, M.D. Hasinoff, J.E. Bussoletti, K.A. Snover, and T.A. Trainor

Nucl. Phys. A336 (1980) 219

J. Höhn, H.W. Barz, and I. Rotter

Nucl. Phys. A330 (1979) 109

M.J. Jensen

unpublished Ph.D. Dissertation, North Carolina State University, 1981

J.W. Jury, B.L. Berman, D.D. Faul, P. Meyer, K.G. McNeill, and J.G. Woodworth

Phys. Rev. C 19 (1979) 1684

S.E. King

unpublished Ph.D. Dissertation, Duke University, 1983

P.W. Lisowski

unpublished Ph.D. Dissertation, Duke University, 1973

M. Marangoni, P.L. Ottaviani, and A.M. Saruis

Phys. Lett. 49B (1974) 253

M. Marangoni, P.L. Ottaviani, and A.M. Saruis

Nucl. Phys. A277 (1977) 239

D.F. Measday, A.B. Clegg, and P.S. Fisher

Nucl. Phys. 61 (1965) 269

Eugen Merzbacher

Quantum Mechanics

John Wiley and Sons, New York, 1961

N.R. Roberson and S.E. Edwards

IEEE Trans. on Nucl. Sci. NS-28 , No. 5 (1981) 3834

M.E. Rose

Elementary Theory of Angular Momentum

John Wiley and Sons, New York, 1957

S.M. Seltzer and M.J. Berger

NAS-NRC Publ. 1133 (1964) 187

R.G. Seyler and H.R. Weller

Phys. Rev. C 20 1979 453

R.G. Seyler

Ohio State University, private communication, 1983

E. Storm and I. Israel

Nucl. Data Tab. 7 No. 6 (1970) 565

M. Suffert, W. Feldman, J. Mahieux, and S.S. Hanna

Nucl. Instr. Meth. 63 (1968) 1

S. Tonsfeld

unpublished Ph.D. Dissertation, University of North Carolina, Chapel Hill, 1980

T.A. Trainor, T.B. Clegg, and P.W. Lisowski

Nucl. Phys. A220 (1974) 533

J.D. Turner

unpublished Ph.D. Dissertation, Duke University, 1978

E. Vogt

"Resonance Reactions, Theoretical"

in Endt and Demeur (1959), p. 259

W.L. Wang and C.M. Shakin

Phys. Rev. C 5 (1972) 1898

H.R. Weller and R.A. Blue

Nucl. Phys. A211, (1973) 221

H.R. Weller and N.R. Roberson

Rev. Mod. Phys. 52 4 (1980) 699

S.A. Wender, C.E. Floyd, T.B. Clegg, and W.R. Wylie

Nucl. Inst. Meth. 174 (1980) 341

K. Wildermuth and W. McClure

Cluster Representation of Nuclei

Springer-Verlag, Berlin, 1966

J.G. Woodworth, K.G. McNeill, J.W. Jury, P.D. Georgopulus, and R.G. Johnson

Nucl. Phys. A327 (1979) 53

J.G. Woodworth, R.A. August, N.R. Roberson, D.R. Tilley, H.R. Weller, and J.W. Jury

Phys. Rev. C 29 (1984) 1186

A MATRIX ELEMENT EXPANSION

The coupling we have chosen is:

A-1 $$\langle j_h^{-1} j_2(J_\gamma, T_\gamma) j_1(J,T) \,|V|\, [j_1^2(J_2, T_2) j_2]^{J_p, T_p} j_h^{-2}(J_h, T_h)(J,T) \rangle$$

For any given matrix element we need only two possible angular momenta (j_1 and j_2) to describe all the possible particle states in our particle–hole formalism. This is true for the cases we need to consider, it is not, however, a general feature of the particle–hole formalism. Similarly, the angular momenta j_h is the only possibility for the hole states.

We wish to expand the matrix element A-1 in terms of the two-body forces between the various particles and holes. To do this we use the creation and annihilation operators (a and $a^\dagger$) (Merzbacher, 1961). We use here the following notation:

A-2 $$a_x \equiv a_{j_x, T_x, m_{j_x}, m_{T_x}}$$

$|0\rangle$ is the vacuum-ket, which represents the ^{12}C core.

Therefore, the matrix element can be written as

A-3 $$\langle 0 | a_h^\dagger a_2(J_\gamma, T_\gamma) a_1(J,T) \,|V|\, (J,T)(J_h, T_h) a_h a_h (J_p, T_p) a_2^\dagger (J_a, T_a) a_1^\dagger a_1^\dagger | 0 \rangle .$$

We now introduce the further notation:

A-4 $$\bar{J} = (2J+1)^{1/2}$$

$$\delta^A_B = 1 \quad \text{if } A=B, \quad = 0 \quad \text{if } A \neq B.$$

The Wigner 6-j coefficients are represented by the symbols:

$$\left\langle \begin{matrix} j1 & j2 & j3 \\ j4 & j5 & j6 \end{matrix} \right\rangle$$

The expansion can be written in terms of three two-body matrix elements. We will call these terms 1A, 1B, and 2 for reasons that will become obvious later. The matrix element A-1 will be expanded in terms of these as

A-5 $$\langle \text{ Matrix Element } \rangle = \langle\ 1\ \rangle + \langle\ 2\ \rangle$$

$$\langle\ 1\ \rangle = \langle\ 1A\ \rangle + \langle\ 1B\ \rangle$$

$$= (\text{common terms})(\langle\ 1a\ \rangle + \langle\ 1b\ \rangle)$$

This particular notation was chosen to agree closely with the derivation of a similiar coupling order for this matrix element (Halderson, 1979).

Because it is the simpler part of term 1, we start the expansion with term 1B.

A-6 $$\langle 0|a_h^\dagger a_2(J_\gamma,T_\gamma)a_1(J,T)|$$

$$= \sum_{J_1,T_1} \bar{J}_\gamma\ \bar{T}_\gamma\ \bar{J}_1\ \bar{T}_1 \left\langle \begin{matrix} j_h & j_2 & J_\gamma \\ j_1 & J & J_1 \end{matrix} \right\rangle \left\langle \begin{matrix} 1/2 & 1/2 & T_\gamma \\ 1/2 & T & T_1 \end{matrix} \right\rangle$$

$$\cdot(-1)^{j_h+j_2+j_1+J+T+3/2} \langle 0|a_h^\dagger, a_2 a_1(J_1,T_1)(J,T)|$$

$$= \sum_{J_1,T_1} \bar{J}_\gamma\ \bar{T}_\gamma\ \bar{J}_1\ \bar{T}_1 \left\langle \begin{matrix} j_h & j_2 & J_\gamma \\ j_1 & J & J_1 \end{matrix} \right\rangle \left\langle \begin{matrix} 1/2 & 1/2 & T_\gamma \\ 1/2 & T & T_1 \end{matrix} \right\rangle$$

$$\cdot(-1)^{J_1+T_1+2j_h+j_1+j_2} \langle 0|a_2 a_1(J_1,T_1)a_h^\dagger(J,T)|$$

A-7 $$|(J,T)(J_h,T_h)a_h a_h(J_p,T_p)a_2^\dagger(J_a,T_a)a_1^\dagger a_1^\dagger|0\rangle$$

$$= \sum_{J_2,T_2} \bar{J}_2\ \bar{T}_2 \begin{Bmatrix} J_p & j_h & J_2 \\ j_h & J & J_h \end{Bmatrix} \begin{Bmatrix} T_p & 1/2 & T_2 \\ 1/2 & T & T_h \end{Bmatrix}$$

$$\cdot \bar{J}_h\ \bar{T}_h\ (-1)^{J_p+T_p+2j_h+J+T+1}$$

$$\cdot|(J,T)a_h(J_2,T_2)a_h(J_p,T_p)a_2^\dagger(J_a,T_a)a_1^\dagger a_1^\dagger|0\rangle$$

We can now combine the results of A-6 and A-7 to form the original matrix element A-3.

A-8 $\langle$ A-3 $\rangle$

$$= \sum_{J_1,T_1} \sum_{J_2,T_2} \bar{J}_\gamma\ \bar{T}_\gamma\ \bar{J}_1\ \bar{T}_1 \begin{Bmatrix} j_h & j_2 & J_\gamma \\ j_1 & J & J_1 \end{Bmatrix} \begin{Bmatrix} 1/2 & 1/2 & T_\gamma \\ 1/2 & T & T_1 \end{Bmatrix}$$

$$\cdot \begin{Bmatrix} J_p & j_h & J_2 \\ j_h & J & J_h \end{Bmatrix} \begin{Bmatrix} T_p & 1/2 & T_2 \\ 1/2 & T & T_h \end{Bmatrix} \bar{J}_h\ \bar{T}_h$$

$$\cdot \bar{J}_2\ \bar{T}_2\ (-1)^{J_p+T_p+J_1+T_1+j_1+j_2+J+T+1}$$

$$\prec 0|a_2 a_1(J_1,T_1)a_h^\dagger(J,T)|V|(J,T)a_h(J_2,T_2)a_h(J_p,T_p)a_2^\dagger(J_a,T_a)a_1^\dagger a_1^\dagger|0\rangle$$

$$= \sum_{J_1,T_1} \bar{J}_\gamma \bar{T}_\gamma \bar{J}_h \bar{T}_h \begin{Bmatrix} j_h & j_2 & J_\gamma \\ j_1 & J & J_1 \end{Bmatrix} \begin{Bmatrix} 1/2 & 1/2 & T_\gamma \\ 1/2 & T & T_1 \end{Bmatrix}$$

$$\cdot \begin{Bmatrix} J_p & j_h & J_1 \\ j_h & J & J_h \end{Bmatrix} \begin{Bmatrix} T_p & 1/2 & T_1 \\ 1/2 & T & T_h \end{Bmatrix} \delta^{J_1}_{J_2} \delta^{T_1}_{T_2} (\bar{J}_1 \bar{T}_1)^2$$

$$\cdot \frac{(1-(-1)^{-T_h-J_h})}{\sqrt{2}} (-1)^{J_p+T_p+J_1+T_1+j_1+j_2+J+T+1}$$

$$\prec 0| a_2 a_1(J_1,T_1) |V| (J_1,T_1) a_h(J_p,T_p) a^\dagger_2(J_a,T_a) a^\dagger_1 a^\dagger_1| 0 \succ$$

A-9

$$= \sum_{J_1,T_1} \bar{J}_\gamma \bar{T}_\gamma \bar{J}_h \bar{T}_h \begin{Bmatrix} j_h & j_2 & J_\gamma \\ j_1 & J & J_1 \end{Bmatrix} \begin{Bmatrix} 1/2 & 1/2 & T_\gamma \\ 1/2 & T & T_1 \end{Bmatrix}$$

$$\cdot \begin{Bmatrix} J_p & j_h & J_1 \\ j_h & J & J_h \end{Bmatrix} \begin{Bmatrix} T_p & 1/2 & T_1 \\ 1/2 & T & T_h \end{Bmatrix} \delta^{J_1}_{J_2} \delta^{T_1}_{T_2} (\bar{J}_1 \bar{T}_1)^2$$

$$\cdot \frac{(1-(-1)^{-T_h-J_h})}{\sqrt{2}} (-1)^{J_a+T_a+J_1+T_1+j_1+2j_2+J+T+3/2}$$

$$\prec 0| a_2 a_1(J_1,T_1) |V| (J_1,T_1) a_h(J_p,T_p) (J_a,T_a) a^\dagger_1 a^\dagger_1, a^\dagger_2| 0 \succ$$

$$= \sum_{J_1,T_1} \sum_{J_z,T_z} \bar{J}_p \bar{J}_z \bar{T}_p \bar{T}_z \begin{Bmatrix} j_2 & J_a & J_p \\ j_h & J_1 & J_z \end{Bmatrix} \begin{Bmatrix} 1/2 & T_a & T_p \\ 1/2 & T_1 & T_z \end{Bmatrix}$$

$$\cdot \bar{J}_\gamma \bar{T}_\gamma \bar{J}_h \bar{T}_h \begin{Bmatrix} j_h & j_2 & J_\gamma \\ j_1 & J & J_1 \end{Bmatrix} \begin{Bmatrix} 1/2 & 1/2 & T_\gamma \\ 1/2 & T & T_1 \end{Bmatrix}$$

$$\cdot \begin{Bmatrix} J_p & j_h & J_1 \\ j_h & J & J_h \end{Bmatrix} \begin{Bmatrix} T_p & 1/2 & T_1 \\ 1/2 & T & T_h \end{Bmatrix} \delta^{J_1}_{J_2} \delta^{T_1}_{T_2} (\bar{J}_1 \bar{T}_1)^2$$

$$\cdot\frac{(1-(-1)^{-T_h-J_h})}{\sqrt{2}}\quad(-1)^{j_1+j_2+j_h+J+T-1/2}$$

$$\prec 0|\,a_2 a_1(J_1,T_1)\,|V|\,(J_1,T_1)(J_z,T_z)a_h(J_a,T_a)a_1^\dagger a_1^\dagger, a_2^\dagger|\,0\succ$$

In the final step of term 1B we will drop the creation/annihilation operator notation, and return to the original notation.

A-10 $\quad\langle$ A-1 $\rangle$

$$=\sum_{J_1,T_1}\bar{J}_p\,\bar{j}_1\,\sqrt{2}\,\bar{T}_p\begin{Bmatrix} j_2 & J_a & J_p \\ j_h & J_1 & j_1\end{Bmatrix}\begin{Bmatrix} 1/2 & T_a & T_p \\ 1/2 & T_1 & 1/2\end{Bmatrix}$$

$$\cdot\bar{J}_\gamma\,\bar{T}_\gamma\,\bar{J}_h\,\bar{T}_h\begin{Bmatrix} j_h & j_2 & J_\gamma \\ j_1 & J & J_1\end{Bmatrix}\begin{Bmatrix} 1/2 & 1/2 & T_\gamma \\ 1/2 & T & T_1\end{Bmatrix}\delta_{j_1}^{J_z}\,\delta_{1/2}^{T_z}$$

$$\cdot\begin{Bmatrix} J_p & j_h & J_1 \\ j_h & J & J_h\end{Bmatrix}\begin{Bmatrix} T_p & 1/2 & T_1 \\ 1/2 & T & T_h\end{Bmatrix}\delta_{J_2}^{J_1}\,\delta_{T_2}^{T_1}\,(\bar{J}_1\,\bar{T}_1)^2$$

$$\cdot\frac{(1-(-1)^{-T_h-J_h})}{\sqrt{2}}\quad(-1)^{j_1+j_2+j_h+J+T-1/2}$$

$$\prec j_1|V|\,j_1^2(J_a,T_a)j_h^{-1}(j_1)\succ$$

We will leave term 1B as is for the time being. We now wish to deal with term 1A. The expansion is the same as for term 1B up to and including step A-8. The following continues from that point.

A-11 $$=\sum_{J_1,T_1}\bar{J}_\gamma\,\bar{T}_\gamma\,\bar{J}_h\,\bar{T}_h\begin{Bmatrix} j_h & j_2 & J_\gamma \\ j_1 & J & J_1\end{Bmatrix}\begin{Bmatrix} 1/2 & 1/2 & T_\gamma \\ 1/2 & T & T_1\end{Bmatrix}$$

$$\cdot \begin{Bmatrix} J_p & j_h & J_1 \\ j_h & J & J_h \end{Bmatrix} \begin{Bmatrix} T_p & 1/2 & T_1 \\ 1/2 & T & T_h \end{Bmatrix} \delta_{J_1 J_2} \delta_{T_1 T_2} (\bar{J}_1 \bar{T}_1)^2$$

$$\cdot \frac{(1-(-1)^{-T_h-J_h})}{\sqrt{2}} (-1)^{J_p+T_p+J+T+1}$$

$$\prec 0 | a_1 a_2 (J_1, T_1) |V| (J_1, T_1) a_h (J_p, T_p) a_2^\dagger (J_a, T_a) a_1^\dagger a_1^\dagger | 0 \rangle$$

$$= \sum_{J_1, T_1} \sum_{J_x, T_x} \bar{J}_a \bar{T}_a \bar{J}_x \bar{T}_x \begin{Bmatrix} j_1 & j_1 & J_a \\ j_2 & J_p & J_x \end{Bmatrix} \begin{Bmatrix} 1/2 & 1/2 & T_a \\ 1/2 & T_p & T_x \end{Bmatrix}$$

$$\cdot \bar{J}_\gamma \bar{T}_\gamma \bar{J}_h \bar{T}_h \begin{Bmatrix} j_h & j_2 & J_\gamma \\ j_1 & J & J_1 \end{Bmatrix} \begin{Bmatrix} 1/2 & 1/2 & T_\gamma \\ 1/2 & T & T_1 \end{Bmatrix}$$

$$\cdot \begin{Bmatrix} J_p & j_h & J_1 \\ j_h & J & J_h \end{Bmatrix} \begin{Bmatrix} T_p & 1/2 & T_1 \\ 1/2 & T & T_h \end{Bmatrix} \delta_{J_1 J_2} \delta_{T_1 T_2} (\bar{J}_1 \bar{T}_1)^2$$

$$\cdot \frac{(1-(-1)^{-T_h-J_h})}{\sqrt{2}} (-1)^{j_2+J+T+3/2}$$

$$\prec 0 | a_1 a_2 (J_1, T_1) |V| (J_1, T_1) a_h (J_p, T_p) (J_x, T_x) a_2^\dagger a_1^\dagger, a_1^\dagger | 0 \rangle$$

$$= \sum_{J_1, T_1} \sum_{J_x, T_x} \sum_{J_y, T_y} \bar{J}_p \bar{J}_y \bar{T}_p \bar{T}_y \begin{Bmatrix} j_1 & J_x & J_p \\ j_h & J_1 & J_y \end{Bmatrix} \begin{Bmatrix} 1/2 & T_x & T_p \\ 1/2 & T_1 & T_y \end{Bmatrix}$$

$$\cdot \bar{J}_a \bar{T}_a \bar{J}_x \bar{T}_x \begin{Bmatrix} j_1 & j_1 & J_a \\ j_2 & J_p & J_x \end{Bmatrix} \begin{Bmatrix} 1/2 & 1/2 & T_a \\ 1/2 & T_p & T_x \end{Bmatrix}$$

$$\cdot \bar{J}_\gamma \bar{T}_\gamma \bar{J}_h \bar{T}_h \begin{Bmatrix} j_h & j_2 & J_\gamma \\ j_1 & J & J_1 \end{Bmatrix} \begin{Bmatrix} 1/2 & 1/2 & T_\gamma \\ 1/2 & T & T_1 \end{Bmatrix}$$

$$\cdot \begin{Bmatrix} J_p & j_h & J_1 \\ j_h & J & J_h \end{Bmatrix} \begin{Bmatrix} T_p & 1/2 & T_1 \\ 1/2 & T & T_h \end{Bmatrix} \delta_{J_1 J_2} \delta_{T_1 T_2} (\bar{J}_1 \bar{T}_1)^2$$

$$\cdot \frac{(1-(-1)^{-T_h-J_h})}{\sqrt{2}} (-1)^{j_2+j_1+j_h+J_x+T_x+J_1+T_1+J+T+1/2}$$

$$\prec 0 | a_1 a_2 (J_1,T_1) |V| (J_1,T_1)(J_y,T_y) a_h (J_x,T_x) a_2^\dagger a_1^\dagger, a_1^\dagger | 0 \rangle$$

In the final step of term 1A we will drop the creation/annihilation operator notation, and return to the original notation.

A-12 $\langle$ A-1 $\rangle$

$$= \sum_{J_1,T_1} \sum_{J_x,T_x} \bar{J}_p \bar{j}_2 \bar{T}_p \sqrt{2} \begin{Bmatrix} j_1 & J_x & J_p \\ j_h & J_1 & j_2 \end{Bmatrix} \begin{Bmatrix} 1/2 & T_x & T_p \\ 1/2 & T_1 & 1/2 \end{Bmatrix}$$

$$\cdot \bar{J}_a \bar{T}_a \bar{J}_x \bar{T}_x \begin{Bmatrix} j_1 & j_1 & J_a \\ j_2 & J_p & J_x \end{Bmatrix} \begin{Bmatrix} 1/2 & 1/2 & T_a \\ 1/2 & T_p & T_x \end{Bmatrix}$$

$$\cdot \bar{J}_\gamma \bar{T}_\gamma \bar{J}_h \bar{T}_h \begin{Bmatrix} j_h & j_2 & J_\gamma \\ j_1 & J & J_1 \end{Bmatrix} \begin{Bmatrix} 1/2 & 1/2 & T_\gamma \\ 1/2 & T & T_1 \end{Bmatrix}$$

$$\cdot \begin{Bmatrix} J_p & j_h & J_1 \\ j_h & J & J_h \end{Bmatrix} \begin{Bmatrix} T_p & 1/2 & T_1 \\ 1/2 & T & T_h \end{Bmatrix} \delta_{J_1 J_2} \delta_{T_1 T_2} (\bar{J}_1 \bar{T}_1)^2$$

$$\cdot \frac{(1-(-1)^{-T_h-J_h})}{\sqrt{2}} (-1)^{j_2+j_1+j_h+J_x+T_x+J_1+T_1+J+T+1/2}$$

$$\cdot \frac{(1-(-1)^{-T_a-J_a})}{\sqrt{2}} \delta_{j_2 J_y} \delta_{1/2 T_y}$$

$$\prec j_2 |V| j_1 j_2 (J_x, T_x) j_h^{-1}(j_2) \succ$$

We will leave term 1A as is for the time being. We now wish to deal with term 2. The expansion starts with the ket in its original form and the bra in the form resulting from step A-6. The following continues from that point.

A-13

$$= \sum_{J_1,T_1} \sum_{J_c,T_c} \bar{J}_a \bar{J}_c \bar{T}_a \bar{T}_c \begin{Bmatrix} j_2 & j_1 & J_c \\ j_1 & J_p & J_a \end{Bmatrix} \begin{Bmatrix} 1/2 & 1/2 & T_c \\ 1/2 & T_p & T_a \end{Bmatrix}$$

$$\cdot \begin{Bmatrix} j_h & j_2 & J_\gamma \\ j_1 & J & J_1 \end{Bmatrix} \begin{Bmatrix} 1/2 & 1/2 & T_\gamma \\ 1/2 & T & T_1 \end{Bmatrix} \bar{J}_\gamma \bar{T}_\gamma \bar{J}_1 \bar{T}_1$$

$$\cdot (-1)^{J_1+T_1+j_1+j_2+J_a+T_a+1}$$

$$\prec 0| a_2 a_1(J_1,T_1) a_h^\dagger(J,T) |V| (J,T)(J_h,T_h) a_h a_h(J_p,T_p) a_1^\dagger(J_c,T_c) a_1^\dagger a_2^\dagger |0\succ$$

$$= \sum_{J_1,T_1} \sum_{J_c,T_c} \sum_{J_k,T_k} \bar{J}_p \bar{T}_p \bar{J}_k \bar{T}_k \begin{Bmatrix} J_c & j_1 & J_p \\ J_h & J & J_k \end{Bmatrix} \begin{Bmatrix} T_c & 1/2 & T_p \\ T_h & T & T_k \end{Bmatrix}$$

$$\cdot \bar{J}_a \bar{J}_c \bar{T}_a \bar{T}_c \begin{Bmatrix} j_2 & j_1 & J_c \\ j_1 & J_p & J_a \end{Bmatrix} \begin{Bmatrix} 1/2 & 1/2 & T_c \\ 1/2 & T_p & T_p \end{Bmatrix}$$

$$\cdot \begin{Bmatrix} j_h & j_2 & J_\gamma \\ j_1 & J & J_1 \end{Bmatrix} \begin{Bmatrix} 1/2 & 1/2 & T_\gamma \\ 1/2 & T & T_1 \end{Bmatrix} \bar{J}_\gamma \bar{T}_\gamma \bar{J}_1 \bar{T}_1$$

$$\cdot (-1)^{J_1+T_1+J_c+T_c+J_h+T_h+j_2+J_a+T_a+J+T+1/2}$$

$$\cdot \langle 0 | a_2 a_1 (J_1, T_1) a_h^\dagger (J, T) | V | (J, T)(J_k, T_k)(J_h, T_h) a_h a_h, a_1^\dagger (J_c, T_c) a_1^\dagger a_2^\dagger | 0 \rangle$$

In the final step of term 2 we will drop the creation/annihilation operator notation, and return to the original notation.

A-14 $\langle$ A-1 $\rangle$

$$= \sum_{J_1, T_1} \bar{J}_p \bar{T}_p \bar{j}_h \sqrt{2} \begin{Bmatrix} J_1 & j_1 & J_p \\ J_h & J & j_h \end{Bmatrix} \begin{Bmatrix} T_1 & 1/2 & T_p \\ T_h & T & 1/2 \end{Bmatrix}$$

$$\cdot \bar{J}_a \bar{T}_a \begin{Bmatrix} j_2 & j_1 & J_1 \\ j_1 & J_p & J_a \end{Bmatrix} \begin{Bmatrix} 1/2 & 1/2 & T_1 \\ 1/2 & T_p & T_p \end{Bmatrix}$$

$$\cdot \begin{Bmatrix} j_h & j_2 & J_\gamma \\ j_1 & J & J_1 \end{Bmatrix} \begin{Bmatrix} 1/2 & 1/2 & T_\gamma \\ 1/2 & T & T_1 \end{Bmatrix} \bar{J}_\gamma \bar{T}_\gamma (\bar{J}_1 \bar{T}_1)^2$$

$$\cdot (-1)^{J_h + T_h + j_2 + J_a + T_a + J + T + 1/2}$$

$$\cdot \frac{(1-(-1)^{-T_a - J_a})}{\sqrt{2}} \delta^{J_k}_{j_h} \delta^{T_k}_{1/2} \delta^{J_c}_{J_1} \delta^{T_c}_{T_1}$$

$$\cdot \langle j_h^{-1} | V | j_1 (j_h^{-2}) (J_h, T_h) (j_h^{-1}) \rangle$$

We will leave term 2 as is for the time being.

We now have expanded terms 1A, 1B, and 2 in terms of simple particle–hole matrix elements. These matrix elements can be expressed in terms of two-body matrix elements between particle states with the following relations (Halderson, 1979).

A-15

$$\langle j_1 | V | j_1^2(J_a, T_a) j_h^{-1}(j_1) \rangle$$

$$= - \frac{\bar{J}_a \, \bar{T}_a}{\sqrt{2} \, \bar{j}_1} \langle j_h j_1 (J_a, T_a) | V | (j_1^2)(J_a, T_a) \rangle$$

A-16

$$\langle j_2 | V | j_1 j_2 (J_x, T_x) j_h^{-1}(j_2) \rangle$$

$$= - \frac{\bar{J}_x \, \bar{T}_x}{\sqrt{2} \, \bar{j}_2} \langle j_h j_2 (J_x, T_x) | V | j_1 j_2 (J_x, T_x) \rangle$$

A-17

$$\langle j_h^{-1} | V | j_1 (j_h^{-2})(J_h, T_h)(j_h^{-1}) \rangle$$

$$= (-1)^{J_h + T_h + j_1 - j_h + 1} \frac{\bar{J}_h \, \bar{T}_h}{\sqrt{2} \, \bar{j}_h}$$

$$\cdot \langle j_h^2 (J_h, T_h) | V | j_1 j_h (J_h, T_h) \rangle$$

If we now insert relations A-15, A-16, and A-17 into equations A-10, A-12, and A-14 respectively, we then have terms 1A, 1B, and 2 in their final forms. These three terms together constitute the final form of the matrix element. This final form is shown in Table 2-1.

BIOGRAPHY

Robert Andrew August, Jr.

PERSONAL: Born in Camden, NJ, July 1, 1957

EDUCATION: B.A. Rutgers University-Camden College of Arts and Science, 1979

M.A. Duke University, 1981

POSITIONS: Research Assistant, Triangle Universities Nuclear Laboratory, 1980-1984

Graduate Teaching Assistant, Duke University, 1979-1980

SOCIETY MEMBERSHIPS:

American Physical Society
Physics Honor Society-Sigma Pi Sigma

PUBLICATIONS AND ABSTRACTS:

"Polarized Neutron Capture into ^{13}C: Evidence for a Secondary Doorway State Effect" with J.G. Woodworth, N.R. Roberson, D.R. Tilley, H.R. Weller and J.W. Jury, Phys. Rev. C 29, 1186 (1984).

"Evidence for a Secondary Doorway State in A=13 Nuclei from Unpolarized and Polarized Capture Measurements" with J.G. Woodworth, N.R. Roberson, D.R. Tilley, H.R. Weller and J.W. Jury, Proceedings of Light Ion Conference, Osaka, Japan, May (1983).

"The $^{11}B(d,\gamma)^{13}C$ reaction" with N.R. Roberson, H.R. Weller, J. Lafferty, D.R. Tilley and S. Cotanch, Bull. Am. Phys. Soc. 27, 708 (1982).

"Radiative Nucleon Capture by ^{12}C" with J.G. Woodworth, N.R. Roberson, D.R. Tilley, H.R. Weller, H. Yao and J.W. Jury, Bull. Am. Phys. Soc. 27, 709 (1982).